ALMA MATER STUDIORUM
UNIVERSITÀ DI BOLOGNA

DOTTORATO DI RICERCA IN

INGEGNERIA ELETTRONICA, TELECOMUNICAZIONI E TECNOLOGIE DELL'INFORMAZIONE

Ciclo 37

Settore Concorsuale: 09/F1 - CAMPI ELETTROMAGNETICI

Settore Scientifico Disciplinare: ING-INF/02 - CAMPI ELETTROMAGNETICI

INTEGRATED ANTENNA TECHNOLOGIES AND WIRELESS POWER TRANSFER SOLUTIONS FOR SPACE AND COMMUNICATIONS SYSTEMS

Presentata da: Ahmet Baris Gok

Coordinatore Dottorato

Davide Dardari

Supervisore

Alessandra Costanzo

Co-supervisore

Diego Masotti

Esame finale anno 2025

In memory of my dear friend, Mete Can Kaya, and all the lives tragically lost in the February 6, 2023, Kahramanmaraş Earthquakes.

Acknowledgments

Completing this PhD has been a transformative journey, filled with intense dedication, countless learning opportunities, and moments that challenged me both intellectually and personally. This work represents not only years of research and persistence but also the culmination of countless experiences, learning curves, and the invaluable support of those around me. The life of a PhD is a unique one—a mix of trials, triumphs, and resilience that shapes both the mind and character. I am grateful for the obstacles that have pushed me to grow, for the discoveries that have inspired me, and for the relationships that have sustained me.

First and foremost, I would like to extend my sincere gratitude to my supervisors, Prof. Alessandra Costanzo and Prof. Diego Masotti. Their unwavering guidance, encouragement, and insight have been foundational to this work. Their expertise and commitment to my progress helped shape both this research and my personal growth as a researcher. I am deeply thankful for their mentorship and belief in me throughout this process.

I am also profoundly grateful to my colleagues in the lab, whose collaboration and camaraderie have made the journey all the more rewarding. A special thank you to Francesca, who has not only been a great collaborator but also a dear friend. Her kindness and constant support have been invaluable, especially as I navigated life as an expat in a new country. Her friendship has been a source of comfort, and her support, both in and out of the lab, has made a lasting difference in my life.

I would like to express my deepest gratitude to my family, whose love and support have been my foundation throughout this journey. My parents, Halil and Aslı, and my sister, Derya, have always motivated me to push forward, providing encouragement and belief in my abilities. I am especially thankful to my grandfather, Sabri, whose guidance and wisdom have been instrumental in my path. His life experiences and insights have offered me invaluable lessons, instilling in me the importance of perseverance and hard work.

And finally, my deepest thanks to my partner, Ezgi, who has been my anchor through every high and low. Her patience, understanding, and constant support have meant the world to me, and I am grateful every day for her presence in my life.

To all those who have been part of this journey, thank you for your support, belief, and kindness. This work is as much yours as it is mine.

Abstract

This thesis centers on advancing integrated antenna technologies and wireless power transfer (WPT) systems, with a primary emphasis on space applications and additional relevance to communication. The research presents an inventive approach that integrates transparent antennas with photovoltaic (PV) panels, enabling satellites to simultaneously capture solar energy and transmit power wirelessly. This dual-function design optimizes surface utility—an essential factor for small satellites where space and weight constraints are paramount.

Transparent antennas are designed using conductive mesh patterns that ensure a high level of optical transparency while maintaining strong electromagnetic performance. These antennas can be seamlessly integrated onto solar panels without significantly impacting their power generation capabilities, offering a practical solution for energy-hungry space missions. By optimizing antenna geometry and adjusting key parameters, such as eliminating horizontal lines to improve transparency, the study achieves a balance between transparency and antenna efficiency. The research also includes a broad investigation into the role of the solar panel's top metal contacts, which are crucial to the performance of both the solar panel and the antenna. This investigation reveals how the top contacts influence antenna radiation patterns and solar cell efficiency, leading to critical insights for optimizing the integration of the two technologies.

A central focus of this thesis is the exploration of WPT for CubeSats. By assessing power transfer networks between larger satellites and CubeSat swarms, the research demonstrates how coordinated power sharing can extend mission longevity. A key contribution is the design of a highly efficient Class-E amplifier-based inverter, which converts solar-generated power into high-frequency signals for wireless transmission. This efficient system is essential for space applications, where energy resources are limited. The design is carefully optimized to integrate seamlessly with the transparent antenna array, enabling effective wireless energy transfer with minimal losses.

The findings have significant implications beyond space, particularly in terrestrial communication systems, where WPT can support the growing demand for energy-efficient solutions in the Internet of Things (IoT) and other low-power devices. The research not only offers a practical solution for satellite power management but also provides a foundation for future innovations in wireless energy systems across multiple industries. By addressing key challenges in antenna transparency, solar panel integration, and efficient power conversion, this thesis contributes to the advancement of next-generation energy systems for both space-based and terrestrial applications.

Table of Contents

List of Figures

List of Tables

List of Abbreviations

AC	Alternating Current
BTM	Balise Transmission Module
BTM-RX	Balise Receive Module
BTM-TX	Balise Transfer Module
DC	Direct Current
EM	Electromagnetic
ESA	European Space Agency
FSK	Frequency-Shift Keying
FSS	Frequency Selective Surfaces
GaN	Gallium Nitride
HEMT	High-Electron-Mobility transistor
IIoT	Industrial Internet of Things
IoT	Internet of Things
IR	Infrared
ITO	Indium Tin Oxide
LEO	Low Earth Orbit
LoRa	Long Range
LPWAN	Low-Power Wide-Area Network
MAM	Microwave Absorption Material
MIMO	Multiple-Input and Multiple-Output
PCB	Printed Circuit Board
PMU	Power Management Unit
PV	Photovoltaic
RF	Radio Frequency
SLL	Sidelobe Level
TCF	Transparent Conductive Film
TXL	Transmission Line
UV	Ultraviolet
UWB	Ultra-Wideband
WLAN	Wireless Local Area Network
WPT	Wireless Power Transfer
WSN	Wireless Sensor Network

List of Symbols

ϵ_r	Relative permittivity
T_{sub}	Transparency of a substrate
S_{ij}	Scattering parameter
P_T	Transmitted power
G_T	Transmitting antenna gain
G_R	Receiving antenna gain
P_R	Received power
d	Distance between satellites (Chapter 3)
λ	Wavelength
π	Pi constant
N_e	Number of elements
L_i	Inductor (Chapter 5)
C_i	Capacitor (Chapter 5)
R_i	Resistor (Chapter 5)
SP	Spectral purity
$tan\delta$	Loss tangent
D_i	Diode (Chapter 6)
P_{DC}	DC power
$\eta_{RF-to-DC}$	RF-to-DC efficiency
M	Expansion margin (Chapter 7)

1 Introduction

The rapid evolution of modern communication and space systems has driven an increasing demand for efficient, compact, and multi functional components capable of supporting advanced applications. Among these components, antenna systems play a critical role in enabling wireless communication and power transfer, two essential aspects for the operation of satellites, spacecraft, and terrestrial communication systems. Traditionally, antennas have been primarily used for transmitting and receiving data, but recent technological advancements have expanded their functionality to include wireless power transfer (WPT) [1]. The concept of WPT was first introduced by Tesla [2], and has evolved significantly over the past decade [3], particularly in resonance coupling, enabling the commercialization of wireless charging systems and sparking interest for applications such as energy harvesting and narrow-beam, high-efficiency power transfer. WPT can be broadly divided into two categories: near-field and far-field power transfer. Near-field WPT is used for short-range power transfer, typically through magnetic fields via inductive coupling or electric fields between the transmitter and energy harvester. Far-field WPT, on the other hand, involves the use of ambient radio frequency (RF) waves in the surrounding environment, either indoors or outdoors, and can utilize backscattering techniques to provide a more sustainable power source for longer distances. In far-field WPT, the focus is on maximizing the efficiency of power transfer from the transmitter to the harvester, which directly impacts the amount of direct current (DC) power that can be extracted. A critical component in this process is the rectenna, a device that combines a rectifier and an antenna to convert received RF signals into usable energy. The convergence of these two capabilities—communication and power transfer—within a single platform represents a transformative development in the fields of space-based systems, the Internet of Things (IoT) [4], and energy-harvesting technologies.

At the forefront of this evolution is the concept of integrated antenna technologies, where the dual functionalities of signal transmission and energy harvesting are combined. These systems hold significant potential for improving the performance of small satellite constellations, such as CubeSats, which are rapidly becoming the preferred platforms for space exploration, scientific missions, and commercial applications. However, realizing such multifunctional systems requires overcoming several technical challenges, including optimizing antenna design for high efficiency, ensuring seamless integration with other system components, and achieving compactness without compromising performance.

CubeSats, characterized by their small size and modular design, have transformed the landscape of satellite technology. Originally developed as educational tools, these compact satellites have quickly evolved into powerful platforms capable of supporting a wide range of missions, from Earth observation and remote sensing to deep space

exploration [5]. Their standardized dimensions and low launch costs make them particularly appealing for universities, research institutions, and commercial entities seeking to test innovative technologies in space. As the demand for satellite-based services continues to grow, CubeSats offer a flexible and scalable solution, enabling rapid deployment and the ability to form constellations for enhanced data collection and communication.

A CubeSat can use a single antenna for multiple functions or employ several antennas to maintain modularity, but this introduces challenges such as potential interference and crosstalk, demanding innovative designs that maximize functionality while minimizing space and weight. Successful CubeSat antenna design requires a deep understanding of link budgets—covering the transmitter, wireless path, and receiver—along with the interplay between transmitted power, signal losses, and noise, which are crucial for optimizing communication performance [6]. Antenna systems are key for CubeSat communication and remote sensing, but the inherent trade-off between antenna gain and size presents significant RF and mechanical challenges, driving the scientific community to develop advanced designs that balance performance, data rate, and resolution with size constraints for modern missions [7]. Common types of antennas used in CubeSat systems include wire antennas [8], reflector antennas [9], reflectarray antennas [10], horn antennas [11], and patch antennas [12]. Given the critical importance of space and weight constraints in small satellites, the deployability of antennas has become a key focus, playing an increasingly crucial role in their design.

Furthermore, in WPT systems, particularly for space applications, the distance between the transmitter and receiver is a critical factor that directly influences the efficiency and feasibility of power transfer. As distance increases, signal attenuation and path losses become more pronounced, making it challenging to maintain effective

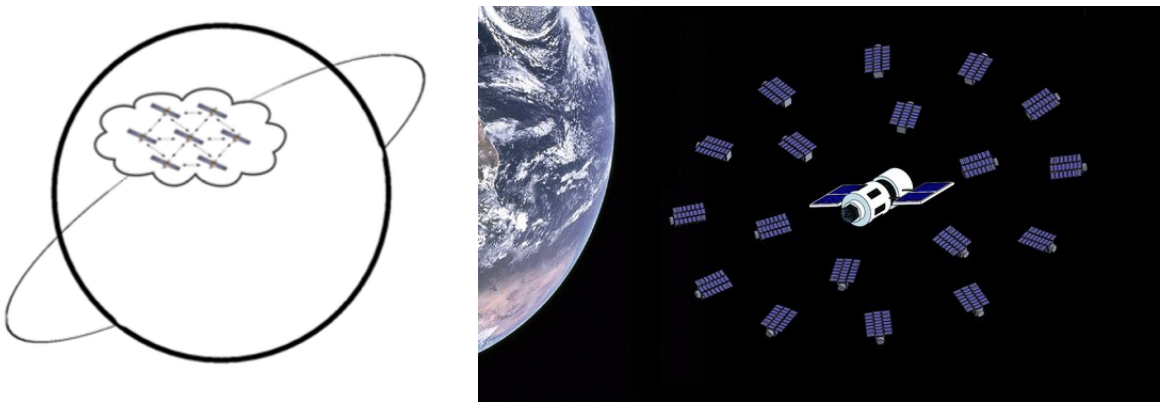

(a) **(b)**

Fig. 1.1. CubeSat swarm constellation of (a) schematic representation [13] and (b) visual representation in space [14].

power delivery. This is especially important in space, where vast distances require highly efficient, focused energy transmission to minimize losses. The deployment of CubeSats in swarm constellations enhances the feasibility of WPT by enabling closer proximity between satellites, thereby reducing the distance required for power transfer and improving overall efficiency. Some example depictions of such swarm constellations are shown in Fig. 1.1. These constellations can facilitate a network of interconnected satellites, enabling more practical and scalable wireless power distribution across short distances in space, a key consideration for future inter-satellite energy-sharing systems.

Antenna gain is a critical factor in addressing the challenges posed by long-distance WPT in space applications. Higher gain can help compensate for signal attenuation and path losses by concentrating the transmitted energy in a specific direction, thereby increasing the efficiency of power transfer over extended distances. This can be effectively achieved through the use of antenna arrays, which leverage multiple radiating elements to form a highly directional beam. By deploying antenna arrays on CubeSats within swarm constellations, the system can further enhance power transmission capabilities, ensuring more precise and efficient energy transfer between satellites over greater distances, making inter-satellite energy sharing more feasible in large-scale space operations. However, the issue of limited surface area persists, particularly for small satellites like CubeSats. The available space for antenna deployment is quite restricted, which poses a significant challenge for enhancing antenna performance. Deployable surfaces offer a potential solution to this limitation, allowing for larger antenna arrays to be deployed in orbit. Yet, this approach introduces new complications, as most of a CubeSat's surface must be dedicated to solar panels, which are critical for generating the power necessary for satellite operation and maintaining essential systems. Solar cells, especially in space environments, are vital for nanosatellites to function effectively, providing the only reliable energy source over extended missions. Therefore, the integration of antenna systems with solar panels becomes even more critical. Achieving this integration while maintaining sufficient solar power production is a crucial design objective. The development of transparent or conformal antennas that can be seamlessly integrated with solar panels offers a promising pathway to overcoming these constraints, ensuring that both power generation and communication needs are met without compromising satellite functionality.

Another added benefit of integrating WPT with solar panels is the potential for WPT to serve as an additional power source for satellites, supplementing the energy provided by solar cells. This is particularly advantageous when satellites enter eclipse phases, where direct sunlight is blocked due to orbital positioning. During these periods, solar power generation ceases, which not only limits the energy available for satellite operations but also reduces temperatures, potentially degrading the

performance of onboard batteries. The inclusion of WPT can be a critical solution in these scenarios, as it ensures a continuous power supply regardless of sunlight availability. A notable example of the consequences of limited energy supply in space missions is the Rosetta mission [15], where the Philae lander, deployed on Comet 67P/Churyumov–Gerasimenko, landed in a shadowed region and was unable to recharge its batteries due to a lack of sunlight. As a result, Philae could only operate for a few days before its mission was cut short, highlighting the vulnerability of relying solely on solar energy in space. WPT could have extended Philae's operational lifespan by providing a secondary power source, demonstrating the importance of exploring alternative energy solutions in future space missions. Implementing WPT as a supplement to solar power could significantly enhance the sustainability and reliability of space probes and satellites, especially in environments with limited solar exposure.

Building on these advancements, this dissertation explores cutting-edge antenna technologies integrated with WPT solutions, emphasizing space applications with potential extensions to ground-based communication systems, as the system architecture is illustrated in Fig. 1.2. This dual-purpose approach optimizes energy utilization and addresses the power constraints of small spacecraft, particularly in remote orbits where frequent battery recharging is unfeasible. The increasing demand for sustainable power solutions in space drives this research, as traditional power generation methods face limitations due to size, weight, and environmental constraints. Integrated antenna systems that wirelessly transfer energy between satellites offer a continuous energy supply to meet both communication and operational demands. Additionally, transparent antenna arrays, seamlessly integrated with solar panels, maximize surface area for energy harvesting, enhancing power generation efficiency

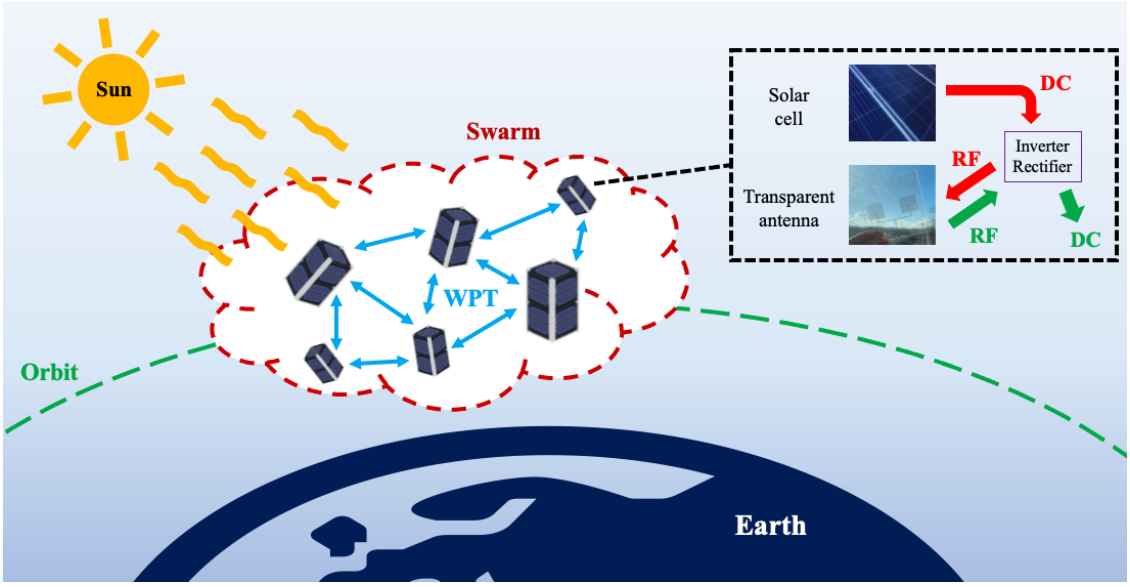

Fig. 1.2. System architecture for WPT between small satellites in near proximity [16].

without altering the satellite's physical profile or significantly increasing its mass.

Beyond its applications in space systems, the principles established in this research have significant implications for terrestrial communication networks. WPT can play a pivotal role in sustaining low-power IoT devices and other autonomous systems, where conventional power sources may be scarce or impractical. The integration of energy transfer capabilities with communication technologies offers the potential to enhance the efficiency of telecommunication infrastructure, ensuring uninterrupted service even in remote or off-grid locations with limited power access. This synergy between WPT and communication systems represents a promising avenue for the future of sustainable network operations.

This thesis investigates multiple facets of antenna design, electromagnetic simulation, and system optimization to develop efficient, robust integrated antenna systems. A primary focus is placed on Class-E amplifiers, known for their high efficiency in power conversion, making them well-suited for low-voltage, high-frequency operations, which are characteristic of space and communication systems. The study examines the use of Class-E amplifier-based inverters to facilitate WPT via resonant circuits, along with methods for biasing these circuits directly from photovoltaic (PV) cells. This approach capitalizes on the abundant solar energy in space, ensuring that the power supply remains both sustainable and reliable.

The objectives of this research are threefold: first, to design and optimize antenna systems capable of supporting both communication and wireless power transfer; second, to explore the integration of transparent antenna arrays with PV panels for space-based applications; and third, to investigate the implementation of high-efficiency power amplifiers, such as Class-E amplifiers, to enable reliable wireless power transfer. The outcomes of this work are expected to contribute significantly to the advancement of next-generation satellite technologies and sustainable communication networks, addressing the pressing challenges of energy efficiency and power management in modern electronic systems.

It is important to note that the chapters in this thesis are not organized in a strict chronological order based on the progression of the research. Instead, they are structured by the relative significance of the activities undertaken, with the transparent antenna concept taking precedence. Therefore, the initial chapters focus primarily on this area, followed by discussions of other wireless power transfer applications in later sections.

The structure of this dissertation is organized as follows: Chapter 2 presents a foundational investigation into the design and integration of meshed antennas with solar panels, marking a significant advancement in this research. Chapter 3 conducts a feasibility study of a solar-powered rectenna/transmitter system for in-space applications, aiming to establish realistic link budgets for various satellite constellation scenarios and provide estimations of WPT link distances through detailed simulations

and power calculations. Furthermore, Chapter 4 serves as a critical foundation of the thesis, delivering an in-depth analysis of the antenna array's performance while offering significant insights into the role of the top contacts on photovoltaic panels. Chapter 5 focuses on the design of an efficient inverter, which acts as a crucial link between antenna radiation and solar power production, thereby concluding the primary focus of the thesis. The subsequent chapters explore terrestrial applications of WPT, which, while distinct, are essential for the success and overall enhancement of the space-related research. Chapter 6 details the development of an innovative modular system that enables simultaneous energy and information transmission between unplugged trolleys in industrial environments, leveraging WPT and battery-less communication nodes for communication to ensure efficient operation and reliability across varying trolley arrangements. In Chapter 7, a novel bidirectional monopole antenna array optimized for Wireless Local Area Network (WLAN) applications is presented, featuring a minimized ground plane configuration that significantly reduces side lobe levels and enhances gain and bandwidth, while also addressing the critical balance necessary in ground plane size to optimize performance without compromising practicality. Moreover, Chapter 8 introduces an innovative design for powering train balises, validated through simulations and measurements, while addressing key challenges such as impedance matching and optimizing circuit efficiency, ultimately achieving a significant reduction in power requirements for balise activation. Finally, Chapter 9 examines the potential advancements and consequences associated with in-space WPT and Chapter 10 concludes with a discussion of the findings.

2 Transparent Antenna Technologies for Solar Energy and Microwave WPT Integration

This chapter is based on the following article:

[17] A. B. Gok, D. Masotti, and A. Costanzo, "Integration of solar power and microwave wpt exploiting transparent antennas," in *2023 IEEE Wireless Power Technology Conference and Expo (WPTCE)*, 2023, pp. 1–4.

2.1 Introduction to the Chapter

Transparent antennas are a state-of-the-art innovation in the growth of wireless communication and infrastructure systems. As urban areas transform into more interconnected networks, often called smart cities [18], the integration of communication technologies into the urban fabric becomes essential. Traditional antennas, which are often large and visually disruptive, fail to meet the aesthetic and practical needs of today's cities. Transparent antennas provide a compelling alternative, offering robust wireless communication while blending into infrastructure, preserving the appearance of buildings [19], windows [20], and vehicles [21] without drawing attention.

The push for optically transparent antennas is largely driven by the demands of next-generation wireless networks like 5G [22] and beyond, which require higher frequencies, faster response times, and more bandwidth to accommodate the rising number of mobile devices and the IoT. Another exciting application of transparent antennas is their integration into glass surfaces for Frequency Selective Surfaces (FSS), which combine the dual functions of microwave filtering and optical transparency [23]. FSS technology is useful in security-critical environments such as hospitals and government buildings, where control over signal propagation is essential. The use of transparent antennas goes beyond urban environments and is being applied in aerospace technologies as well. A notable example is the CubeSat platform, a compact satellite used for space research, which has benefited from the incorporation of transparent antennas. By integrating antennas onto the solar panels of these satellites, engineers can optimize surface area for power generation without compromising communication performance with Earth-based stations. This dual-purpose design is especially advantageous for space missions, where the efficient use of every square centimeter of the satellite's surface is essential.

In addition to their established role in satellite communication, transparent antennas are emerging as a pivotal component in the development of advanced WPT systems. Recent innovations are investigating the integration of transparent antennas

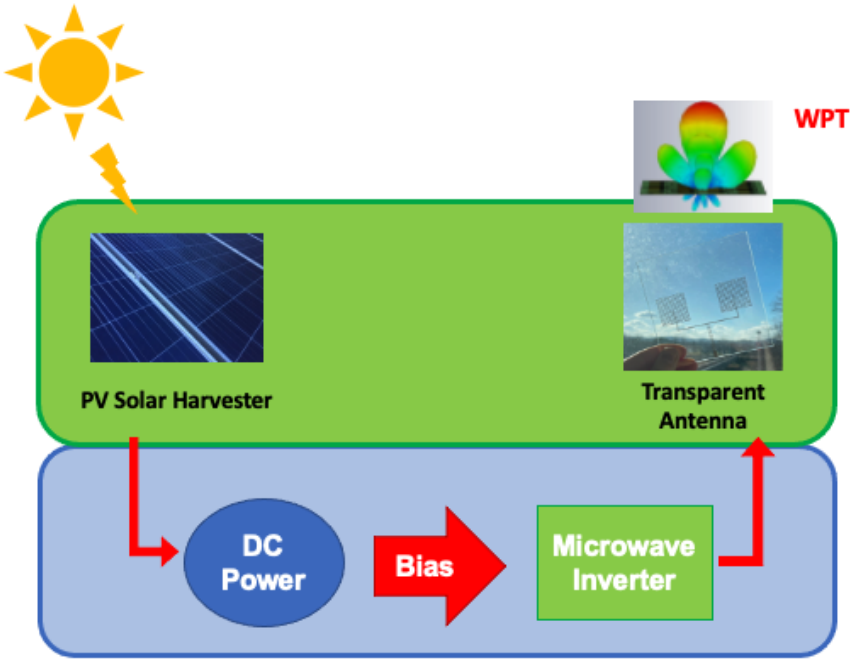

Fig. 2.1. Overview of solar panel integration with transparent antennas for WPT.

with PV cells to facilitate energy transfer between space-based platforms, such as CubeSats. This cutting-edge approach, illustrated in Fig. 2.1, merges solar energy harvesting with wireless power transmission into a single, optically transparent system. The significance of this integration lies not only in reducing the payload for aerospace vehicles but also in offering an alternative energy source to satellites operating in the harsh and unpredictable environment of space. One of the key challenges in this domain is ensuring that the integration of solar cells does not adversely impact the performance of the transparent antennas, and vice versa. Specifically, the transparent antenna must maintain its electromagnetic functionality without obstructing the efficiency of the solar cells. Achieving this delicate balance between transparency and functionality requires a nuanced understanding of both antenna design and PV integration. As a result, optimizing the compatibility of these components is a critical research area.

Before delving into the specifics of the thesis work, it is important to highlight various types of transparent antennas and notable advancements in the field. These advancements provide essential context for understanding the challenges and innovations presented in this thesis, particularly with regard to developing systems that maximize both solar energy collection and wireless power transmission efficiency.

2.2 Varieties of Transparent Conductors

In the design of transparent antennas, two main approaches are employed: transparent conductive films (TCFs) and conductive meshes. TCFs typically refer to materials like indium tin oxide (ITO), which is a type of transparent conducting oxide (TCO). However, the literature also highlights various other materials and nanostructures. Conversely, conductive meshes are made up of a network of conductive wires that achieve transparency by strategically removing conductive material from the design. While this category primarily includes mesh structures, it is not confined to them; there are numerous examples of conductive metallization in various shapes that can still provide acceptable levels of optical transparency.

2.2.1 Transparent Conductive Films

Thin-film-based antennas offer several advantages, particularly when integrated with glass substrates, due to their high conductivity, ease of availability, and transparency. However, the high cost of materials used in these designs remains a significant challenge. Researchers have explored various materials and techniques to improve antenna performance while maintaining transparency. ITO is a commonly used material for transparent antennas, but alternatives like gallium-doped zinc oxide are being explored due to cost and material availability concerns. These materials, often applied in thin-film form, have been shown to deliver good performance in various frequency ranges, from GHz to millimeter waves, and are suitable for modern applications such as 5G communication and intelligent transport systems.

Different antenna designs, including reflect arrays, dipoles, and coplanar waveguides, have been studied, with promising results in terms of efficiency, gain, and bandwidth. For instance, some designs achieve high transparency with minimal loss, making them ideal for applications where aesthetics or integration with existing infrastructure is important, such as mounting antennas on building glass for communication purposes. In urban cellular networks, transparent antennas using conductive films or specialized coatings have demonstrated notable gains and bandwidth, showing potential for multilayer designs in high-frequency applications.

Authors in [24] designed and tested transparent antennas using patterned ITO on flexible Corning® Willow® Glass for wireless applications in the 2.4 GHz and 5.8 GHz ISM bands. These antennas, including grid, loop, and split-ring monopoles, achieved 90% transparency and efficient radiation. The fabricated antennas, illustrated in Fig. 2.2a, demonstrated good agreement, making them suitable for applications such as glass-mounted systems in homes, cars, and commercial buildings. In another study [25], the authors presented a transparent ITO patch antenna (Ant1) designed for operation at 4.9 GHz, as shown in Fig. 2.2b. The antenna features a square radiating patch and a

ground plane. A 50 Ω transmission line supplies power to the patch, and both conductive layers utilize ITO transparent conductive films. A prototype of Ant1 was created through an in-house photolithography process that involved applying a photoresist layer to the ITO glass, exposing it to UV light, and subsequently etching it with hydrochloric acid to form the ITO pattern. On the other hand, ITO can also serve as an effective microwave absorption materials (MAMs). In a novel study [26], researchers demonstrated the use of 2D conformal microwave absorbing material fabricated on an ITO layer for designing a portable anechoic chamber. This absorber, optimized with a dipole-like resonance structure, delivers broadband absorption across 0.7 to 18 GHz. The innovative MAM was applied to the chamber's walls, achieving precise measurements of antenna performance, including return loss and radiation patterns, for various frequencies. This work expands the applications of ITO beyond antennas to high-performance microwave absorption.

Despite ITO's widespread use in transparent antennas and microwave components, its brittleness and the high cost of indium, a rare-earth element, pose significant limitations. As a more practical alternative, conductive meshes have emerged, offering cost-efficiency and ease of fabrication through additive manufacturing. This approach aims to maintain high transparency while optimizing RF performance.

2.2.2 Conductive Meshes

Antenna designs utilizing the mesh-grid technique offer notable benefits, including ease of fabrication, cost-effectiveness, and enhanced conductivity. Notably, a trade-off exists between reducing grid size to improve conductivity and maintaining optical transparency. Metal mesh antennas, composed of conductive grids, enhance electrical conductivity by providing more interconnected pathways for current flow. However, as the mesh size decreases, the density of conductive lines increases, leading to greater

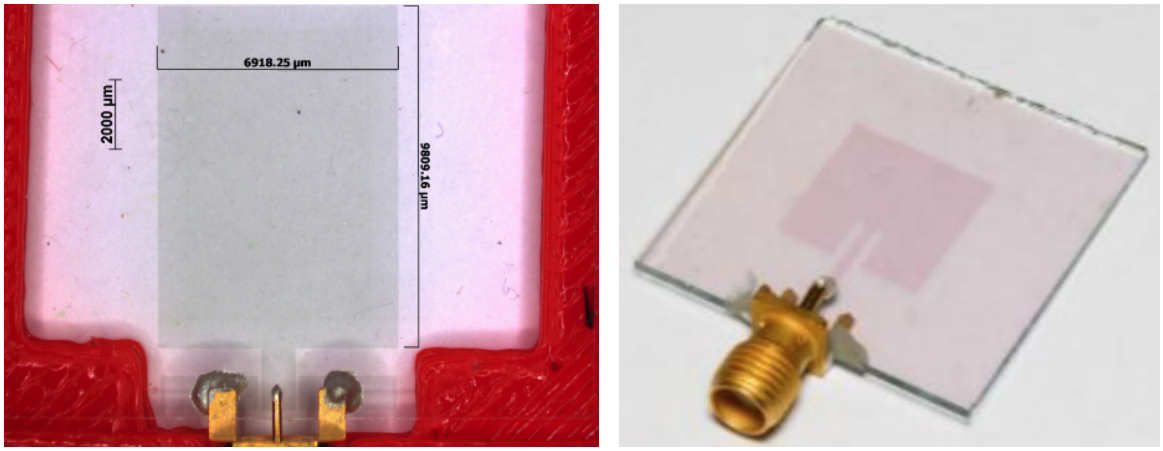

(a) **(b)**

Fig. 2.2. Images of ITO based antenna examples from (a) [24] and (b) [25].

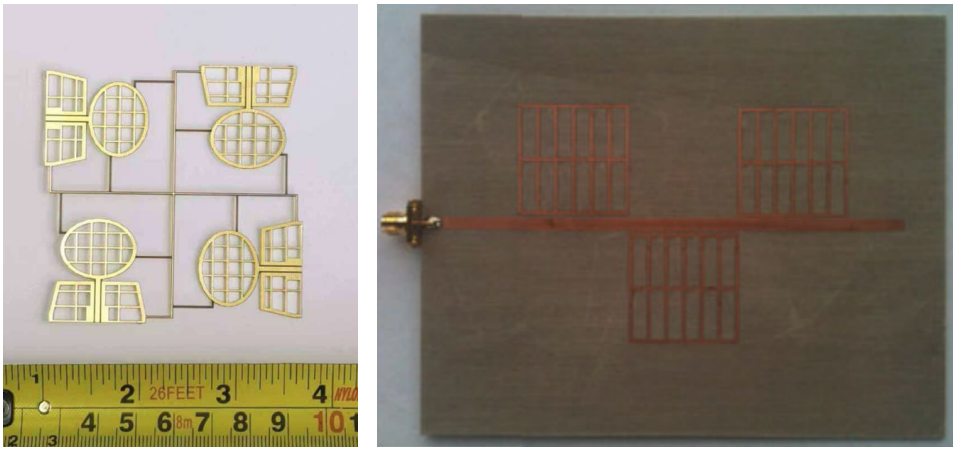

(a) **(b)**

Fig. 2.3. Images of proposed mesh antennas: (a) [27] and (b) [28].

optical obstruction and reduced transparency. Conversely, larger mesh sizes allow more light to pass through, improving optical transparency, but may result in higher electrical resistance due to the reduced number of conductive pathways. Optimizing mesh design requires balancing these factors to achieve the desired performance for specific applications.

Several studies have explored the use of meshed transparent antennas in various applications. In [27], an ultra-wideband (UWB) multiple-input and multiple-output (MIMO) antenna is introduced, employing a metal mesh structure to optimize performance while preserving transparency. This design, illustrated in Fig. 2.3a, achieves a transparency of 73% for individual elements and 77% for the entire MIMO array, with an operational bandwidth of 3.2 to 11.2 GHz. Another recent study [28] addresses the limited impedance bandwidth of meshed patch antennas, particularly for CubeSat applications, which is also a key focus of this thesis. The solution involves designing three differently sized meshed patch elements, expanding the bandwidth to 2.5 times that of a single-element patch. As shown in Fig. 2.3b, the design maintains high transparency, making it well-suited for integration with CubeSat solar panels, and uses a coplanar proximity feed to ensure smooth system integration.

Meshed antennas for space applications encounter several challenges before deployment. They require rigorous space qualification testing to ensure consistent printing processes and material properties that meet mechanical, thermal, and electrical standards. Materials must resist ionizing radiation, as exposure can degrade performance, while thermal stability is essential to withstand extreme temperature fluctuations without delamination or warping. Additionally, inks must exhibit strong adhesion and endure mechanical stresses during launch while resisting dust and moisture. The quality of printed patterns significantly impacts electrical performance,

where inconsistencies can compromise impedance and gain. While ink printing offers flexibility, achieving the necessary resolution and pattern fidelity is crucial. Despite these challenges, advancements in material science and printing techniques are vital for the successful integration of ink-printed mesh antennas in future space missions.

2.3 Choosing the Right Printer and Material

Transparent antennas often rely on specific substrates that ensure optimal performance while maintaining visual transparency. These substrates must possess specific properties, including high light transmission, mechanical strength, and suitable thermal resistance. Additionally, they need to have favorable dielectric characteristics to support efficient operation at various frequencies. When selecting a substrate, it is crucial to consider these factors to achieve effective integration of the antenna into its intended environment without compromising its functionality or aesthetics.

Glass is a widely utilized material in the design of transparent antennas due to its inherent optical transparency and favorable mechanical properties. Its high light transmission allows for minimal interference with the passage of light, making it an ideal choice for applications where maintaining visual aesthetics is crucial, such as in buildings, vehicles, and consumer electronics. Glass can also offer durability and resistance to environmental factors, ensuring the longevity of the antenna system. Numerous glass samples have been utilized in the literature for designing antennas and RF components [29]. These include various types of soda-lime float glass, such as clear and tinted variants, low-iron content extra clear glass, and coated glasses for heat protection [30]. By evaluating the relative dielectric constant and loss tangent of these glass substrates over a wide frequency range, from MHz to GHz, researchers have been able to assess their suitability for RF applications. This approach allows for precise modeling and optimization of antenna performance on different glass materials, demonstrating the versatility of glass as a substrate in RF design.

We chose to work with Schott Borofloat® 33 glass [31] samples due to their superior material properties, making them an ideal substrate for antenna design. Borofloat® 33 offers excellent thermal stability, low thermal expansion, and high resistance to both chemical and environmental factors, ensuring reliable performance in harsh conditions. Its high transparency across ultraviolet, visible, and infrared wavelengths makes it well-suited for optoelectronic applications, while its low alkali content ensures effective electrical insulation, which is crucial for RF components. Additionally, its excellent flatness, optical clarity, and surface quality make it suitable for precise electromagnetic simulations and enhanced antenna performance. These characteristics make Borofloat® 33 a versatile and reliable material choice for advanced antenna designs, particularly in high-performance RF and wireless systems.

The relative permittivity ($\epsilon_r = 4.46$) and loss tangent ($\tan\delta = 0.006$) were taken from the CST simulation library, which already defines these parameters for Borofloat® 33. Upon obtaining the glass samples, the dielectric properties of the substrate were initially evaluated through both simulations and measurements using a two-port prototype fabricated on 1.75 mm-thick samples. Fig 2.4 presents the photograph of the two-port network, including an open stub, alongside the transmission coefficient plots for both simulated and measured results. As shown in the plots, a strong agreement was observed between the simulated and experimental data, confirming the accuracy of the design and validating the suitability of the glass substrate for further investigation. No significant discrepancies or issues were identified during the evaluation process.

The subsequent phase in the development of antennas is manufacturing, which encompasses a systematic process involving various stages and techniques. Commonly employed materials for antenna fabrication include metals such as copper and aluminum for the radiating elements, as well as dielectric substrates like FR-4 or ceramic, which are selected based on the specific frequency and application requirements. The production process frequently utilizes techniques such as photolithography, etching, and milling for fabricating metal components, in conjunction with traditional PCB (Printed Circuit Board) fabrication methods for printed antennas. In instances where complex geometries are required, advanced manufacturing methods such as 3D printing can be employed to create intricate designs. In this context, we considered the application of circuit printers to facilitate the realization of low-cost antennas that can be printed on the surface of glass

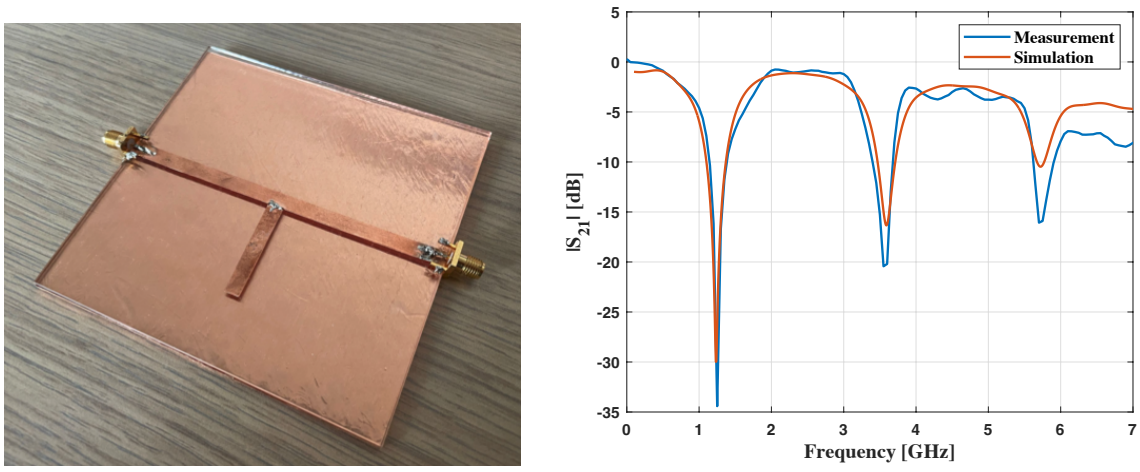

(a) **(b)**

Fig. 2.4. (a) Photo of the two-port network placed on the 1.75 mm-thick glass substrate, and (b) simulated and measured transmission coefficients of the two-port prototype.

substrates. Low-cost circuit printers, often referred to as PCB printers, represent an emerging technology that streamlines the fabrication of electronic circuits, particularly for small-scale production. These printers enable the direct printing of circuit patterns onto substrates using conductive inks, thereby enhancing the PCB manufacturing process. Utilizing either inkjet or laser printing technologies, these devices facilitate the deposition of conductive materials, with inkjet printers utilizing specialized conductive inks and laser printers adapted for toner transfer onto suitable substrates. Notably, low-cost circuit printers are characterized by their user-friendly interfaces and compatibility with widely used PCB design software, promoting accessibility in circuit design and fabrication. While these printers present a cost-effective solution for rapid prototyping and small-batch production, they are subject to limitations concerning precision, layer thickness, and material compatibility, which may constrain their application in high-frequency or complex multi-layer designs.

The use of circuit printers for antenna fabrication remains relatively uncommon, though several studies [32] in the literature indicate promising directions for further exploration in this innovative field. In this context, the Voltera V-One [33] circuit printer was chosen for its ability to rapidly prototype printed electronics. It is noted for its precision in printing conductive traces on various substrates, making it ideal for cost-effective, custom circuit production. Its application is particularly advantageous in

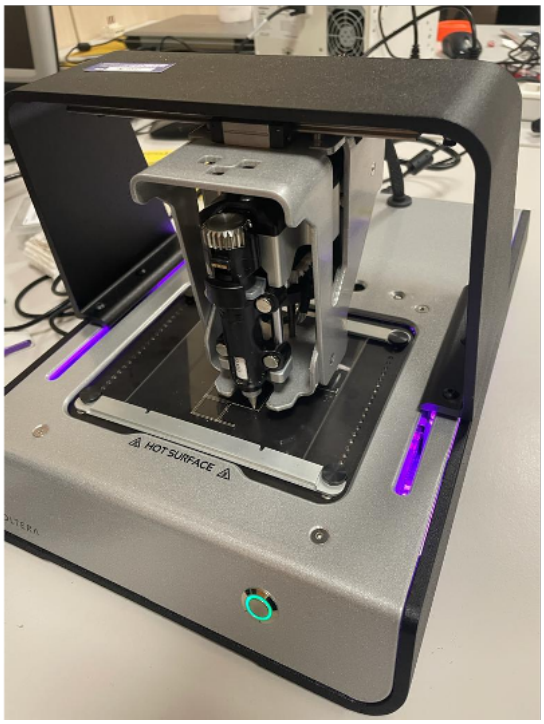

(a)

(b)

(c)

Fig. 2.5. (a) Image of the Voltera V-One circuit printer, (b) image of the Borofloat® 33 glass substrate sample, and (c) image of the flexible conductive ink used in the printing process.

research environments, where quick prototyping and iterative testing are critical. The decision to use the V-One, shown in Fig. 2.5a, was driven by its proven ability to fabricate high-quality, functional antenna structures, aligning with the specific requirements of this project. It is important to note that, given the printer's maximum printing area of 128 x 116 mm^2 [33], the glass substrate samples, shown in Fig. 2.5b, were chosen with dimensions of 11 x 11 cm^2 to ensure compatibility with the Voltera V-One circuit printer. Additionally, the conductive ink used, shown in Fig. 2.5c, is a flexible ink composed of tin, bismuth, and silver. The choice to use this ink was primarily due to its availability.

The integration of advanced manufacturing techniques, particularly the use of circuit printers, aligns closely with the design and simulation of meshed antennas. By leveraging the Voltera V-One circuit printer, we can fabricate intricate mesh designs that maximize the balance between transparency and electromagnetic performance. This seamless transition from simulation to fabrication enables the optimization of key performance metrics, including bandwidth and efficiency, while maintaining the aesthetic requirements essential for transparent applications. Consequently, the implementation of circuit printing technologies not only supports the physical realization of our antenna designs but also fosters innovation in the integration of meshed structures into a variety of environments, paving the way for future research in transparent antenna systems.

2.4 Design and Simulation of Meshed Antennas

Given the need for high antenna gain in the intended application, a two-element array design was selected for its balance between simplicity and compactness. A meshed, transparent patch antenna array was designed using CST Studio Suite, a full-wave electromagnetic simulation tool. The design process began with a solid patch, which provided an initial estimate for the required dimensions to achieve the desired resonance frequency. The patch was then modified using a meshing technique. Fig. 2.6 illustrates the antenna's geometry, including its key dimensions, where "G" and "W" represent the gap and line widths, respectively. As shown, the gap is narrower at the patch edges to fit within the specified dimensions, which correspond to a resonance frequency of 2.4 GHz. The design features meshed radiating elements and a feeding network, consisting of two $100\,\Omega$ branches that connect the antenna elements to a central $50\,\Omega$ transmission line. To accommodate soldering of the SMA connector, a solid section of the transmission line was incorporated.

Initially, the design process considered the implementation of a meshed ground plane to complement the meshed antenna structure. The intention was to maintain the overall transparency of the system while providing a stable ground reference for the antenna.

However, as the design evolved, the potential of utilizing the conductive back contact of the solar panel as the ground plane emerged as a promising alternative. Given the structural and electrical properties of the solar panel's back layer, it was hypothesized that it could function as an effective ground plane, eliminating the need for a separate meshed ground structure and simplifying the overall design. Therefore, this chapter confirms that the solar panel's back contact is a viable solution for the ground plane, allowing us to move forward with this simplified, yet highly effective, configuration in the final antenna design.

The filling factor plays a crucial role in enhancing the optical transparency of the antenna and is mathematically defined as $\frac{W}{W+G}$ [34]. This factor essentially determines the proportion of conductive material in relation to the open space, directly influencing how much light can pass through the antenna structure. However, the overall optical transparency of the antenna, denoted as T_{ant}, is not solely dependent on the filling factor. It also incorporates the transparency of the substrate material itself, T_{sub}. Therefore, the total optical transparency can be expressed as:

$$T_{ant} = T_{sub}(1 - \frac{W}{W+G})^2 \tag{1}$$

From this equation, it is clear that a lower filling factor, achieved by minimizing the line width W relative to the gap G, is beneficial for maximizing optical transparency. Essentially, as the conductive lines become narrower compared to the gaps, more light is allowed to pass through, improving the transparency. It is important to emphasize that optical transparency in this context refers to the transmission of light across a broad range of wavelengths, from ultraviolet (UV) to infrared (IR) [35]. This is

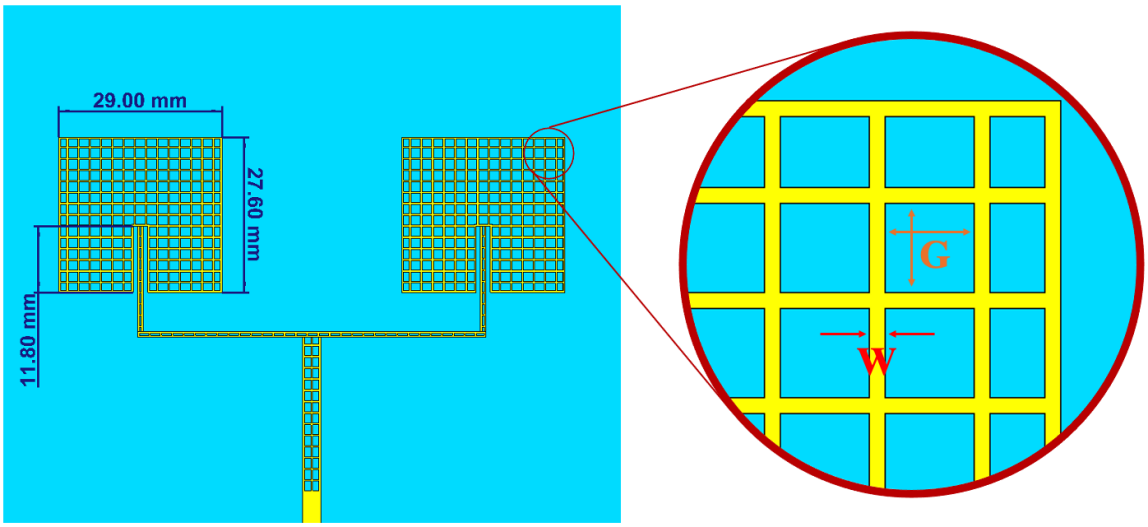

Fig. 2.6. The layout of the designed antenna array along with an explanation of the design parameters [17].

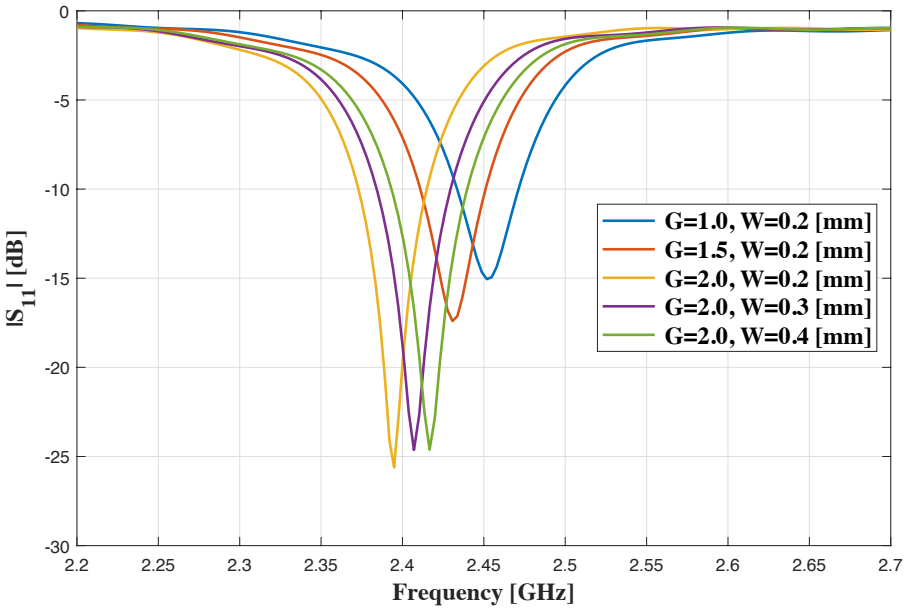

Fig. 2.7. Simulated reflection coefficients of the meshed antenna array for different values of gap width G and line width W [17].

Table 2.1. Overview of Antenna Performance [17]

Mesh Variables		**Performance Parameters**		
G [mm]	***W [mm]***	***Gain [dB]***	***Rad. Eff. [%]***	T_{ant} ***[%]***
1.0	0.2	7.4	74.8	63.9
1.5	0.2	7.1	71.6	71.6
2.0	0.2	6.6	68.0	76.0
2.0	0.3	6.9	70.5	68.6
2.0	0.4	7.1	71.9	61.6

particularly significant for applications like solar cell integration, where maximizing the transmission of sunlight is essential. However, the width of the conductive lines, W, is often limited by the resolution of the printing technology used in fabrication, which poses practical constraints on how small W can be made. Balancing the need for fine resolution with the printing limitations is a key design challenge in optimizing both the antenna's electromagnetic performance and its transparency.

Various meshed structures were simulated while keeping the width and length dimensions of the patch antenna constant. However, the line width W and gap width G were varied to observe their effects. Fig. 2.7 presents the resulting frequency shift in the reflection coefficient as these mesh parameters are altered. Notably, the resonance frequency decreases as the gap width increases and the line width decreases, indicating a sensitivity to these design variables. Further analysis of the antenna's performance is detailed in Table 2.1, which outlines the simulated gain, radiation efficiency at 2.4 GHz,

and the calculated optical transparency for different combinations of line and gap widths. The overall optical transparency of the antenna, T_{ant}, is calculated using (1), with T_{sub} assumed to be 92%, corresponding to the transparency of Borofloat® 33 glass.

As the gap width increases, the optical transparency improves, but this comes at the cost of reduced antenna gain and radiation efficiency. Conversely, increasing the line width results in a decrease in transparency but leads to improved antenna gain and radiation efficiency. This trade-off between optical transparency and antenna performance becomes a crucial design consideration. The final design of the array strikes a balance between these factors, achieving 68.6% optical transparency with a gap width $G = 2.0$ mm and a line width $W = 0.3$ mm. This selected configuration optimizes the antenna's performance while maintaining a satisfactory level of transparency for applications such as integration with solar cells.

2.5 Antenna Manufacturing and Evaluation

The proposed meshed microstrip antenna array was fabricated using a Voltera V-One circuit printer on a Borofloat® 33 glass substrate with a thickness of 1.75 mm. A flexible conductive ink, composed of tin, bismuth, and silver, was directly printed onto the glass substrate. The printing process took approximately 10 minutes, after which the printed ink was cured at a temperature of 160°C for 45 minutes to ensure proper adhesion and conductivity. Fig. 2.8a showcases the fabricated antenna, emphasizing its transparency, which is a key feature of the design. The transparent nature of the antenna makes it ideal for applications that require minimal interference with light, such as those involving solar panels or other optically sensitive components.

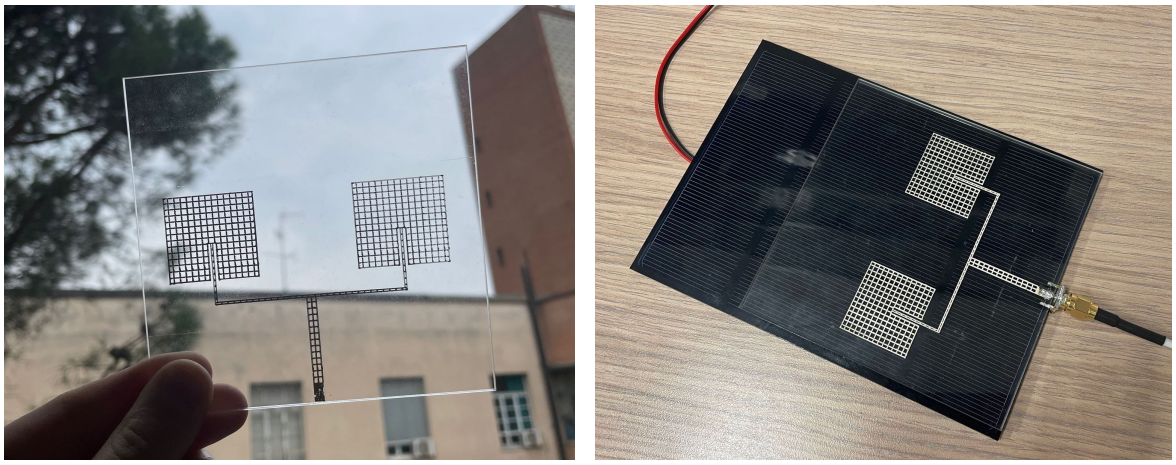

(a) **(b)**

Fig. 2.8. Images of (a) the printed meshed antenna array and (b) the antenna measurement setup with the solar cell in place [17].

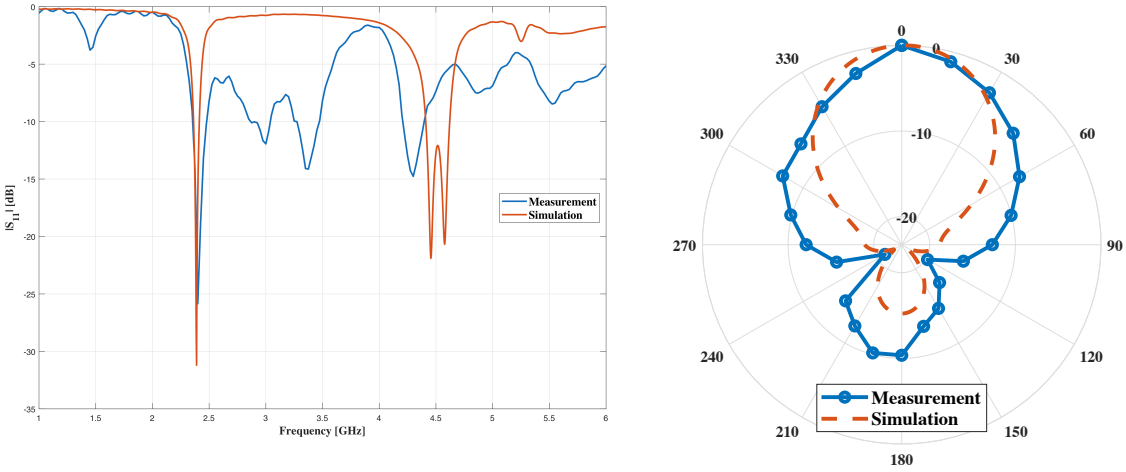

(a) (b)

Fig. 2.9. The plots of simulated and measured (a) reflection coefficients and (b) the normalized radiation patterns in the H-plane [17].

2.5.1 Contrasting Experimental Findings with Simulated Results

As previously discussed, the meshed antenna is positioned atop the solar panel, with the aluminum layer of the panel serving as the antenna's ground plane. The configuration for the antenna measurement is illustrated in Fig. 2.8b, while Fig. 2.9a presents the simulated and measured reflection coefficients S_{11} over a frequency range of 1 to 6 GHz. It is important to note that the exact layer composition of the solar panel was not definitively known, and the simulations were conducted based on the assumption of using glass, silicon, and aluminum materials. Consequently, while the measurement results align closely with the desired frequency, some discrepancies are observed in specific frequency regions due to the uncertainty regarding the solar cell's layer stack-up. Additionally, the normalized radiation pattern comparisons are provided in Fig. 2.9b, where minor variations can be attributed to potential imperfections in the printing process and the modeling of the solar panel within the simulation. These factors highlight the challenges in achieving precise correspondence between simulated and measured results, emphasizing the need for accurate material representation in simulations for improved predictive capability.

2.5.2 Impact on Solar Cell Efficiency

To evaluate the light transmission efficiency of the fabricated prototype and its impact on the power output of a solar cell, measurements were conducted using a 2.5 W solar panel made from single-crystal material, measuring 160 x 116 x 2.5 mm^3. This solar panel features a fine resin surface and has a solar energy conversion efficiency of 17%. The open-circuit voltage and short-circuit current of the solar panel were recorded both

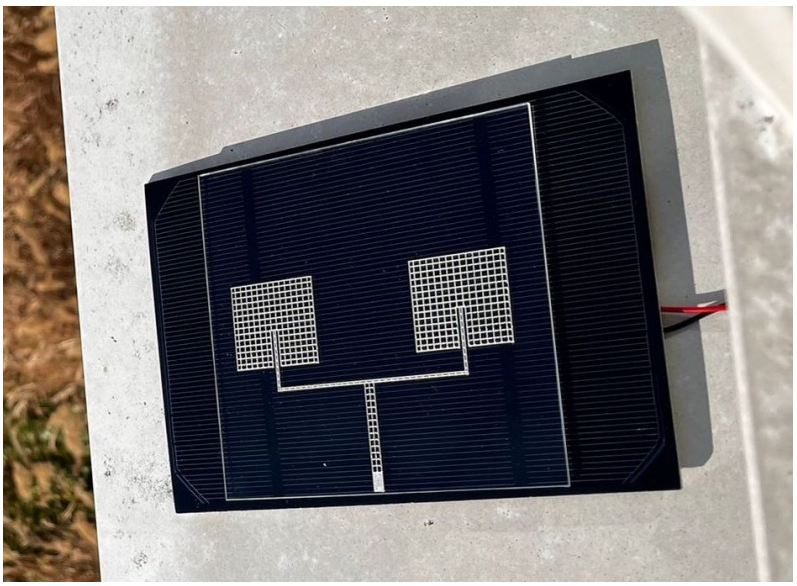

Fig. 2.10. Image of the solar panel with the transparent antenna positioned on top for solar cell measurements.

Table 2.2. Analysis of Solar Cell Performance [17]

	Open-circuited Voltage [V]	***Short-circuited Current [mA]***
Solar Panel Only	6.39	270
Solar Panel and Glass Only	6.32	250
Solar Panel and Transparent Antenna	6.24	230

with and without the transparent antenna positioned above it. The measurement setup is illustrated in Fig. 2.10, where the antenna is included. When the antenna was present, the recorded short-circuit current and open-circuit voltage of the solar panel were 230 mA and 6.24 V, respectively. Table 2.2 also presents data from tests conducted with only the glass substrate and the solar panel alone for comparison. In contrast, the solar panel, when tested independently, generated a short-circuit current of 270 mA and an open-circuit voltage of 6.39 V.

The introduction of the transparent meshed antenna array resulted in a reduction of 14.8% in the short-circuit current, while the drop in the measured open-circuit voltage was minimal at just 2.3%. It is important to note that the 11 x 11 cm^2 antenna covers approximately 70% of the solar panel's surface area. These preliminary findings provide encouraging evidence for the viability of integrating transparent antennas with solar panels, indicating that such a combination can effectively harness both solar energy and wireless communication capabilities without significantly compromising performance.

2.6 Conclusion of the Chapter

This work presents and experimentally validates the potential of developing a multilayer structure that effectively integrates solar cells with antenna systems. The integration employs printing techniques applied directly to the glass substrate, while also opening up possibilities for similar applications on the superstrate of the solar cell. This initial proof-of-concept demonstrates the feasibility of creating microwave antenna arrays that occupy the same area as existing solar cells. This configuration is designed to facilitate the harvesting of microwave energy or the retransmission of power stored in the solar cells by integrating suitable RF-to-DC converters between the overlapping layers. Importantly, the integrated system experiences only minimal performance degradation when the metal patterns of the antennas are carefully optimized. The cost-effective methodology used for the printed array has been validated through measurements, while more advanced yet expensive approaches can be readily scaled to support larger meshed antenna arrays.

This chapter represents the foundational investigation into the design and integration of meshed antennas with solar panels, marking the first significant step in this research. The outcomes of this study have laid the groundwork for the rest of the thesis, shaping the direction for further exploration and development. Based on the results achieved here, subsequent chapters will delve deeper into the practical applications of this technology, particularly in space environments where the integration of antennas with solar panels can provide both functional and structural benefits. Additionally, further geometric enhancements, performance optimizations, and detailed calculations will be explored, aiming to refine the design and push the boundaries of what is achievable with meshed antenna technology in advanced RF systems.

3 Exploring In-Space Wireless Power Transmission Solutions for CubeSats

This chapter is based on the following article:

[36] A. B. Gok, D. Masotti, and A. Costanzo, "Preliminary study of an in-space wireless power transmission for cubesats," in *2023 IEEE International Conference on Wireless for Space and Extreme Environments (WiSEE)*, 2023, pp. 99–104.

3.1 Introduction to the Chapter

In recent years, nanosatellites have become an integral component of spacecraft technology, driven by advancements in the miniaturization of electronic components and the increased demand for smaller, more cost-effective space missions. Among these nanosatellite platforms, the CubeSat standard has played a transformative role in democratizing satellite technology, offering a modular, compact, and low-cost alternative for space-based research and communication systems. However, as space missions evolve and the need for more sophisticated onboard instrumentation grows, larger and more complex CubeSat designs are increasingly replacing their smaller counterparts. These advanced systems often require additional space and power to accommodate the payloads, whether they are next-generation communication equipment or specialized measurement instruments. This shift has led to challenges in power management, as the energy demands of larger payloads surpass the capacity provided by the small, surface-mounted solar cells typically used in CubeSat missions.

Furthermore, while CubeSats were initially developed for Low Earth orbit (LEO) applications, recent missions, such as NASA's MarCO mission [37], have demonstrated their potential for deep space exploration. As these missions venture further from the Sun, the limitations of solar panels as a primary power source become increasingly evident. Solar panels, which convert sunlight into electrical power, are subject to temperature fluctuations and, more critically, to the inverse square law, which states that the intensity of solar radiation decreases as the square of the distance from the Sun increases. This reduction in available solar energy, combined with extreme temperature variations in deep space, can significantly impact the efficiency and performance of solar cells, leading to power deficiencies for nanosatellites operating beyond LEO.

To address these challenges, integrating transparent antennas into the satellite structure has emerged as a promising solution. Transparent antennas, designed to be nearly invisible and seamlessly integrated into surfaces like solar panels, offer a dual-function approach by enabling both WPT and traditional solar power generation.

These antennas, constructed using meshed conductors, allow light to pass through while still functioning effectively as radiating elements for microwave frequencies. This design not only maintains the functionality of the solar cells but also enables new possibilities for power management in space. Transparent meshed antennas can be manufactured using cost-effective methods such as screen printing or inkjet printing, making them accessible for small-scale production and research purposes [38].

One of the primary challenges associated with WPT in space is the significant power loss over long distances. However, recent research [39] suggests that this issue can be mitigated by deploying a network of power relay nodes along the transmission path. In this scenario, small satellites could function as relays, as shown in Fig. 3.1, by receiving power from a central source and redistributing it to nearby nodes or satellites, thereby ensuring a more efficient and continuous power flow throughout the network. This concept has the potential to enable long-range WPT in space, allowing nanosatellites to function effectively in both power-receiving and power-transmitting modes, thereby extending the operational range of space missions without relying solely on solar power.

This part of the thesis presents a comprehensive feasibility study of a solar-powered rectenna/transmitter system for in-space applications. The study evaluates the performance of a transparent WPT transceiver integrated with solar cells, considering key factors such as power generation, transmission efficiency, and subsystem interactions. By conducting detailed simulations and power calculations, the goal of this work is to establish realistic link budgets for different satellite constellation

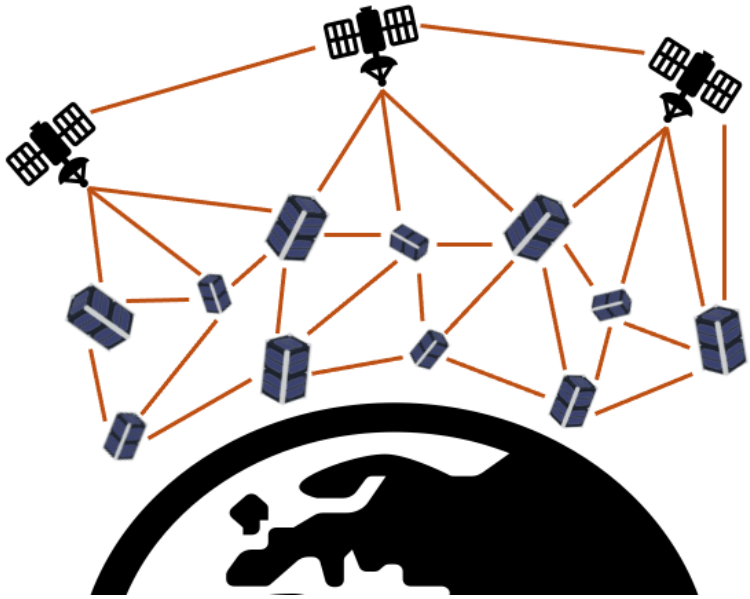

Fig. 3.1. Schematic representation of power relay mechanism among small satellites, showcasing their role in redistributing energy from a central source to enhance network efficiency [36].

scenarios and provide estimations for applicable WPT link distances. This research aims to contribute to the development of sustainable power solutions for nanosatellites, particularly in deep space missions where traditional solar power systems face inherent limitations. However, the successful deployment of such systems requires an in-depth understanding of overall energy management, as power generation is only one aspect of ensuring the continuous operation of nanosatellites in harsh space environments.

In the following section, comprehensive energy management strategies that address both generation and consumption are explored, focusing on how the limited power available can be efficiently stored, distributed, and utilized by nanosatellites.

3.2 Energy Management for Nanosatellites

The increasing demand for advanced communication systems in space has amplified the power requirements for satellites of all sizes, especially nanosatellites. As the technological capabilities of these small spacecraft continue to evolve, so do the expectations for higher data transmission rates, longer mission durations, and more sophisticated on-board instruments. However, the compact dimensions of nanosatellites inherently restrict the available surface area for power generation, making it difficult to produce sufficient energy to support high-data-rate communication links. This limitation becomes particularly evident when these nanosatellites are tasked with handling complex payloads, maintaining continuous contact with ground stations, or operating in multi-satellite constellations that require constant inter-satellite communication.

The primary source of energy for nanosatellites is solar panels, which convert sunlight into electricity to power essential subsystems. However, the small size of the satellite's body means that the available area for solar cells is limited, leading to a constrained energy budget. As a result, there is often insufficient power to meet the growing needs of energy-intensive tasks, such as data processing, long-range communication, or running scientific instruments. This power shortfall becomes even more critical in missions that demand consistent high-performance communication, where power-hungry transmitters and receivers must operate for extended periods.

To effectively address this power deficiency, it is essential to carefully analyze the power consumption of various satellite subsystems and prioritize their energy needs. By doing so, satellite designers can not only optimize the existing power resources but also explore innovative solutions to enhance energy efficiency. The development of more efficient solar panels, energy storage systems, and power management techniques could help maximize the limited energy resources available to nanosatellites, ensuring their ability to perform high-data-rate communication tasks without compromising other critical functions. The challenge of balancing compact size with the increasing

power requirements remains a key consideration in the ongoing advancement of nanosatellite technologies.

As outlined in the power budget of a 2U CubeSat detailed in [40], the peak power requirement for the primary payload, which monitors the time-resolved flux of atomic and molecular oxygen in the space environment, is approximately 3 W. However, this power demand can fluctuate based on factors such as the satellite's size, the complexity of the payload, mission objectives, and the specific components involved in the system. It becomes evident that even an additional 1 W of power could significantly enhance the satellite's overall functionality. Consequently, a key objective of this study is to explore potential solutions and perform a thorough analysis aimed at generating an extra 1 W of power for CubeSat operations.

From an alternative viewpoint, it is essential to recognize that satellites undergo substantial periods of eclipse throughout their orbital journeys, a phenomenon influenced by both their altitude and geocentric angle in relation to the Sun [41]. During these eclipses, satellites cannot harness solar energy, forcing them to depend on onboard batteries for power. This reliance presents a significant challenge, as many satellites are required to transition into low-power modes, which severely limit their operational capabilities and functionality. The inherent dependence on batteries in the harsh environment of space introduces several complications. For instance, the performance of batteries can be significantly impacted by extreme conditions such as intense radiation exposure, which can lead to capacity degradation and a reduction in overall lifespan. Additionally, during eclipse periods, temperatures can plummet to levels that may cause permanent damage to battery cells. This dual threat of radiation and low temperatures underscores the critical need for robust thermal management systems and advanced battery technologies that can withstand such extremes. Consequently, effectively managing power systems during eclipse phases is vital for ensuring continuous satellite operation, longevity, and overall mission success in the demanding conditions of space.

The challenges outlined above highlight the urgent need to address the high power requirements of nanosatellites. Current literature has explored the potential of WPT technology as a viable solution for powering small satellites, particularly through the use of laser beams emitted from larger satellites [42]. However, given the recent increase in CubeSat deployments, there is a compelling case for implementing microwave-based WPT systems. As the distances between these satellites continue to decrease, the feasibility of microwave power transfer becomes increasingly viable. Moreover, in certain swarm formations [43], CubeSats can be deployed in close proximity to one another, often just a few meters apart, allowing for collaborative operations such as formation flying or distributed sensing. This close range creates opportunities for inter-satellite power transfer, catering to the relatively lower power

demands typical of such systems. Therefore, this work aims to explore and develop innovative solutions for inter-satellite power distribution, leveraging the advantageous positioning of CubeSats in close formations to enhance their operational capabilities and sustainability in space.

In particular, the design of transparent meshed radiating elements will play a vital role in facilitating efficient energy transfer among satellites. The subsequent chapter will delve into the intricacies of developing transparent antennas, highlighting their importance in achieving both aesthetic and functional objectives in space applications. This exploration will encompass the design principles, material considerations, and performance metrics essential for optimizing the efficacy of transparent antennas in the context of advanced nanosatellite missions.

3.3 Optimizing Transparent Radiating Elements

In the previous chapter, we explored the design of a meshed antenna element as an initial step in the development of transparent antenna technology. While that investigation laid the groundwork for understanding the fundamental principles of meshed transparent antennas, the current study takes a more comprehensive and multifaceted approach to further this concept. This work delves deeper into the design intricacies, considering more detailed geometrical aspects of the antenna. Additionally, it examines performance across a range of frequencies and antenna sizes, offering a broader perspective on how these elements can be optimized for various applications.

As mentioned, the ultimate goal of this investigation is to create a hybrid solar-powered WPT transceiver by integrating a transparent rectenna system with a fully functional solar cell. The rectenna will serve the dual purpose of either collecting or radiating EM energy, allowing for a seamless blend of energy harvesting and communication capabilities. The first phase of this integration involves designing a meshed patch antenna on a borosilicate glass substrate, with a solar cell mounted directly underneath. This design offers a compact and efficient solution, as both the antenna and solar cell share the same physical footprint, significantly reducing the overall space required for the system.

A key innovation in this design is the use of the solar cell's highly reflective aluminum layer as the ground plane for the meshed patch antenna. This allows for a conformal and streamlined installation, making it suitable for space-constrained applications, such as nanosatellites or CubeSats. Furthermore, experimental results from the previous chapter have already validated the practical feasibility of integrating transparent antennas with solar panels, confirming that the proposed structure offers a promising solution for efficient energy transfer and communication. This broader investigation builds upon those initial findings, refining the design and expanding its

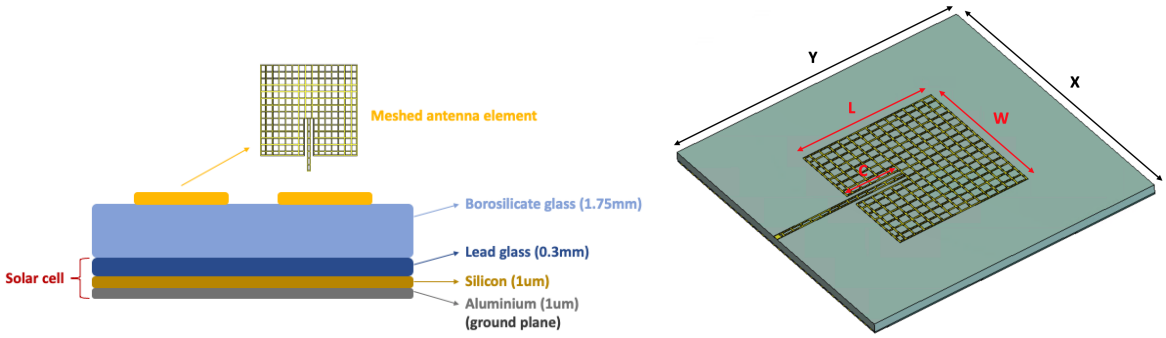

Fig. 3.2. (a) Stacked configuration of the meshed patch antenna and (b) top view of the antenna element structure. [36].

applicability across different operating conditions and environments.

The chosen antenna topology for this work is a meshed patch antenna, which can be fabricated using printing technology on a Borofloat® 33 glass material with a thickness of 1.75 mm and a copper layer of 35 µm, same as before. The stacking assembly of the meshed patch antenna, which is integrated with a solar cell, is illustrated in Fig. 3.2a. This assembly is inspired by the structure of conventional silicon-based solar cells and incorporates various layers to optimize performance. The overall effectiveness of such stacked-patch antennas is heavily influenced by the dielectric constant and thickness of each layer in the design. In line with the approach described in [44], the electromagnetic simulation of this structure—conducted using CST—relies on a simplified material stack consisting solely of aluminum, silicon, and glass layers. This selective use of materials minimizes computational complexity while still providing accurate simulation results.

Among the layers in the assembly, the lead glass is the thickest and serves a dual purpose. Primarily, it acts as a protective cover for the solar cell, shielding it from potentially damaging solar radiation. However, this layer also plays a critical role in determining the antenna's performance, particularly its resonance frequency. The thickness and dielectric properties of the lead glass exert a significant influence on the antenna's electromagnetic behavior, making it a key factor in achieving the desired balance between antenna efficiency and solar cell integration. The careful consideration of each material in the stacking assembly ensures that the proposed meshed patch antenna maintains both its structural durability and high-frequency functionality in the demanding conditions of space.

The performance of a meshed patch antenna is closely influenced by the number of mesh lines and their respective widths, both of which must be carefully optimized to balance antenna gain and bandwidth while maintaining the desired level of transparency. In this design, the thickness of the mesh lines has been set at 0.3 mm, while the spacing between these lines is 1.7 mm. However, to preserve the detailed contour of the patch,

especially at the edges where precision is crucial for maintaining the correct resonance frequency, the line spacing is reduced in those regions. This ensures that the antenna's geometry is aligned with the operating frequency while preserving its transparency. To accurately predict the performance of the meshed antenna array, utilizing the same surface area as the solar panel, simulations were conducted at three different operating frequencies. These full-wave simulations allowed for a comprehensive analysis of how the meshed structure would perform in terms of both radiation efficiency and transparency. Fig. 3.2b provides a top view of the meshed antenna structure, giving a clear visual representation of the layout and configuration.

$$Transparency\ [\%] = (1 - \frac{Meshed\ Metal\ Area}{W \times L}) \times 100 \tag{2}$$

The transparency of each individual patch antenna element was calculated using (2), where the denominator corresponds only to the patch's total area. The meshed metal area was then determined by taking into account both the number of mesh lines and their respective thickness. It is important to note that the transparency calculation exclusively considers the area of each patch, without including surrounding elements or other components. This approach allows for a precise evaluation of how the meshed design impacts both the optical transparency and the overall electrical performance of the antenna, ensuring that the antenna remains functional while integrated with solar panels.

When interpreting the transparency values in this thesis, it is crucial to distinguish between the transparency equations. Equation (1) offers a theoretical value focused on the antenna design, specifically the line thickness in relation to the gaps, and it provides the transparency for the antenna's radiating elements only, excluding the full substrate area. In contrast, equation (2) is more practical, accounting for the total meshed metal area and the overall dimensions of the antenna element. While equation (2) gives a more comprehensive transparency estimate, it still applies solely to the antenna element and not the entire substrate. Therefore, it is important to handle these equations carefully and not confuse them, as they reflect different aspects of the design. Readers should pay attention to the context of each equation when interpreting the corresponding

Table 3.1. Single-Element Antenna: Performance Summary [36]

Frequency ***[GHz]***	***X*** ***[mm]***	***Y*** ***[mm]***	***W*** ***[mm]***	***L*** ***[mm]***	***C*** ***[mm]***	S_{11} ***[dB]***	***Gain*** ***[dBi]***	***Transparency*** ***[%]***
1.2	95	95	59.0	55.7	20.8	-19.6	3.6	68.6
1.8	70	70	39.0	36.8	14.5	-24.6	4.5	67.5
2.4	60	60	29.5	27.5	11.2	-26.5	4.6	67.4

transparency values presented in the tables.

Table 3.1 presents the performance metrics of the antenna elements operating at frequencies of 1.2 GHz, 1.8 GHz, and 2.4 GHz, alongside their respective dimensions. The table includes a detailed comparison of key parameters such as reflection coefficients and antenna gains, which were derived from the full-wave simulation results. Additionally, the calculated transparency values for each antenna element are provided, reflecting the extent to which the meshed structure maintains optical transparency while preserving functional efficiency. These performance metrics offer a comprehensive overview of how the antenna design varies across different frequencies, highlighting the balance between electromagnetic performance and transparency, which is critical for integrating the antenna with solar panels in space-based applications.

3.4 Evaluation of Large-Scale Antenna Arrays

To determine the number of antenna elements that can be deployed and to evaluate the performance of the antenna array, it is essential to first establish the available solar panel sizes. The size of the solar panels plays a crucial role in determining the potential integration of antenna elements. For a large satellite scenario, the Rosetta spacecraft (see Fig. 3.3a), operated by the European Space Agency (ESA), is considered. Rosetta was equipped with two expansive solar panels, each measuring approximately 14 meters in length and 2.2 meters in width, which provided the electrical power necessary for its mission throughout its journey [45].

In contrast, the performance predictions for a small satellite are based on the LunaH-Map (Lunar Hydrogen Mapper) (see Fig. 3.3b), part of NASA's CubeSat Launch Initiative [47]. This CubeSat, weighing approximately 14 kilograms and configured in a 6U form factor (about 30 x 20 x 10 cm^3), is planned to be deployed into lunar orbit as a secondary payload on a future mission. LunaH-Map is equipped with two uniquely shaped solar panels that unfold upon deployment. The largest uniform area on these solar panels, suitable for fitting an antenna array, is approximately 30 x 60 cm^2. These dimensions provide a more constrained space for antenna integration compared to larger spacecraft, necessitating careful design considerations to optimize both the antenna performance and its compatibility with the available solar panel area.

A comprehensive set of six array simulations was performed, encompassing three selected frequencies and two distinct solar panel sizes. To optimize the performance of the antenna array, the element spacing was deliberately set to half of the wavelength. This spacing choice is crucial as it maximizes gain in the primary radiation direction while minimizing mutual coupling between elements, which can adversely affect overall performance.

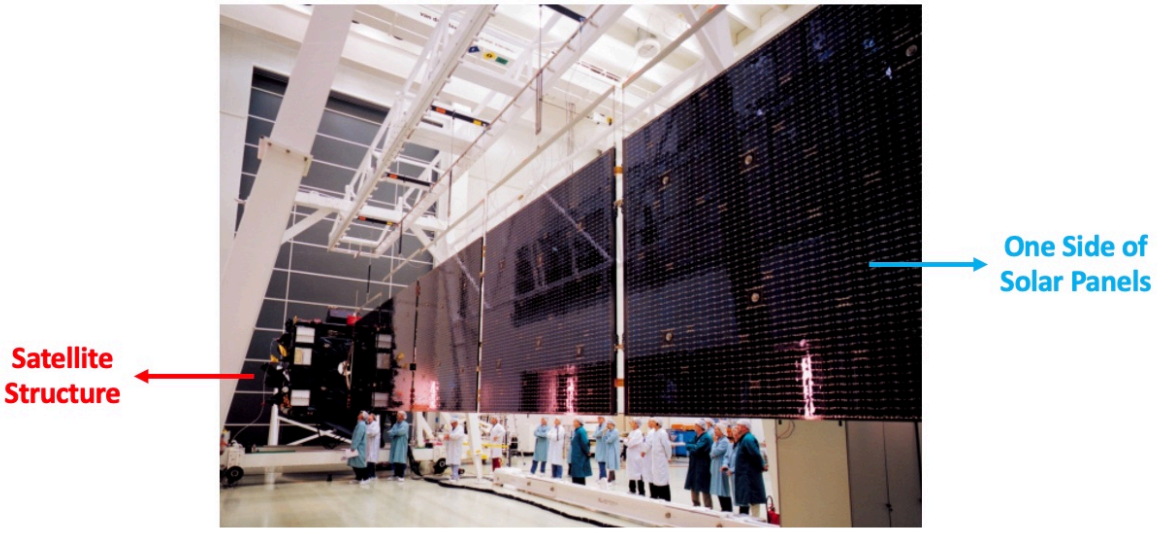

(a)

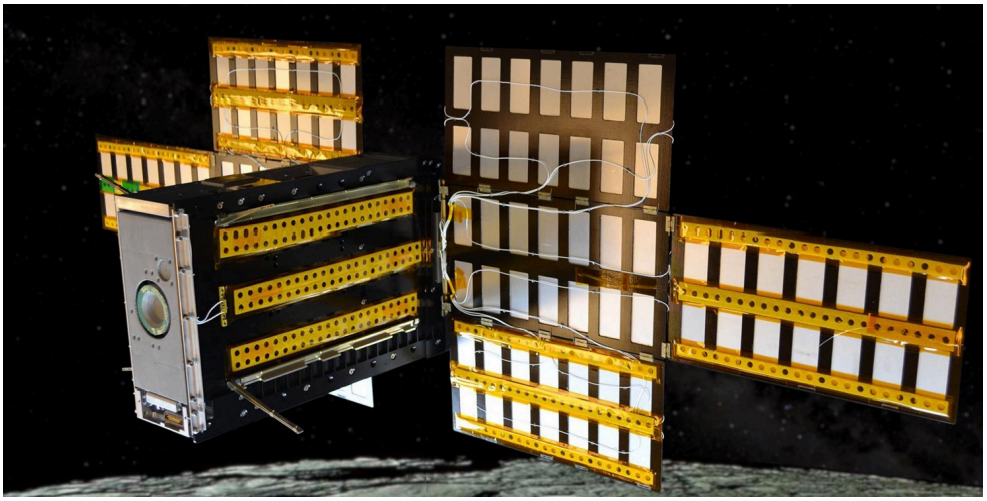

(b)

Fig. 3.3. Photos of (a) Rosetta spacecraft [46] and (b) LunaH-Map CubeSat [47].

Table 3.2. Performance Comparison of Antenna Arrays with Varying Element Counts and Frequencies [36]

Frequency [GHz]	*Satellite*	N_r	N_c	*Gain [dBi]*
1.2	**LunaH-Map**	2	4	11.6
	Rosetta	18	112	35.3
1.8	**LunaH-Map**	4	8	18.3
	Rosetta	26	168	39.5
2.4	**LunaH-Map**	4	10	19.3
	Rosetta	36	224	42.2

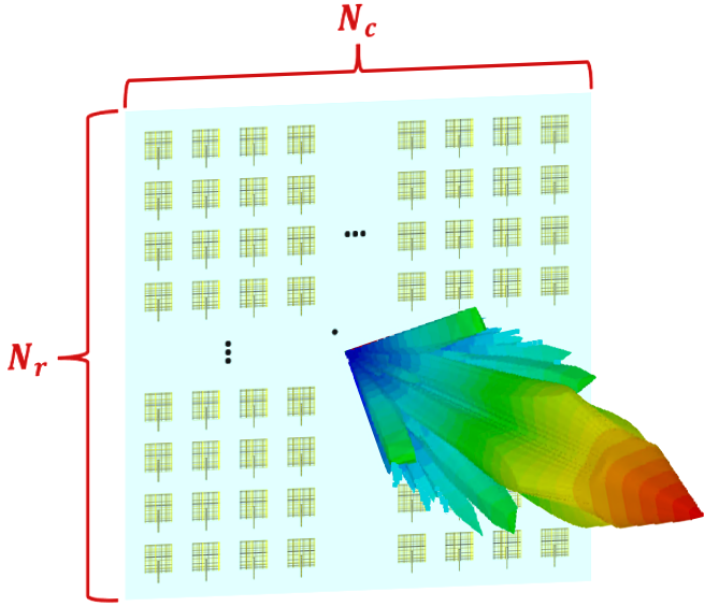

Fig. 3.4. Layout of the antenna array configuration illustrating the spatial arrangement of elements based on solar panel dimensions [36].

Table 3.2 provides a comprehensive summary of the antenna array performance across the configurations under study. For clarity, the dimensions of the solar panels (covering one side of each satellite) are specified as 30 x 60 cm^2 for LunaH-Map and 2.2 x 14 m^2 for Rosetta. The table also outlines the number of antenna elements in each configuration, denoted as N_r and N_c, representing the horizontal and vertical orientations, respectively, as determined by the operating frequency. For a visual reference, Fig. 3.4 illustrates the spatial layout of the antenna elements, designed to optimize performance across the selected frequencies. For example, at an operating frequency of 1.8 GHz, one side of the Rosetta satellite's solar panel can accommodate a 26 x 168 element array, yielding an antenna gain of 39.5 dBi.

The array simulations have demonstrated the impact of frequency and panel size on antenna performance, laying the foundation for effective integration into satellite systems. With these results, attention now turns to the inter-satellite link budget, which will assess the feasibility of power transfer between satellites in different scenarios.

3.5 Inter-Satellite Power Transfer Analysis

In the context of our study, an inter-satellite link budget refers to the detailed assessment and distribution of power resources within a satellite system, specifically aimed at supporting WPT between satellites. This involves analyzing key parameters such as transmitted power, antenna gains, path losses over varying distances, and the duration of satellite interactions. By conducting a thorough evaluation of these factors,

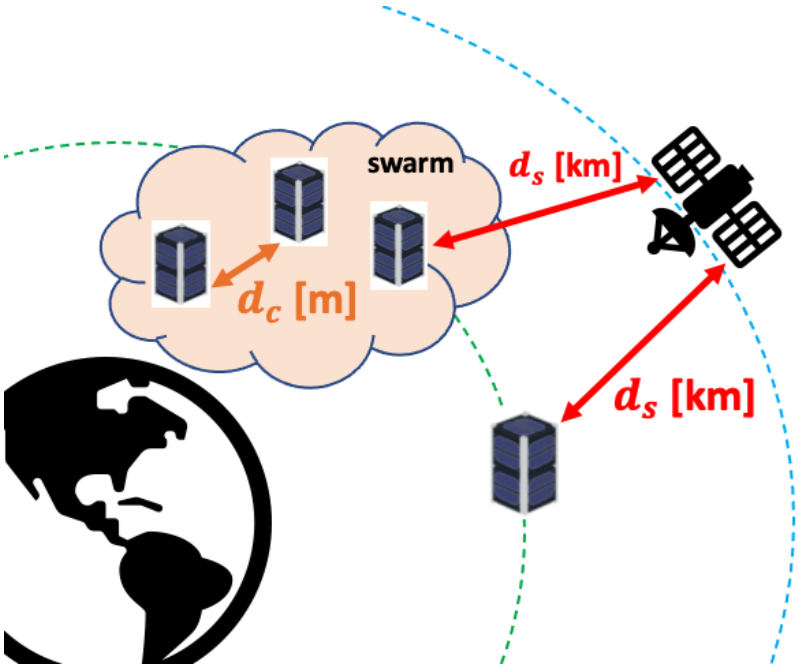

Fig. 3.5. CubeSat powering scenarios depicting WPT between a large satellite and CubeSats, and a swarm-based collaborative powering solution utilizing transparent antennas and solar panels [36].

it is possible to optimize the overall satellite constellation configuration, ensuring effective power distribution, system design, and resource management. Such considerations play a critical role in enhancing the efficiency and success of in-space WPT operations.

Fig. 3.5 illustrates two distinct CubeSat powering scenarios addressed in this work. The distance between satellites can vary based on mission objectives and the specific formation configuration, whether it involves a single large satellite, such as one in LEO, or a swarm (or cluster) of CubeSats. Given the current surge in the number of deployed satellites, particularly nanosatellites, which often operate in close proximity to one another, the concept of powering a CubeSat (or a swarm) using a larger satellite is increasingly feasible. Additionally, a second scenario explores the integration of transparent antennas with solar panels to enable collaborative power sharing among a satellite swarm. This approach leverages a power relay method offering a potential solution for coordinated power distribution within a satellite cluster. The distances between satellites, denoted as d_s and d_c in the figure, are determined based on the link budget calculations and the corresponding received power levels, providing insight into the feasibility of inter-satellite power transfer.

The distance calculations for the inter-satellite WPT scenarios are performed using the standard Friis transmission equation (3), with the results summarized in the link budget tables. These calculations take into account two distinct scenarios and three operating frequencies, offering a detailed analysis of potential WPT applications.

$$P_R = \frac{P_T G_T G_R \lambda^2}{(4\pi d)^2} \tag{3}$$

Scenario A involves RF power being transmitted from a larger satellite to a CubeSat, representing a one-way transfer from a more powerful platform to a smaller satellite. Scenario B, on the other hand, examines RF power transmission between two CubeSats within the same swarm, focusing on power sharing within a closely coordinated formation of smaller satellites. In both scenarios, the critical parameters influencing WPT performance include the transmitted power (P_T), the gain of the transmitting antenna (G_T), the gain of the receiving antenna (G_R), and the received power (P_R). These parameters are calculated based on specific system requirements and physical constraints. The distance between satellites, d, is determined according to the selected scenario, while the wavelength, λ, is calculated based on the chosen operating frequency.

An essential aspect of the WPT operation is that the power supplied for transmission must be harvested exclusively from the solar panels integrated into the satellite system. This power is then converted and regulated by a high-efficiency inverter, which drives the transmitting antenna array. The efficiency of the inverter is therefore a critical factor in determining the overall effectiveness of the power transfer process and is carefully considered in all performance evaluations.

The results presented in the link budget tables reflect the interplay between these factors, showing how different frequencies, distances, and antenna configurations impact the WPT efficiency for both scenarios. Furthermore, the transmission and reception antenna gains, as well as the available power from the solar panels, are modeled to reflect real-world constraints on satellite operations, ensuring that the scenarios remain practically viable. This investigation will further explore the specific trade-offs, challenges, and optimizations required to enhance WPT between satellites, particularly focusing on real-world applicability and the unique demands of space-based power systems. With this foundation in place, we now turn our attention to a comprehensive analysis of each scenario, breaking down the critical performance metrics and design considerations in greater detail.

3.5.1 Power Transmission from Primary Satellite to CubeSats

Most CubeSats are deployed in LEO to carry out a variety of missions, ranging from Earth observation and communication experiments to technology demonstrations and educational initiatives. CubeSats are often launched alongside larger spacecraft or from dedicated launch vehicles, and they can either enter their intended orbits directly or be released at a designated point to reach their operational altitudes. The distance

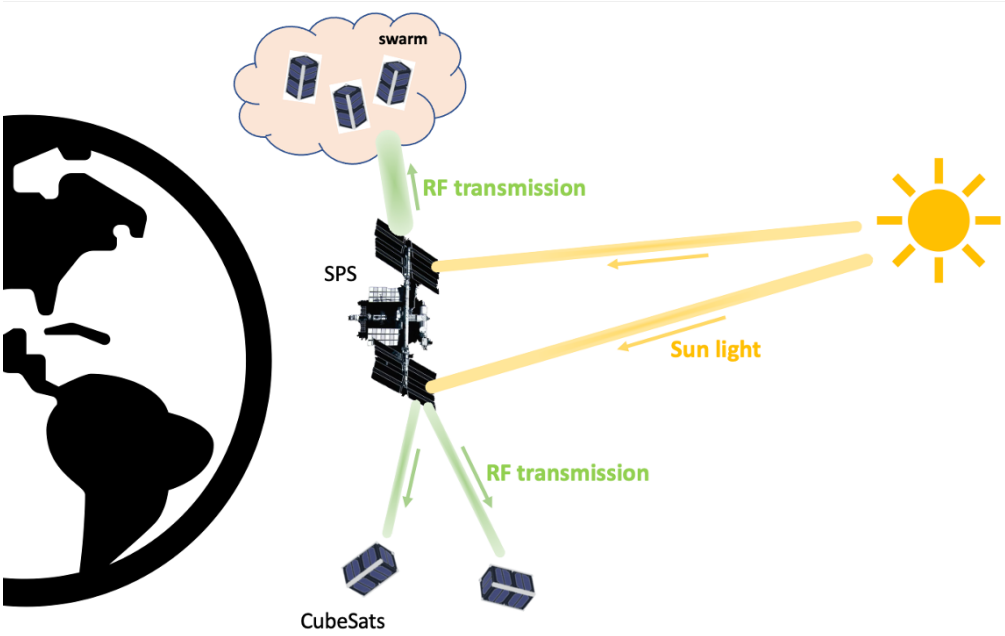

Fig. 3.6. CubeSat powering scenario depicting power transfer from primary satellite to a CubeSat or swarm of CubeSats.

between a CubeSat and a larger satellite can vary widely based on mission objectives and orbital configuration. In certain missions, CubeSats stay close to their host satellite, maintaining distances of only a few kilometers for formation flying or collaborative tasks, as depicted in Fig. 3.6. In other instances, the separation can extend to several hundred kilometers or even more, particularly when CubeSats are released to perform independent tasks. These distances are determined by factors such as mission type, communication range, and the operational needs of the CubeSat, ensuring that each satellite operates within its optimal environment while remaining within the broader mission framework. The dynamic nature of CubeSat deployment and operation in LEO makes them highly versatile for a wide range of space missions.

Satellite solar panels are engineered to optimize power generation while keeping overall weight to a minimum, which is crucial for space missions where efficiency is paramount. These panels frequently incorporate advanced high-efficiency solar cells, such as multi-junction cells or gallium arsenide cells, both of which are known for their ability to convert a significant fraction of sunlight into electrical energy. The total power generated by a satellite's solar array can vary considerably based on a variety of factors, including the physical size of the satellite and the specific efficiency ratings of the solar panels employed. According to findings presented in [48], even a solar array that is one-quarter the size of the panels considered in this study can generate over 10 kW of power. Additionally, as the demand for solar arrays continues to increase, modern satellite systems are pushing the boundaries of power generation, with some arrays now delivering up to 50 kW.

Table 3.3. Power Transfer Link Budget: Large Satellite to CubeSat Scenario [36]

$Frequency\ [GHz]$	$P_T\ [dBW]$	$G_T\ [dB]$	$G_R\ [dB]$	$P_R\ [dBW]$	$d_s\ [km]$
1.2	45	35.3	11.6	0	0.78
1.8		39.5	18.3		1.83
2.4		42.2	19.3		2.10

For the purposes of this study, a transmitted power of 30 kW (equivalent to 45 dBW) has been deemed a practical and reasonable figure, making it suitable for our WPT application. Table 3.3 provides a detailed link budget, where the goal is to receive a minimum power level of 1 W at the receiving end. Despite the fact that path loss tends to increase at higher frequencies, the use of larger antenna arrays on both the transmitting and receiving satellites compensates for this loss by significantly boosting antenna gains. As a result, even with these path losses, the transmission range is extended, allowing for a CubeSat swarm to be positioned as far as 2 kilometers away from a larger satellite and still receive sufficient power.

Another key factor influencing the efficiency of the power transfer link is the interaction time between the two types of satellites. Given their differing relative speeds, the interaction window is limited, and this timeframe is closely tied to the design of the satellite constellation. Consequently, the success of the power transfer process hinges on the precise coordination of these interaction times, further emphasizing the importance of thoughtful constellation design in ensuring that sufficient power is transferred during the available interaction period.

3.5.2 Inter-CubeSat Power Transfer within Swarm Networks

In this section, the feasibility of WPT between CubeSats is explored, specifically focusing on the scenario where one CubeSat with excess energy transmits power to another CubeSat in need. Given the limited size of CubeSats, their solar power generation capacity is naturally constrained, which directly impacts the maximum transmission power they can provide. Unlike larger satellites, which have the benefit of greater surface area for solar panels, CubeSats must operate within their smaller power budgets. However, this limitation can be mitigated through cooperative efforts among multiple nanosatellites. By coordinating their actions, a scenario can be envisioned where several CubeSats act as power transmitters, pooling their energy to transfer it to a single CubeSat that requires additional power.

This collective energy-sharing model opens the possibility for a distributed power transfer network within a swarm of CubeSats. The idea is not to rely on a single CubeSat transmitting large amounts of power, but rather on multiple CubeSats contributing

smaller amounts of energy. In this cooperative scenario, the transmission power levels are understandably lower compared to what a large satellite could achieve. Therefore, the received power target is also adjusted accordingly. Unlike the previous scenario involving larger satellites, where a receiving power level of 1 W was acceptable, in this case, a more modest received power level of 100 mW is deemed sufficient to support the energy needs of the recipient CubeSat.

Additionally, in this context, it is worth considering the solar panel capabilities of CubeSats. Referring to previous findings, it is noted that a CubeSat's solar panels are designed to generate approximately 96 W of power under optimal conditions when the satellite is first deployed and fully operational. For the purposes of this analysis, a relatively optimistic transmission power level of 100 W (equivalent to 20 dBW) is assumed, taking into account the potential for efficient energy sharing within the CubeSat swarm. Although CubeSats individually have limited power generation and transmission capabilities, this value represents a plausible upper limit for a coordinated WPT scenario among nanosatellites. Furthermore, the nature of the swarm formation, where CubeSats are arranged in a coordinated and stable flying formation, ensures that there is consistent interaction between all members of the swarm. This configuration facilitates a more reliable power transfer system, as the proximity and alignment of the CubeSats enable more effective energy exchange.

In this scenario, the details of the calculated distances required for effective power transfer between CubeSats are summarized in Table 3.4. The calculations are based on the revised power requirements, which account for the unique limitations associated with CubeSat operations. Notably, the transmitting and receiving antenna gains are assumed to be equal in this case, as both the transmitter and receiver are CubeSats. This equalization is crucial given the constraints on size and power generation capabilities inherent to CubeSats, which generally yield lower overall power output compared to larger satellites.

Due to these limitations, the maximum applicable distance for successful power transfer may fall short of initial expectations. However, a cooperative functioning model presents a solution to enhance the performance of the power transfer process. By allowing a single CubeSat to receive power from multiple transmitting CubeSats simultaneously, the total received power can be significantly augmented. This

Table 3.4. Power Transfer Link Budget: CubeSat to CubeSat Scenario [36]

$Frequency\ [GHz]$	$P_T\ [dBW]$	$G_T\ [dB]$	$G_R\ [dB]$	$P_R\ [dBW]$	$d_c\ [m]$
1.2	20	11.6	11.6	-10	9.1
1.8		18.3	18.3		28.4
2.4		19.3	19.3		26.8

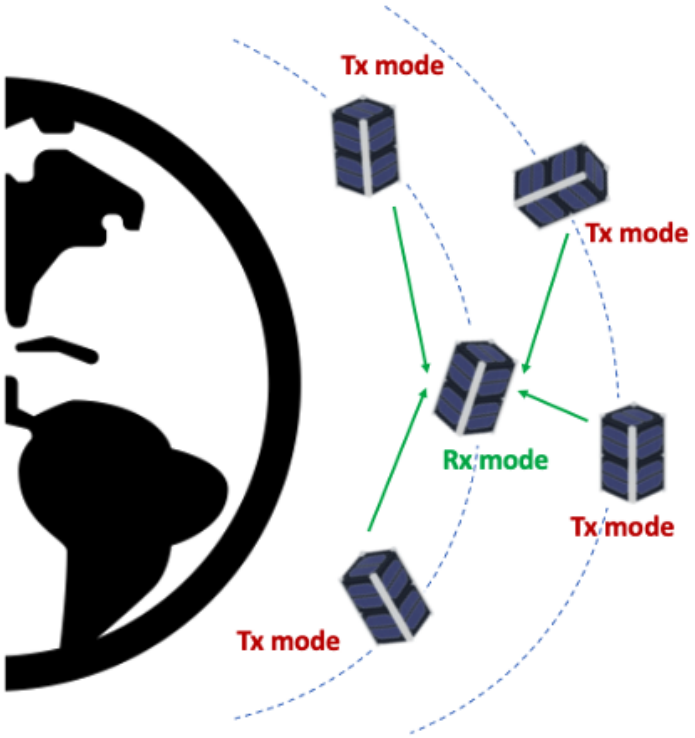

Fig. 3.7. Illustration of collaborative CubeSat WPT, where multiple CubeSats coordinate to transmit energy to a single receiving CubeSat.

collaborative approach not only increases the effective power at the receiving CubeSat but also extends the possible operational distances for the power transfer. Through this strategic coordination, CubeSats can overcome their individual power generation constraints, enabling more efficient and reliable energy sharing within the swarm formation.

In this scenario of cooperative WPT between CubeSats, the concept of distributed power transmission plays a critical role in enhancing overall system efficiency. Specifically, when multiple CubeSats coordinate to transfer energy to a single receiver CubeSat, the collective power transmitted by each CubeSat can significantly improve the performance of the receiving antenna. For example, consider a scenario where two receiving antennas are employed to harvest energy from four transmitting CubeSats. This setup increases the total number of WPT links to four, effectively spreading the load across multiple paths and ensuring more consistent energy transmission to the receiving CubeSat. Furthermore, it is assumed that the CubeSats are equipped with a synchronized communication system that enables coordinated power transmission. This synchronization ensures coherent power transfer, allowing the transmitted signals to align in phase at the receiving end, thereby preventing destructive interference and maximizing the efficiency of energy transfer.

This cooperative functioning not only diversifies the power sources but also directly

Table 3.5. Power Transfer Link Budget: Cooperative CubeSat Scenario

$Frequency\ [GHz]$	$P_T\ [dBW]$	$G_T\ [dB]$	$G_R\ [dB]$	$P_R\ [dBW]$	$d_c\ [m]$
1.2	20	11.6	11.6	-16	18.1
1.8		18.3	18.3		56.6
2.4		19.3	19.3		53.4

impacts the receiver sensitivity. In the case described, the receiver sensitivity is improved from -10 dBW to -16 dBW due to the cumulative contributions from the multiple CubeSats. Such an improvement in sensitivity ensures that even with relatively lower transmitted power from each individual CubeSat, the total received power at the receiver meets operational thresholds. Consequently, the distance over which efficient power transfer can occur is also enhanced. For instance, as depicted in Fig. 3.7, this collaborative approach allows for greater flexibility in CubeSat positioning within a swarm formation, with distances exceeding 50 meters for two of the operating frequencies, as indicated in Table 3.5.

The advantages of cooperative CubeSat powering are particularly pronounced in swarm formations, where multiple CubeSats can dynamically allocate resources depending on power demand and supply conditions. By leveraging the aggregated power from multiple transmitters, the system ensures that the receiver CubeSat can maintain operational functionality over extended distances, even in scenarios where solar power generation may be limited or unevenly distributed across the constellation. This collaborative strategy, therefore, not only extends the operational range but also enhances the resilience and efficiency of the WPT system, making it a promising approach for next-generation nanosatellite missions.

3.6 Challenges and Future Outlook

Satellites often perform various types of close-proximity maneuvers that require precise control to bring two or more satellites near each other while maintaining a safe operational distance. These controlled approaches can serve various purposes, such as satellite servicing or collaborative tasks, and their duration is influenced by several key factors including the satellites' relative velocities, orbital configurations, and specific mission objectives. The interaction time during these close encounters can vary significantly depending on mission requirements. In the context of collaborative power transfer between satellites, the timing and positioning are highly flexible, allowing the interaction to be tailored to the needs of the mission. For example, in swarm missions where one satellite is tasked with supplying power to another, the duration of close approaches may extend from several hours to even days, depending on the operational

workload of the swarm. However, careful planning and coordination are essential to ensure mission success, as these maneuvers require accurate orbital calculations and real-time control to maintain both safety and efficiency throughout the process.

Another significant challenge lies in the regulatory framework governing satellite transmissions. Satellite communications must comply with national and international regulations, particularly regarding frequency allocation and transmission power limits. Securing the necessary frequency bands, minimizing interference with other satellite systems, and adhering to strict power regulations are complex issues that satellite operators must navigate. Moreover, current regulations surrounding WPT for in-space applications are not fully developed, adding further uncertainty to mission planning and design.

In addition to regulatory challenges, small satellites such as CubeSats are inherently constrained by their limited size, which directly impacts their power generation capacity. Designing efficient power systems that maximize the available energy from solar panels and optimizing transmission techniques to reduce power consumption are critical to ensure that WPT systems are viable for small satellites. Using low-power components, improving energy harvesting technologies, and developing innovative methods for power management become essential to overcoming these limitations. As space missions increasingly rely on small satellites to perform complex tasks, these challenges must be addressed to achieve reliable and sustainable communication and power transfer within the constraints imposed by the satellite's physical dimensions.

3.7 Conclusion of the Chapter

This section of the thesis examines the feasibility of in-space WPT systems for nanosatellites, with a particular emphasis on the integration of transparent antennas with solar panels. By leveraging the same spatial resources for both power generation and transmission, WPT presents a promising solution for efficient energy transfer within satellite systems. Two scenarios were investigated: power transfer from larger satellites to CubeSats and cooperative power sharing within a swarm of CubeSats. Simulations of various antenna array configurations, panel sizes, and operating frequencies indicated that effective power transfer from larger satellites over distances of several kilometers is achievable, thereby supporting future satellite servicing missions. However, cooperative power transfer between CubeSats is constrained to tens of meters due to their smaller dimensions and reduced power generation capabilities. Despite these limitations, coordinated power sharing within a swarm is deemed viable for short-range applications.

The integration of transparent antennas into solar panels exhibits significant potential for enhancing satellite power systems. While challenges such as optimizing

antenna design and addressing regulatory considerations persist, this research underscores the increasing viability of inter-satellite WPT. It is anticipated that future technological advancements will further enhance the efficiency and applicability of these systems, rendering them valuable assets for satellite missions aimed at achieving energy autonomy and extending operational lifetimes. Having discussed and investigated the feasibility of in-space WPT among small satellites within this work and section, it is recognized that improvements in performance and usability of the concept are essential, which has been precisely addressed in the subsequent stages of this research.

4 Optimization of Meshed Antenna Arrays for Photovoltaic Integration

This chapter is based on the following article:

[16] A. B. Gok, D. Masotti, and A. Costanzo, "Co-location of pv panel with meshed antenna array for inter-satellite energy transmission," *IEEE Journal of Radio Frequency Identification*, vol. 8, pp. 516–525, 2024.

4.1 Introduction to the Chapter

In this chapter of the thesis, a more detailed investigation into a higher number of antenna array configurations is conducted, alongside several geometrical improvements. The prototypes for two frequency bands have been successfully realized, and further insights into the impact of the solar panel's presence on antenna performance are explored.

The design process incorporates a novel strategy by eliminating horizontal conductive strips in the antenna's meshed metallization. This adjustment is critical for enhancing the transparency of the antenna without sacrificing its performance, thus maintaining optimal solar power production capabilities. The chapter discusses the engineering challenges and design choices made for two distinct antenna arrays operating at frequencies of 2.45 GHz and 5.8 GHz. These frequencies are selected for their suitability in WPT applications, enabling efficient energy transmission between satellites while minimizing interference.

The fabrication of the antenna arrays employs low-cost additive manufacturing techniques on borosilicate glass substrates measuring 110×110 mm^2. The choice of vertical strips with a line spacing of 0.04λ emerges as the optimal compromise, ensuring maximal transparency and performance of the antenna while preserving the underlying PV panel's functionality.

A critical aspect of this study is the presence of front conductive lines in solar panels, commonly referred to as "fingers" and "busbars". These lines serve the essential purpose of collecting and conducting the generated electrical current, but their spacing constitutes a significant parameter that greatly influences the overall performance of the system. This influence is particularly pronounced at higher frequencies, where the antenna's radiation characteristics can be adversely affected by the conductive elements' arrangement. Therefore, careful consideration of these factors is essential in the design and optimization of the integrated system.

Through rigorous simulations and experimental validations, this study uncovers the significant influence of the PV metallization patterns on the radiation properties of the

antennas, particularly at the higher frequency of 5.8 GHz. Notably, discrepancies in antenna gain compared to theoretical predictions underscore the importance of considering the interaction between the antenna and the PV panel's metallization layout. By employing a reverse-engineering approach, the effective electromagnetic characteristics of the glass substrate are modeled, highlighting the necessity for a co-design strategy that aligns the PV panel and antenna systems. This approach not only enhances the accuracy of full-wave simulations but also facilitates a comprehensive understanding of the overall system's radiating characteristics.

In summary, this chapter aims to provide insights into the innovative integration of transparent antennas with PV technology, addressing the challenges of power autonomy in small satellite missions while setting the stage for future developments in in-space WPT applications. The exploration of this integrated design approach lays the groundwork for optimizing the performance and efficiency of energy transfer systems in satellite constellations, paving the way for advancements in deep space exploration and satellite coordination.

4.2 Photovoltaic Cell Simulation Framework

A solar cell, commonly referred to as a PV cell, typically consists of silicon-based materials coupled with protective glass. This glass functions as a transparent barrier, safeguarding the solar cell against physical damage, moisture, dust, and other contaminants. The components incorporated into our simulation framework include the back contact, silicon layer, protective glass (with a relative permittivity ϵ_r of 6), and the borosilicate glass substrate that supports the printed antenna structure. Given the variability in configurations dictated by the selected solar panel, along with the absence of comprehensive specifications for some low-cost commercially available options, approximations regarding the stack layout become a necessary consideration.

The back contact of a solar cell is a crucial element utilized as the ground plane for our antenna, a role its efficacy has been demonstrated in the prior research study [17]. This component functions as the negative terminal and is strategically positioned on the side of the cell that faces away from incident sunlight, making direct contact with the substrate. By exploiting this dual-purpose layer, we not only facilitate the efficient collection and transport of electrons generated within the semiconductor layers but also minimize energy losses. The back contact is essential in preventing the recombination of electrons and holes in the semiconductor, thereby enhancing the overall performance and effectiveness of the solar cell.

To achieve a deeper understanding and yield more precise outcomes in our simulations, it is imperative to provide a detailed specification of the employed simulation model. Importantly, the model incorporates not only the back conductor

layer but also includes the metallization atop the silicon layer, comprising busbars and fingers. The busbars play a vital role in conducting the direct current generated by the solar PV cell, while the metallic, narrower grid fingers—referred to as solar cell fingers—are oriented perpendicularly to the busbars and are responsible for collecting the generated current, which is then transferred to the busbars. Fig. 4.1 illustrates the configuration of this metal layer in conjunction with the other components that constitute a typical PV cell stack.

The application of these contacts, encompassing both busbars and fingers, is executed using a technological process known as screen printing on the surface of the PV cell. Notably, the design and optimization of these metallization components can be customized based on considerations of cost, quality, and performance [49]. A primary challenge in the design of these top contacts lies in achieving an optimal balance between the increased resistance losses associated with widely spaced grids and the augmented reflection caused by a high proportion of metal coverage on the surface.

Determining the number of top contact lines—whether categorized as busbars or fingers—along with their specific positions, arrangements, line widths, and uniformity across the entire PV module surface presents a complex challenge. As a result, developing a universally applicable model for this work is particularly difficult. These considerations have guided our decision to adopt a simulation model that simplifies the stack-up of PV cells while retaining a general-purpose approach applicable to various types of PV panels, as discussed in the next sections.

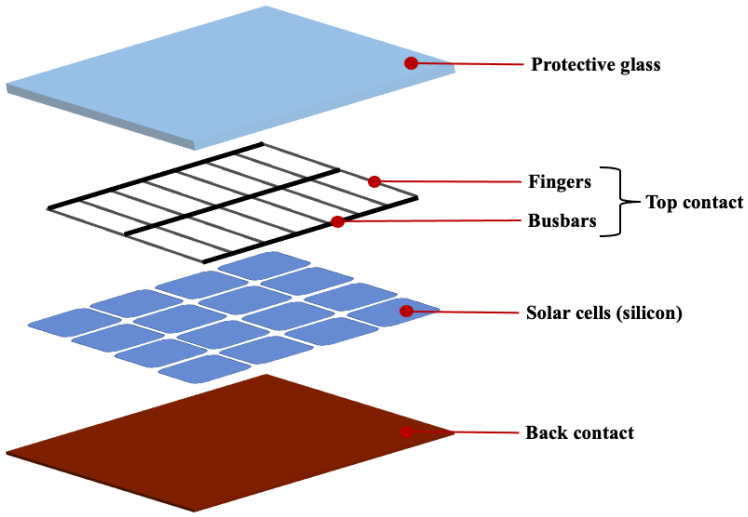

Fig. 4.1. Schematic overview of a standard solar module structure featuring top contact elements [16].

4.3 Impact of Horizontal Line Removal

Building on our previous work with printed mesh antenna structures, we now focus on enhancing the transparency of the antenna while preserving its optimal performance. This approach involves the strategic removal of horizontal lines from the mesh design, based on the understanding that current primarily flows along the vertical lines of the antenna. The expectation is that this modification will have minimal impact on the antenna's performance while significantly increasing its transparency.

Fig 4.2a and 4.2b illustrate both design configurations, which are engineered for operation at 2.45 GHz, allowing for a comparative performance analysis. In Fig 4.3, surface current simulation results for both designs are presented, employing a consistent

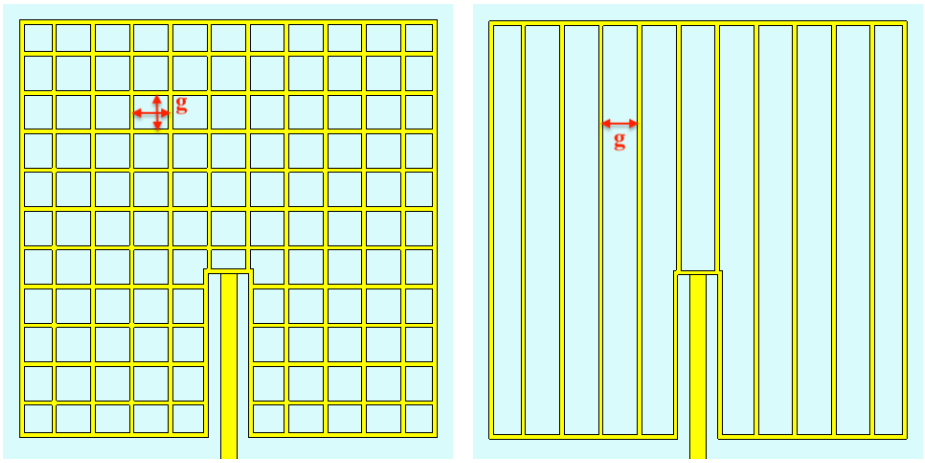

Fig. 4.2. Patch antenna element designs: (a) default meshed configuration; (b) modified transparent design with vertical lines only [16].

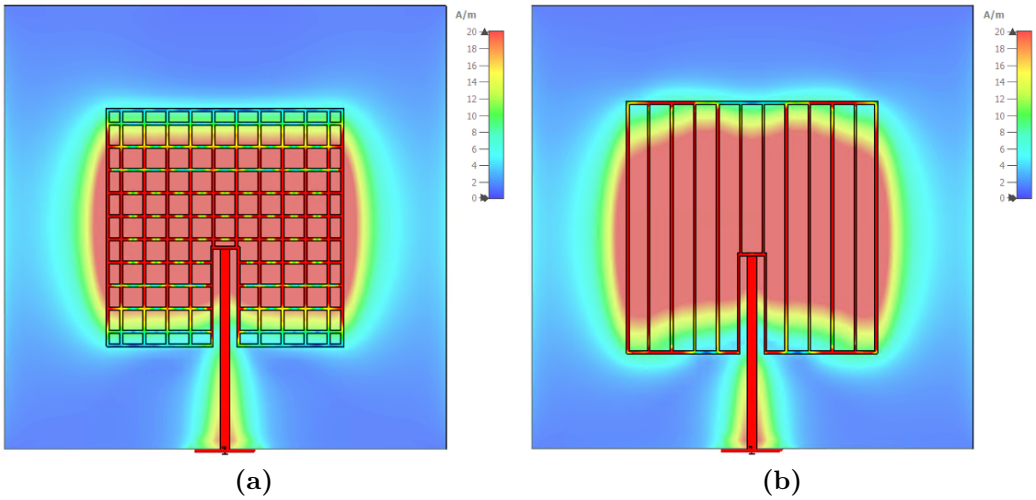

Fig. 4.3. Surface current simulations at 2.45 GHz for (a) the meshed antenna design and (b) the vertical line design [16].

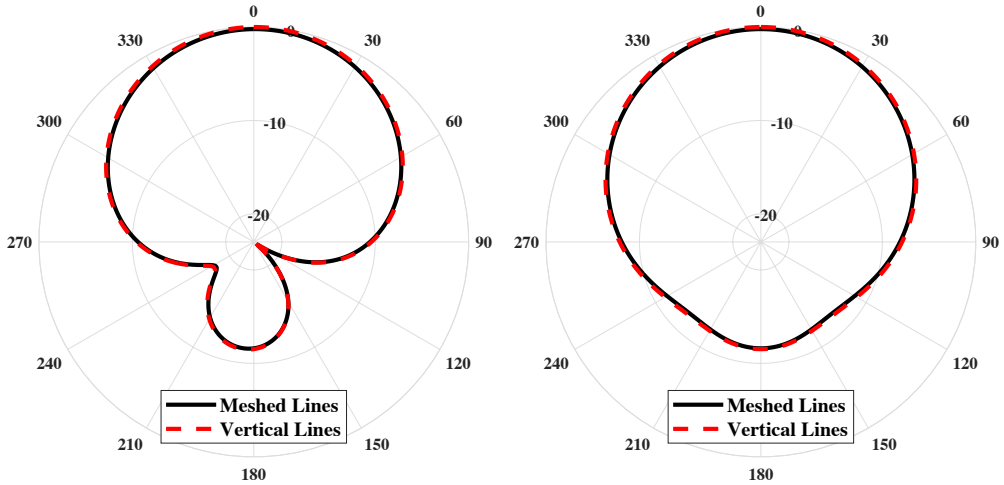

Fig. 4.4. Normalized simulated radiation patterns at 2.45 GHz for the meshed and vertical line antennas: (a) E-plane, (b) H-plane [16].

scale for clarity. While there is a slight difference in the shape of the surface current distribution, the radiation patterns for both the meshed and vertical line designs are remarkably similar, as shown in Fig 4.4 at the designated frequency.

However, Fig. 4.5 reveals the reflection coefficient graphs for both configurations, indicating the emergence of new resonances in the vertical line design. These resonances are likely attributed to distributed reactive coupling along the vertical lines. In contrast, the meshed configuration avoids this issue due to the shorting effect

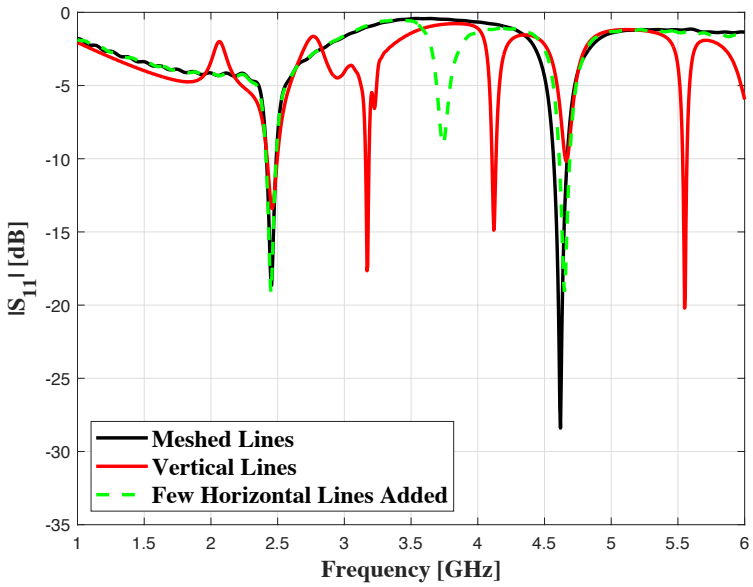

Fig. 4.5. Simulated input S-parameters for the antenna element with various conductive line configurations [16].

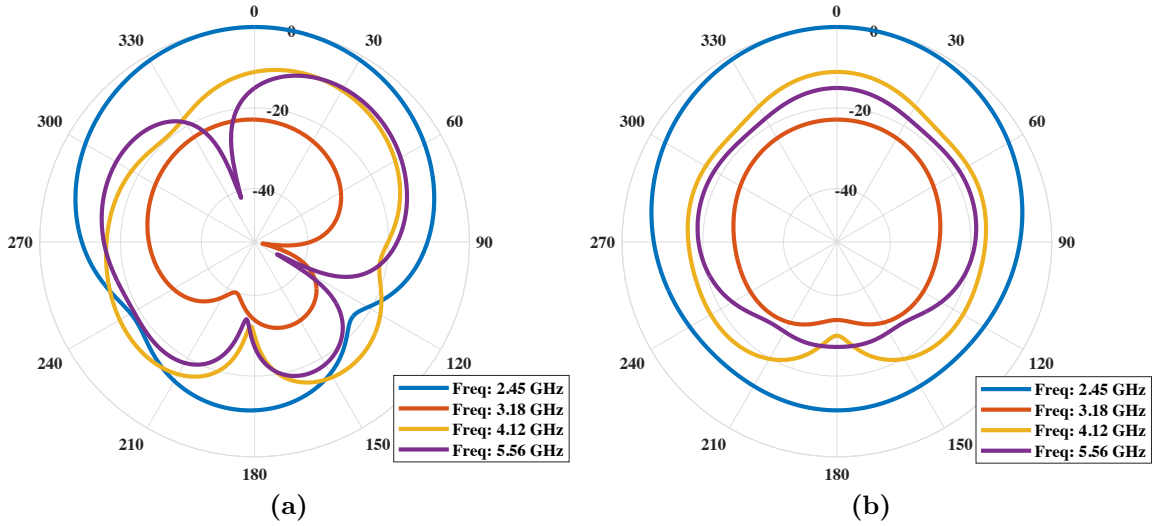

Fig. 4.6. Comparison of normalized simulated radiation patterns at new resonant frequencies relative to 2.45 GHz for the antenna with vertical lines: (a) E-plane, (b) H-plane [16].

provided by the horizontal lines. When the radiation patterns at the newly identified resonant frequencies, shown in Fig. 4.6, are compared to the reference frequency of 2.45 GHz, no effective radiation is observed.

To further validate our findings, we also analyzed an antenna featuring only three horizontal lines. The predicted reflection coefficient for this design is also presented in Fig. 4.5, confirming that the resonances can be mitigated through periodic shorting of the vertical lines, thereby suppressing parasitic resonances. Consequently, the design utilizing only vertical lines is favored, as it reduces the amount of conductive ink used by 37.7%. This design change leads to an increase in transparency, calculated based on the applied metallization, improving from 91.6% to 94.4% for the antenna elements designed on a 50 x 50 mm^2 substrate during simulations.

A detailed examination of the antenna gains reveals a subtle increase from 4.4 dBi in the meshed design to 4.6 dBi in the vertical line configuration, which is a significant finding in this study. Consequently, it is recommended that future research focuses specifically on the vertical line configuration within array antenna setups, as it presents a promising direction for further investigation.

To achieve this goal, we performed antenna array simulations for both the 2.45 GHz and 5.8 GHz frequency bands. These simulations were tailored to be compatible with the capabilities of the specified printer and were designed to fit the available Borofloat® 33 glass samples. Similar to the previous prototypes, the glass samples measured 110 x 110 mm^2, with a thickness of 1.75 mm. In addition, the thin PV panel situated beneath the glass was integrated into the array structure and modeled as a homogeneous layer, representing the EM properties of silicon. For each frequency, three

designs were simulated, varying the spacing between the printed vertical lines, with the spacing values consistently set at 0.02λ, 0.03λ, and 0.04λ, in terms of wavelength, for both frequencies. Across all designs, the line thickness was kept constant at 0.3 mm, adhering to the limitations of the printer's resolution.

At the outset, all six antenna element designs were thoroughly analyzed, and simulations of antenna arrays incorporating a corporate feeding network were conducted using CST to evaluate their performance. For the 2.45 GHz configuration, it was determined that a maximum of four antenna elements could be positioned within the spatial limits of the available glass samples. In contrast, at the higher frequency of 5.8 GHz, a denser configuration accommodating up to 16 elements was achievable within the same glass dimensions. The spacing between antenna elements was carefully optimized based on wavelength considerations, ensuring that as many elements as possible were incorporated without introducing excessive mutual coupling or interference between them, which could degrade performance.

Throughout the simulation process, key performance metrics such as radiation efficiency and array antenna gain were extracted and analyzed. This data provided valuable insights into the functional characteristics of the arrays at both frequency bands. Moreover, the transparency of the patch elements on the array, referred to as T_{patch}, was computed using (4). This transparency value was derived by subtracting the total area occupied by the conductive material from the overall transparency of the glass substrate, taking into account the full surface area of the borosilicate glass sample. Notably, the transparency calculation deliberately excluded the feeding network from consideration, since the layout and design of the feeding network tend to vary substantially across different frequencies. This is especially true for array designs, where the number of radiating elements and their arrangement directly impact the network's configuration. Consequently, the primary goal of the transparency calculation at this stage was to provide an initial estimate of the transparency of the antenna patches themselves, offering an early evaluation of how transparent the design might be before finalizing and refining the complete array structure. This approach ensures that the design process remains flexible, allowing for further adjustments to improve transparency or performance as necessary before moving to the next design phase. It is also important to highlight that this transparency equation accounts for the entire surface area of the substrate. As a result, readers should carefully reference earlier equations and take note of the differences when comparing transparency values discussed in previous chapters. This distinction is crucial for ensuring an accurate comparison, as earlier sections may have focused on more localized aspects of transparency, while this equation provides a broader assessment based on the full substrate area.

Table 4.1. Simulated Performance of Antenna Array at 2.45 GHz [16]

g [mm]	1.15 (0.02λ)	1.7 (0.03λ)	2.3 (0.04λ)
Radiation Efficiency [%]	72.5	72.2	68.2
$\boldsymbol{T_{patch}}$ ***[%]***	93.9	95.6	96.4
Array Gain [dBi]	8.7	8.5	8.3

Table 4.2. Simulated Performance of Antenna Array at 5.8 GHz [16]

g [mm]	0.5 (0.02λ)	0.7 (0.03λ)	0.95 (0.04λ)
Radiation Efficiency [%]	68.4	68.1	67.8
$\boldsymbol{T_{patch}}$ ***[%]***	93.2	94.4	95.3
Array Gain [dBi]	13.4	13.3	13.2

$$T_{patch} = 1 - \frac{[\lceil \frac{W}{g+w_l} \rceil + 2] \times L \times w_l \times N_e}{Total\ Area} \tag{4}$$

In this context, W refers to the width of the antenna element, g represents the spacing between the lines, w_l indicates the line width, L denotes the length of the antenna element, and N_e corresponds to the number of elements used in the antenna array. Additionally, Tables 4.1 and 4.2 provide the simulated performance metrics for the antenna arrays operating at 2.45 GHz and 5.8 GHz, respectively. The inter-line spacing, g, is presented in millimeters along with its relative proportion to the wavelength at each frequency. Transparency values have been converted to percentages, and the antenna gain is expressed in decibels. The simulation results for the antenna arrays reveal a slight reduction in both radiation efficiency and array antenna gain. However, this is counterbalanced by an increase in the overall transparency of the antenna. It is important to emphasize that this improvement in transparency is also associated with a decrease in the amount of ink used during printing, which in turn leads to a reduction in material costs.

In the following chapter, a more in-depth exploration of the design aspects for each frequency will be presented, along with a detailed discussion of the corresponding prototypes.

4.4 Development of a 2.45 GHz Solar Antenna Array

Based on the results obtained from the simulations, a decision has been made to fabricate the antenna system for operation at 2.45 GHz, opting for the widest inter-line spacing (g) of 2.3 mm to enhance the transparency of the patch, denoted as T_{patch}. Although this choice results in a slight compromise in the antenna's radiation

performance compared to alternative designs functioning at the same frequency, the primary objective remains focused on preserving the operational efficacy of the PV panels. As previously stated in Chapter 2 that an increase in transparency correlates with improved solar power output, thereby justifying this approach.

To thoroughly assess the integration of the PV panel, two distinct prototypes were developed following the inkjet printing of the antenna array on the glass substrate. For the purposes of comparison, one prototype utilized a conventional copper layer as the ground plane, while the other incorporated the solar panel itself; both prototypes are illustrated in the photographs provided in Fig. 4.7. The antenna array is configured

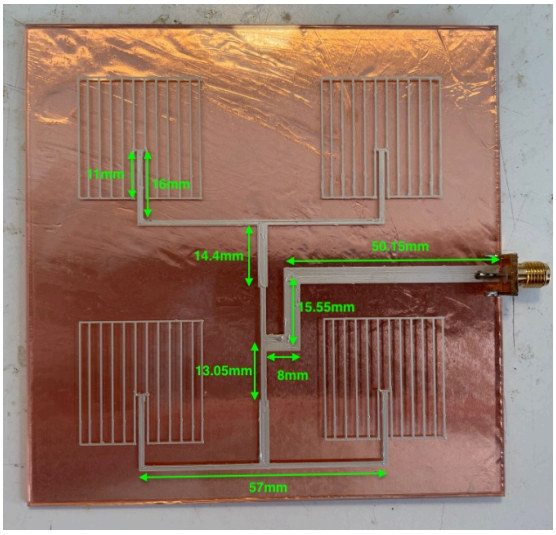

(a)

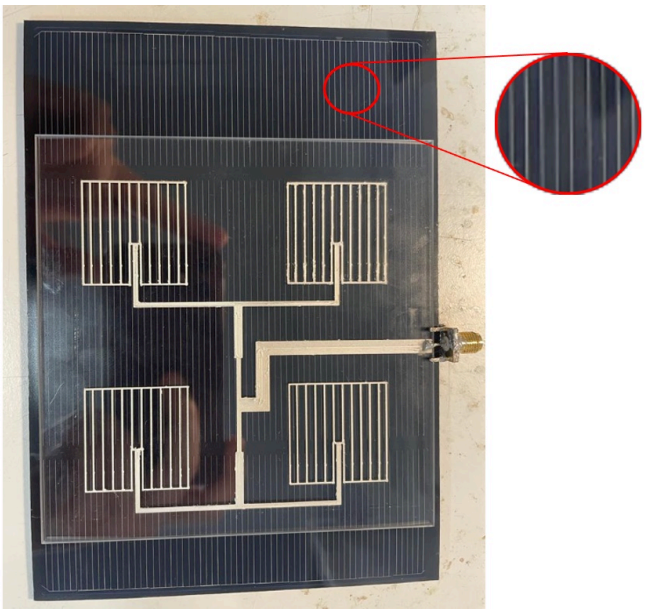

(b)

Fig. 4.7. Images of the 4-element prototype at 2.45 GHz: (a) excluding the solar panel; (b) including the solar panel [16].

with four square patch elements, each measuring 28.4 mm x 28.4 mm, and is inset fed through 100 Ω microstrip lines. These lines converge into a single feed path via a quarter-wave transformer designed for impedance matching. Additionally, the main 50 Ω feeding line is meandered to position it strategically between the two 100 Ω branches, with the meandering pattern refined through iterative simulations to ensure optimal performance.

In Fig. 4.7a, critical dimensions that elucidate the previously discussed design parameters are meticulously detailed, offering significant insights into the intricacies of the design process. Remarkably, the transparency of the printed prototype has been recorded at 91.7%, a value that accounts for the filling of the feeding network in the assessment.

The plots of the simulated and measured input reflection coefficients for both configurations are illustrated in Fig. 4.8. The results are indicated to show a satisfactory agreement near the targeted frequency of 2.45 GHz for both cases. However, a slight shift in frequency towards 2.5 GHz is noted in the presence of the solar panel, along with the appearance of additional resonances when the PV panel is included. These variations may be attributed to the simplified representation of the stack-up employed in the EM simulation. Additionally, it is suggested that the presence of top contacts, including front fingers and busbars as depicted in Fig. 4.7b, could also affect the observed discrepancies. The enlarged metal strips shown in the figure may introduce further complexities into the electromagnetic propagation, potentially leading to effects that are not sufficiently captured by the simplified simulation models of the PV panel. This is particularly noticeable at higher frequencies, as evidenced in Fig. 4.8b.

To evaluate the array antenna gains of the two prototypes presented in Fig. 4.7, an experimental setup was employed, as depicted in Fig. 4.9. This configuration included

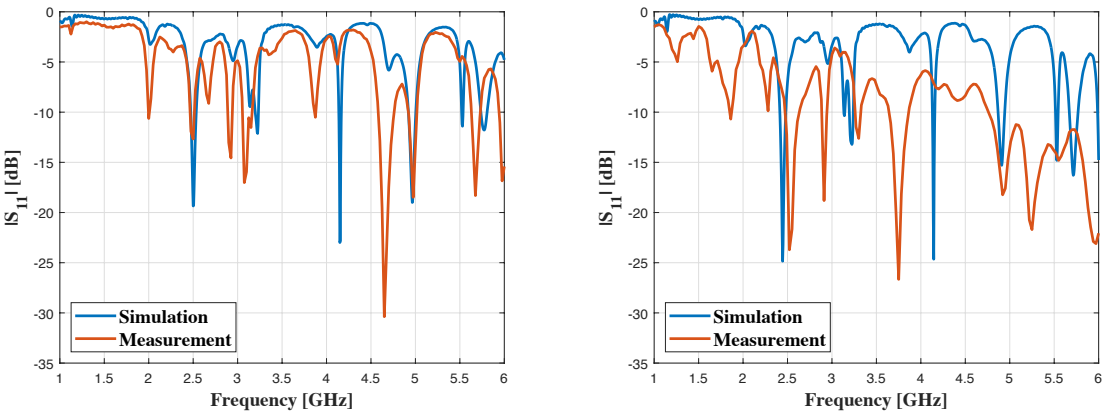

Fig. 4.8. Simulated and measured reflection coefficients of the antenna array operating at 2.45 GHz: (a) without the solar panel; (b) with the solar panel [16].

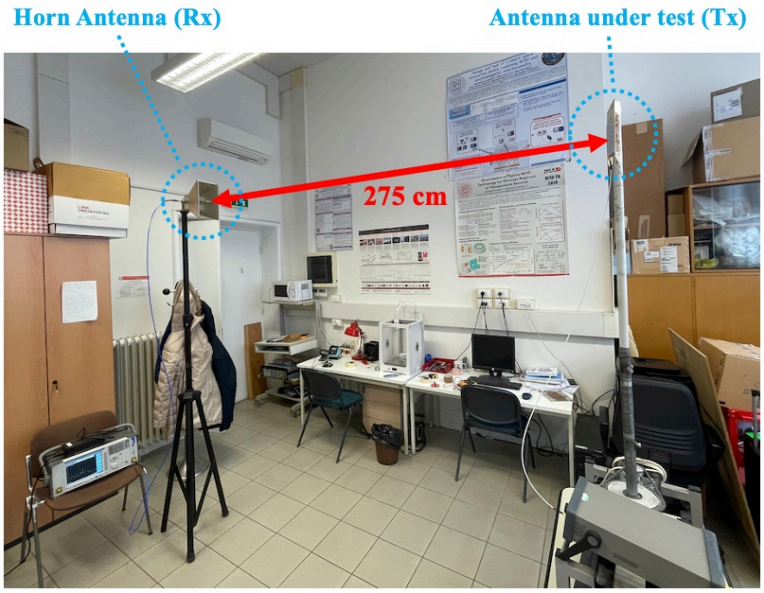

Fig. 4.9. Experimental setup for evaluating antenna array performance in the laboratory [16].

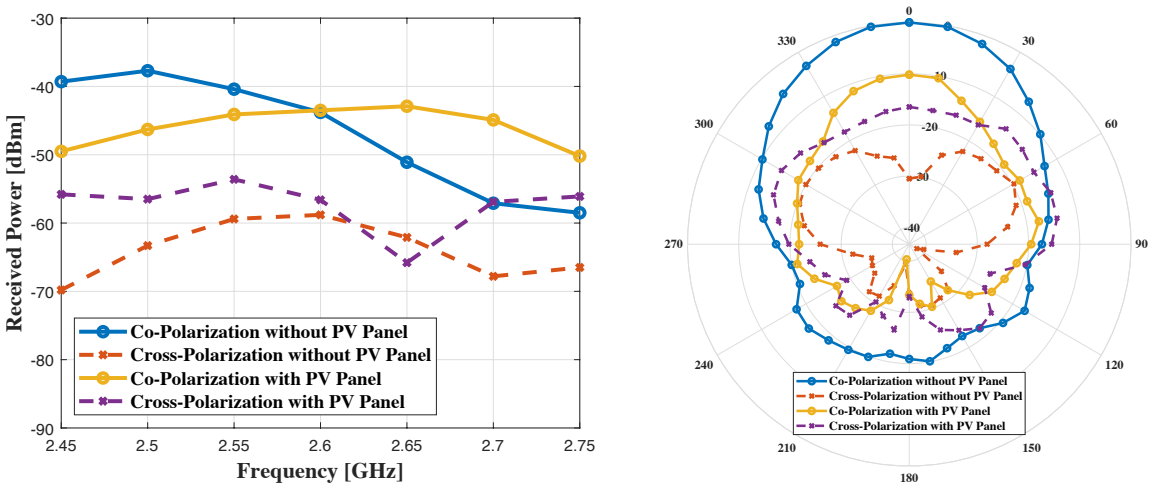

Fig. 4.10. Measurements of co- and cross-polarization for the 4-element antenna array: (a) received power levels for -2.3 dBm transmitted power; (b) normalized radiation patterns at 2.45 GHz, with and without the PV panel [16].

a horn antenna connected to a spectrum analyzer, which was utilized to measure the received power spectra for both co- and cross-polarization emitted by the proposed system. The system was excited by a signal generator placed 275 cm away. It is crucial to note that for the prototype shown in Fig. 4.7b, proper alignment between the metal lines of the patch antenna and the top conductive lines of the PV panel is vital, as a 90°-rotation was found to adversely affect radiation performance.

The data illustrated in Fig. 4.10a displays the received power levels from the two prototypes referenced earlier, as detailed in Fig. 4.7. Both co- and cross-polarization

results are included to confirm the linear polarization characteristics of the array system. The measurements were performed across a frequency range to accommodate the slight detuning noted in Fig. 4.8b, which is likely caused by inconsistencies in the printing process. Furthermore, Fig. 4.10b showcases the measured radiation patterns for both co- and cross-polarization at 2.45 GHz, emphasizing how the solar cell substrate influences antenna performance. The figure indicates that incorporating the PV panel negatively impacts broadside radiation, resulting in increased cross-polarization and a decrease in co-polarization levels.

Upon closer examination of the received power levels in Fig. 4.10a, it becomes clear that the inclusion of the solar panel significantly affects the operating frequency of the antenna array. Specifically, the maximum received power is achieved at 2.5 GHz in the absence of the solar panel, while the introduction of the solar panel shifts the frequency to 2.65 GHz. This shift highlights the influence of the simplified solar panel model used in the EM simulation, which does not fully capture the complexity of the real-world effects of the panel on antenna performance. As demonstrated in Fig. 4.10a, the peak received power in co-polarization, which directly correlates with the maximum antenna gain, is recorded at 2.5 GHz, achieving a value of 7.1 dBi. This result aligns well with the simulated gain of 8.3 dBi when no solar panel is present. However, with the integration of the PV panel, the highest gain is observed at 2.65 GHz, where it drops to 2.9 dBi—a significant reduction from the 8.3 dBi gain without the panel. The gain values obtained from these measurements account for several factors, including free space path loss, mismatch loss, cable attenuation, and the horn antenna's gain.

Having explored the 2.45 GHz antenna array and its integration with the solar panel, the focus now shifts to the design at 5.8 GHz. This next chapter examines the specific challenges and optimizations required for higher frequency operation, addressing the key design parameters, performance outcomes, and potential improvements over the 2.45 GHz configuration.

4.5 Development of a 5.8 GHz Solar Antenna Array

In this part of the chapter, a design operating at 5.8 GHz is explored to assess performance at higher frequencies, utilizing a line spacing (g) of 0.95 mm, which corresponds to 0.04λ. This configuration accommodates a 16-element array within the dimensions of the glass substrate. To enhance transparency, strategic metallization removals were executed in the broader sections of the feeding network, as demonstrated in Fig. 4.11, with simulation results indicating no significant degradation in performance. The final design achieved a successful reduction of 15% in the solid feeding network, resulting in improved transparency without compromising the efficiency of the antenna system. The printed design, depicted in Fig. 4.11, features a

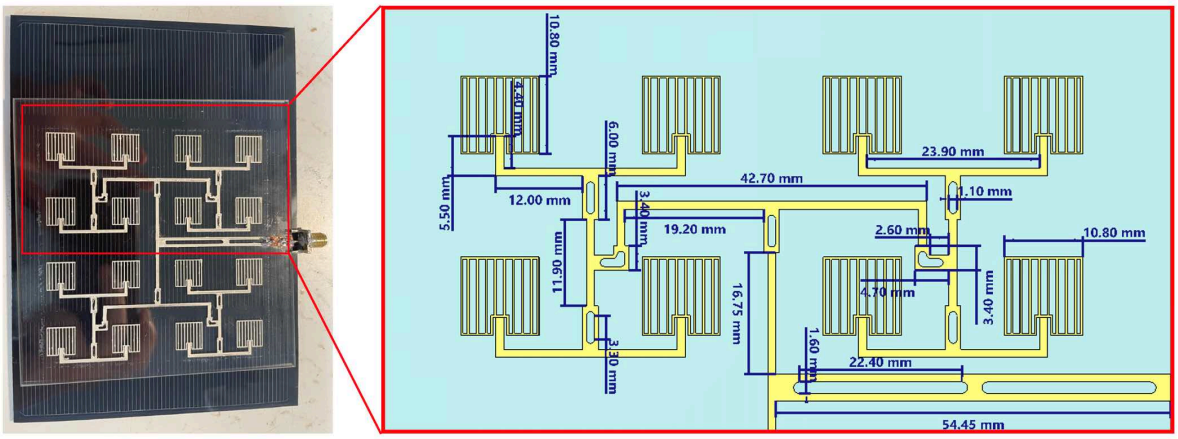

Fig. 4.11. Image of the 5.8 GHz printed prototype installed on a solar panel, highlighting the geometric dimensions of the meshed patch antenna array [16].

configuration of 16 square patch antenna elements, each measuring 10.8 x 10.8 mm^2. Additionally, the feeding network is characterized by 14 small apertures distributed along the quarter-wave transformers and two larger openings located on the 50 Ω microstrip line directly after the connector. Comprehensive geometric dimensions of these holes and other essential parameters are meticulously detailed in Fig. 4.11, accompanied by a call-out depiction. The overall transparency, accounting for both the feeding network and the hollows, achieves an impressive value of 88.9%.

The S-parameter measurements were obtained using a vector network analyzer, and the results are illustrated in Fig 4.12a, which compares simulated and measured data.

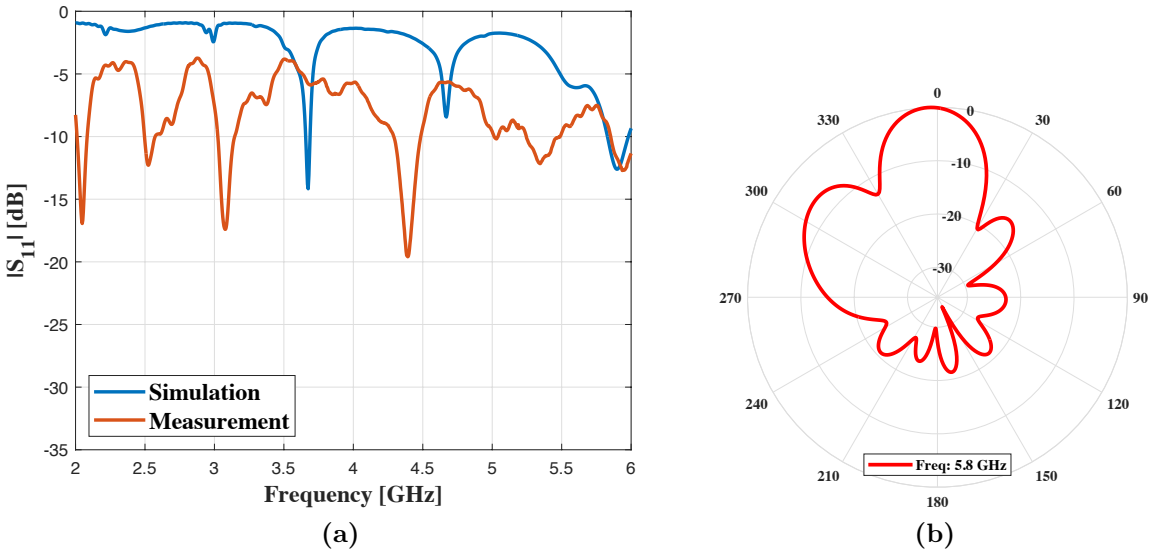

Fig. 4.12. (a) Comparison of simulated and measured input S-parameters for the antenna array at 5.8 GHz with the solar panel [16] and (b) simulated radiation pattern.

The simulated radiation pattern is presented in Fig. 4.12b. A clear alignment between the measurement and simulation is observed at the target frequency of 5.8 GHz; however, discrepancies are noted at other frequencies, akin to observations made in the previous section, potentially stemming from similar underlying factors. At the designated design frequency, the metal line pattern of the PV panel—excluded from the full-wave simulation—significantly affects the antenna's performance, as evidenced by antenna gain measurements taken at a distance of 200 cm. The translation of the antenna patches relative to the PV conductive lines alters the antenna's performance, as evidenced by the significant decline in performance when the metallizations of the PV panel and antenna array are rotated by 90 degrees. This misalignment disrupts the linear polarization characteristics, resulting in a measurable reduction in received power for both co-polarization and cross-polarization. In contrast to the simulation results, cross-polarization measurements show a closer resemblance to co-polarization outcomes. Specifically, the recorded antenna gains are -4.2 dBi for co-polarization and -9.7 dBi for cross-polarization. This finding is corroborated by measurements conducted on the array placed on glass with a standard copper ground plane instead of the PV panel, which yielded a measured gain of 7.5 dBi. Furthermore, co-polarization measurements demonstrate substantially higher values compared to those of cross-polarization.

To provide a comprehensive overview, measurements taken under less than ideal conditions—specifically when the metallizations of the PV panel and the antenna array are rotated by 90 degrees—reveal a significant decline in performance, particularly affecting the linear polarization characteristics of the array. As anticipated, the cross-polarization received power drops from -53.0 dBm when the conductive lines of the PV panel and antenna are misaligned to -55.2 dBm when aligned. Conversely, the received power for co-polarization improves from -63.0 dBm to -60.8 dBm with proper alignment. These observations indicate that the PV panel adversely impacts overall performance at this operational frequency. The periodic arrangement of the PV metal lines could potentially be the source of several resonances in the antenna input impedance. This phenomenon is analogous to the behavior observed in FSS or metamaterials, where periodic structures introduce additional resonant modes as a result of their interaction with electromagnetic waves. However, experimentally testing this theory presents significant challenges, as modification of the solar cells' internal structure is not feasible due to the absence of manufacturing control. To address this, future work could involve reimagining the entire design of the solar cell specifically for this purpose, optimizing the metal lines and their spacing to minimize their impact on antenna performance. Such an approach would enable the verification of whether the periodic structure is indeed the primary cause of the observed resonances and discrepancies. The lack of a precise representation of the conductive lines of the PV

panel in the simulation model markedly affects the results, especially in high-frequency designs. Given the close spacing of approximately 1.6 mm between the metallizations of the PV panel and the antenna elements—optimized as fractions of the wavelength—this issue becomes more pronounced. While the PV panel's metal lines can be effectively modeled as a lossy ground plane at lower frequencies, this assumption becomes insufficient at higher frequencies due to the increasing significance of the silicon layer's thickness relative to the wavelength, which causes interactions between the panel's metal lines and the antenna's metallization pattern. As a result, a more complex modeling approach is essential to accurately capture these interactions.

In conclusion, these findings highlight the importance of accurately modeling the conductive features of PV panels in simulations, particularly for high-frequency applications, to ensure dependable performance predictions for integrated antenna systems. This chapter elucidates the intricate relationship between the PV panel and antenna performance, stressing the need for advanced design methodologies that take real-world conditions into account.

4.6 Assessment of Top Contact Structures in Solar Panel Modeling

As discussed in Section 4.2, solar cells consist of front fingers and busbars that form a metallic pattern atop the silicon substrate, with widths significantly smaller than those of the antenna metallization grids. To develop an EM model for the antenna array that balances accuracy and computational efficiency, the detailed layout of the metal layer has been simplified and represented at a higher level of abstraction. This simplification involves assigning an effective conductivity to one of the layers that hosts the grid metallization of the antenna array, as depicted in Fig. 4.13. However, the results obtained indicate a critical need to include the front contact layer in our simulation models. It is important to note that the stack-up presented in Fig. 4.13 closely resembles that in Fig. 3.2a; however, a key distinction lies in the thickness of the silicon layer, which can vary among different PV cells. In this investigation, we

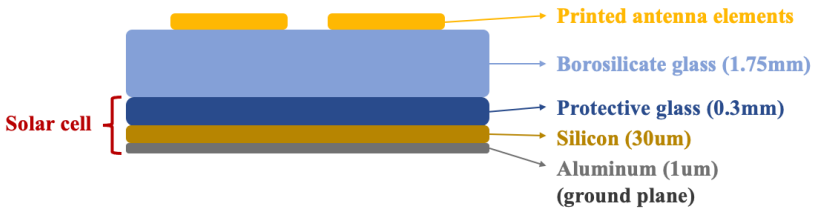

Fig. 4.13. Simplified representation of the multi-layer PV substrate integrated with the grid-printed antenna array [16].

aimed to explore the effects of the silicon layer more comprehensively, thus we have increased its thickness to facilitate a deeper understanding of its influence on performance. The structural attributes and metallic properties of this front layer pose substantial challenges due to their inherent complexities, making it difficult to ensure homogeneity and accurately characterize the metal. Our findings emphasize the considerable impact that the configuration of the top contact layer has on the performance of the antenna, which is contingent upon the design of the metal lines. We argue that the effects of varying frequencies and configurations on antenna performance are influenced by factors such as the thickness, conductivity, and spacing of the top solar lines, necessitating a more detailed representation of the solar panel model to capture these interactions accurately.

The complex design of the front lines poses significant challenges; however, their effects can be integrated into simulations by increasing the conductivity of the protective glass layer. Unlike the approach taken in [50], which emphasizes enhancing the conductivity of the silicon layer, we propose that it is both more effective and appropriate to focus on augmenting the effective conductivity of the cover glass, given its considerably greater thickness relative to the silicon. This strategy facilitates a more comprehensive understanding of the interactions and behaviors of the metal lines within the simulation framework.

To address the identified challenges, the focus is placed on the 2.45 GHz antenna array by enhancing the effective conductivity of the protective glass substrate, which allows for a more precise representation of the metallic front layer. This adjustment is

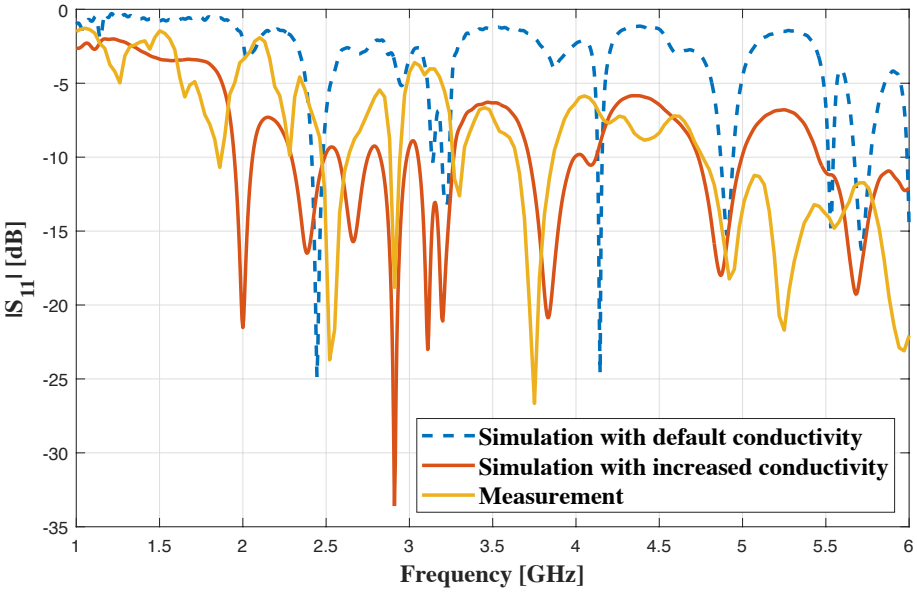

Fig. 4.14. S-parameter comparison of simulation results with enhanced effective conductivity of the protective glass and measured data at 2.45 GHz [16].

deemed essential due to the complexities associated with accurately modeling thin metallic lines using a full-wave approach. By improving the effective conductivity, ambiguities related to the front layer's structure are reduced, thereby enhancing the simulation's ability to effectively represent the behavior of the solar cell. Initially, a default conductivity of 10^{-12} S/m is employed in the protective glass simulation model. This value is systematically increased to evaluate its impact on performance. Up until a conductivity of 0.1 S/m, minimal changes are observed. However, significant variations are noted once this threshold is surpassed, leading to comparisons being made with a conductivity value of 1 S/m. Fig. 4.14 presents the S-parameter characteristics at the input port, with simulations featuring increased conductivity compared to actual measurements within the target frequency range. Results from simulations conducted under default conductivity settings are also included to highlight the differences. While perfect alignment between simulation and measurement is not achieved, the trends observed illustrate the considerable impact of the front metallic wires on the antenna's performance. This finding is further supported by the simulated antenna gain, which is shown to drop to 2.2 dBi at 2.45 GHz, closely matching the highest measured gain recorded in the presence of the solar panel.

Following an initial investigation primarily focused on conductivity, the research direction shifted to exploring a more effective realization of the fingers and busbars in solar cells. A particular study [51] provides insight into the physical characteristics of these front lines, noting that the Ag-lattice layer on the upper surface measures 17.6 µm in thickness. This layer consists of 57 electrodes, each with a line width of 0.1 mm, along with two orthogonally oriented busbars measuring 2 mm in width. Building upon these findings, similar metallization was proposed to be placed between the ground and the transparent antenna element, as demonstrated for the single-element case in Fig. 4.15a.

A step-by-step improvement strategy was employed for the reflection coefficient analysis. Initially, the silicon thickness was increased from 30 mm to 210 mm, and the conductivity was raised to 250 S/m, as recommended in [51]. The significant increase in conductivity is attributed to the electrical conductivity of the Si layer increasing with higher light intensity, as noted in the same study. It is important to highlight that, in this first consideration, the top contact metallization was omitted, and the default simulation from the previous study is included in Fig. 4.16 for comparison purposes. In the second model, the front fingers and busbars were introduced. Subsequently, in the fourth model, the protective glass thickness was increased from 0.3 mm to 0.8 mm, as it should be significantly thicker than the silicon layer. Fig. 4.16 summarizes the investigation by illustrating the step-by-step changes, providing a clearer understanding of the frequency variations resulting from these modifications.

The single-element analysis has provided a foundational understanding of the effects

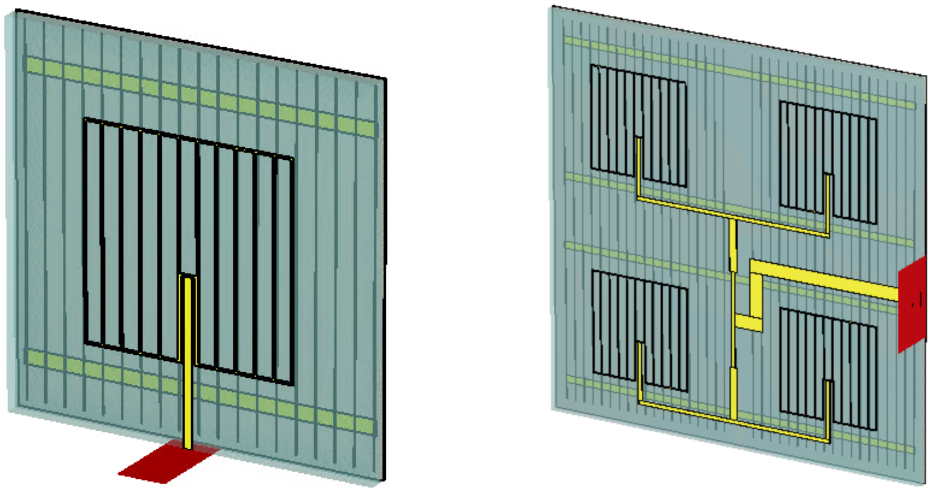

(a) (b)

Fig. 4.15. Simulation model illustrating the inclusion of the solar cell top contact for (a) the single-element design and (b) the 2-by-2 array design.

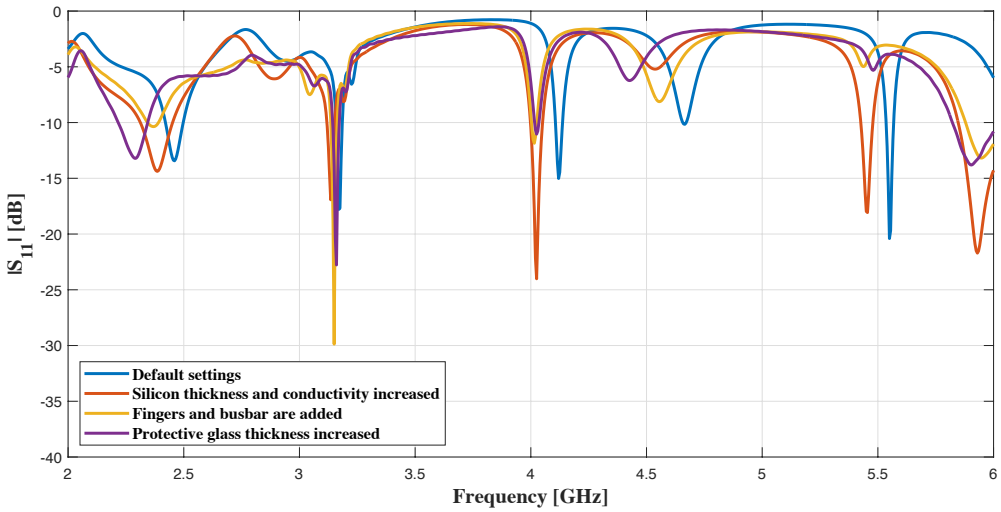

Fig. 4.16. Reflection coefficient plot for the single-element design, comparing different simulation models.

of the implemented modifications. The focus will now shift to the 2-by-2 design, which was previously fabricated, allowing for a more detailed comparison with both the experimental measurements and the prior design. This comparison aims to develop a more comprehensive and accurate simulation model. The design, incorporating all the aforementioned modifications, is shown in Fig. 4.15b. The new simulation, shown in Fig. 4.17 alongside the previous simulation and measurement data, reveals both improvements and degradations across different frequency ranges. In certain frequencies, the new simulation aligns more closely with the measurements, while in other regions, performance deteriorates. This investigation highlights the inherent

challenges in developing an accurate simulation model for solar cells. A more comprehensive study would require a detailed description of the solar cell's structure and properties. Nonetheless, it is evident that the parameters modified in this analysis have a significant impact on the results.

4.7 Conclusion of the Chapter

This chapter has provided a thorough examination of the integration of meshed antenna arrays with PV panels, demonstrating the feasibility of achieving both solar energy harvesting and WPT within a unified structure, eliminating the need for separate operational spaces. The innovation of using patch elements composed solely of vertical metal strips, with spacing optimized to the operating frequency, is a key achievement. This design not only ensured optical transparency but also delivered optimal performance in the fabricated prototypes, representing one of the most significant contributions of this thesis. Extensive analysis was conducted across various design configurations at frequencies of 2.45 GHz and 5.8 GHz, with the highest transparency patterns fabricated on glass substrates and validated through measurement. While measurements without solar panels aligned well with simulation predictions, those conducted with co-located PV panels emphasized the need for a refined model. In particular, the interaction between the PV panel's metal contacts

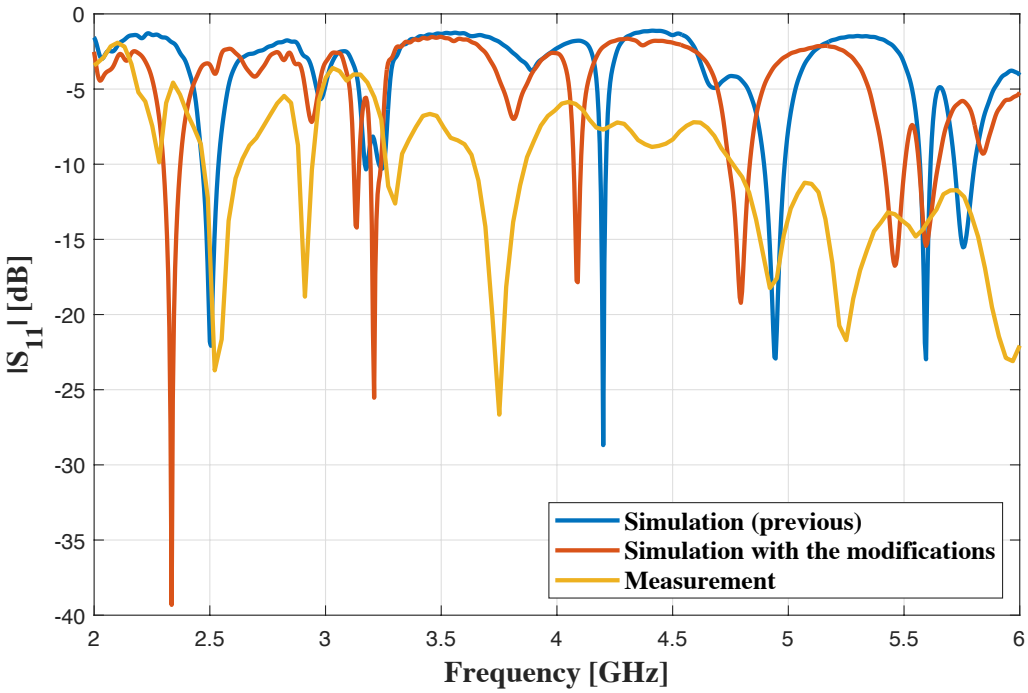

Fig. 4.17. Reflection coefficient plot for the 2-by-2 design, comparing previous simulations, the new simulation, and measurement data.

and the antenna array was shown to critically affect performance, necessitating the development of a more accurate numerical model. This finding is a crucial outcome of the thesis, shedding light on the importance of the solar panel stack-up in overall system performance. A generalized model was proposed, enhancing the conductivity within the protective glass of the PV panel, and this model was successfully validated through comparisons with measurements at 2.45 GHz.

This chapter is the cornerstone of the thesis, offering a detailed investigation of the antenna array's performance and valuable insights into the role of PV panel top contacts. It marks the conclusion of the transparent antenna-related portion of the in-space WPT system, a significant milestone in the research. Going forward, the focus of the thesis will transition to the electronic design aspects, with particular emphasis on the development of the inverter, which will drive the next phase of this work.

5 Efficient Inverter Design for Loading by Designed Transparent Antenna

5.1 Introduction to the Chapter

The inverter plays a pivotal role in RF applications, functioning as a crucial component for converting DC into high-frequency alternating current (AC) signals necessary for the efficient execution of WPT, communication systems, and signal amplification processes. Among the various inverter topologies, Class-E inverters are particularly favored due to their ability to achieve high power conversion efficiency while significantly reducing switching losses, which is critical for enhancing overall system performance. Their suitability for driving inductive loads, such as antennas, further underscores their utility in RF systems. Moreover, Class-E inverters are instrumental in facilitating impedance matching, ensuring optimal power transfer and minimizing reflections, thereby maximizing system performance in advanced RF applications.

While Class-E inverters are predominantly utilized in lower-frequency applications, such as powering train balises (discussed in a later chapter) or coil drivers in inductive coupling-based WPT systems, as outlined in [52], our goal is to extend the Class-E topology and working principles for use as a power oscillator, similar to the approach in [53]. In this scenario, switch-mode Class-E oscillators can achieve high conversion efficiencies, making them ideal for RF power sources, where efficiency and performance are crucial.

In the proposed WPT concept, the inverter represents the final critical component that bridges the solar energy harnessed by the PV cells to the transparent antenna, enabling the system to function as a power transmitter. With the system complete upon successful integration of the inverter, a fundamental element of the WPT link within the constellation is established, paving the way for future enhancements, such as the previously discussed relay node concept. However, a significant design challenge remains in relying on a single, unstable power source—the solar energy harvested from the sun. This chapter focuses on addressing these challenges through the design and critical analysis of a Class-E inverter, demonstrating through simulations how the system can maintain efficient performance despite the variability of the power source.

5.2 Design Constraints and Topology

The working principle of the Class-E inverter circuit, as illustrated in Fig. 5.1, revolves around a high-efficiency switching mechanism. It employs key components such as a choke inductor L_1, shunt capacitor C_1, and a series resonant circuit C_2-L_2, with a load

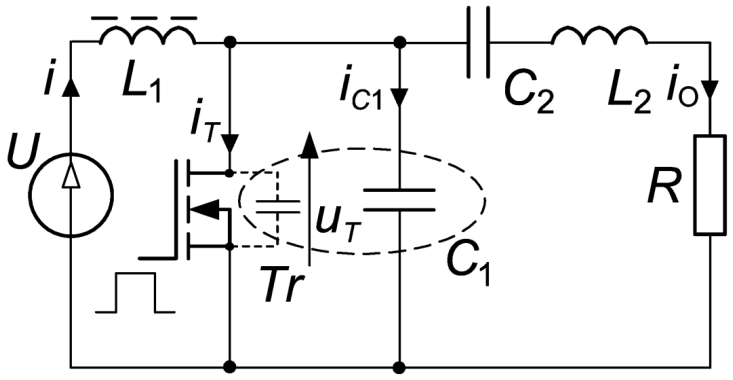

Fig. 5.1. Circuit representation of the Class E inverter [54].

resistor R and a transistor serving as the main switching device. The transistor is operated at a 50% duty cycle, ensuring that it switches on during zero-voltage switching and zero-voltage slope conditions. This switching process minimizes power losses, as both voltage and current values transition to zero during switching events, leaving only conduction losses. Consequently, the Class-E inverter can achieve efficiencies above 90%, making it highly suitable for RF and power conversion applications [54].

A significant challenge in the design of the oscillator circuit arises from the dependency on a singular DC source for the transistor, specifically a cost-effective solar panel, as previously outlined in this dissertation. This design paradigm aligns with existing literature on solar-powered active antennas [55]. In our investigation, we seek to advance this foundational study by implementing a Class-E-based oscillator, enhancing overall efficiency through the integration of High-electron-mobility transistor (HEMT) technology. More specifically, the SAV-541+ low-noise E-PHEMT transistor [56] is chosen due to its availability and compatibility with the intended operational frequency. Furthermore, the operational frequency is meticulously established at 2.45 GHz, thereby maintaining coherence with the prior design of the transparent antenna.

Additionally, a critical consideration in the design pertains to the bias voltage and its inherent fluctuations, which are contingent on solar availability. Although the solar cell utilized in this study can generate an open circuit voltage exceeding 6 V, as measured in Chapter 2 under optimal conditions on a sunny day and with a relatively large surface area, we have opted to adopt a more conservative estimate of 4 V. This adjustment reflects a realistic scenario, particularly when accounting for the operational power demands of nanosatellites, which must balance WPT with their primary functional energy consumption. It is acknowledged that the available voltage will vary based on factors such as the solar panel's orientation to the sun and environmental conditions. However, these fluctuations can be effectively mitigated through the

implementation of a suitable voltage regulator. Consequently, we have set 4 V as the bias voltage (V_{solar}) for the transistor and optimized it accordingly, while also evaluating efficiency across a range of nearby values, as discussed in subsequent section.

5.3 Simulation Results

The inverter circuit was designed and simulated using ADS, with the schematic illustrated in Fig. 5.2. Initially, the resonant circuit within the feedback loop was analyzed by examining its S-parameters before being integrated into the rest of the circuit. Key parameters were then optimized, considering a 50 Ω load, representative of the 2.45 GHz transparent antenna array, consisting of four elements, discussed in the previous chapter. The optimization and tuning process involved employing various simulation methods to refine circuit performance. Oscillation tests were conducted to ensure compliance with the Barkhausen criteria, and further analysis, including harmonic balance and transient simulations, was performed to verify the circuit's stability and performance, leading to necessary adjustments. Subsequently, minor fine-tuning of the circuit parameters was conducted to ensure optimal performance. The final optimized component values are presented in Table 5.1.

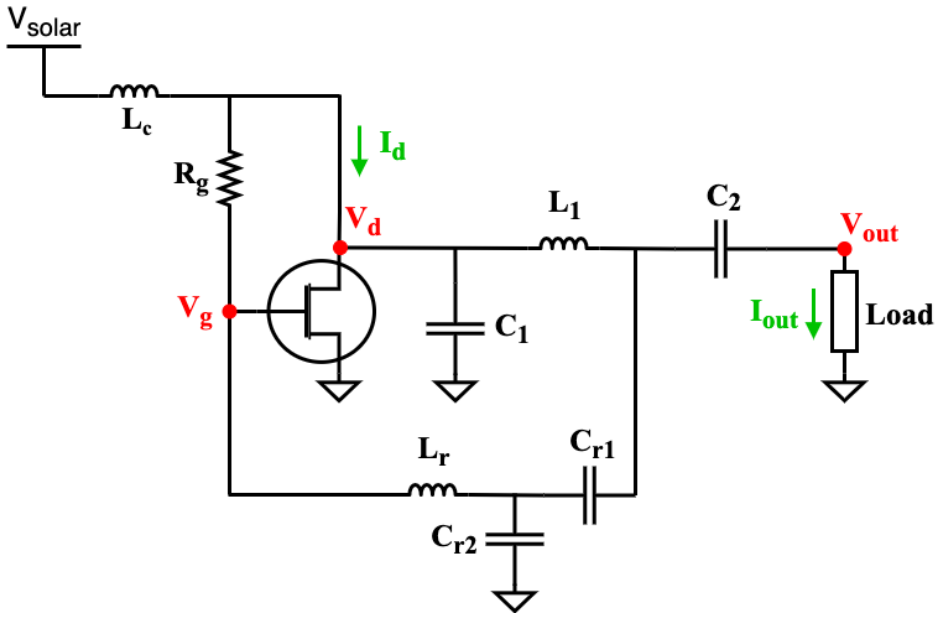

Fig. 5.2. Circuit schematic of the designed Class-E oscillator, showing generic component parameters.

Table 5.1. Optimized Circuit Parameters for Class-E Oscillator Design

L_c	R_g	C_1	L_1	C_2	C_{r1}	C_{r2}	L_r
220 nH	8 kΩ	1.8 pF	4 nH	2.2 pF	0.4 pF	0.3 pF	6.6 nH

Simulation results concerning the reflection coefficient of the oscillator test validated that the magnitude of the reflection coefficient exceeded 1, while the phase was found to be very close to 0, which meets the criteria for oscillation. The harmonic balance and transient simulation results are presented in Fig. 5.3. From Fig. 5.3a, it can be inferred that switching losses have been minimized, which is critical for achieving high efficiency. The output characteristics of the inverter, as observed in the harmonic balance simulation, are depicted in Fig. 5.3b, demonstrating good oscillation with acceptable levels of voltage and current. Additionally, the output voltage from the transient simulation is illustrated in Fig. 5.3c. It should be noted that the transient simulation exhibited significant challenges in convergence due to the high nonlinearity of the circuit. The time scale of this figure has been adjusted to display more steady-state results. Furthermore, the output frequency is illustrated in Fig. 5.3d, where a Fourier transform of the time-domain analysis is presented, clearly indicating

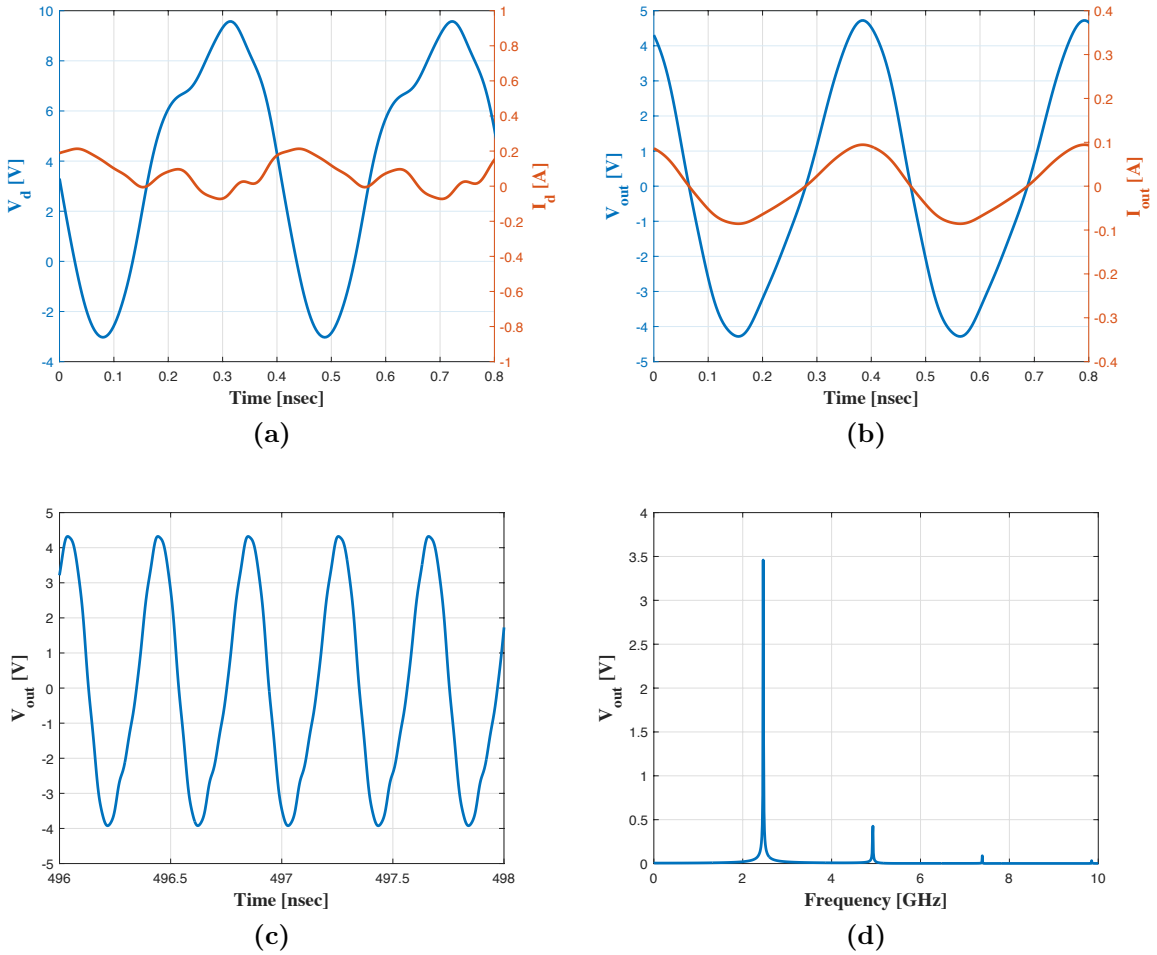

Fig. 5.3. Harmonic balance analysis illustrating (a) drain voltage and current, (b) output voltage and current, with transient analysis showing output voltage in (c) the time domain and (d) the frequency domain.

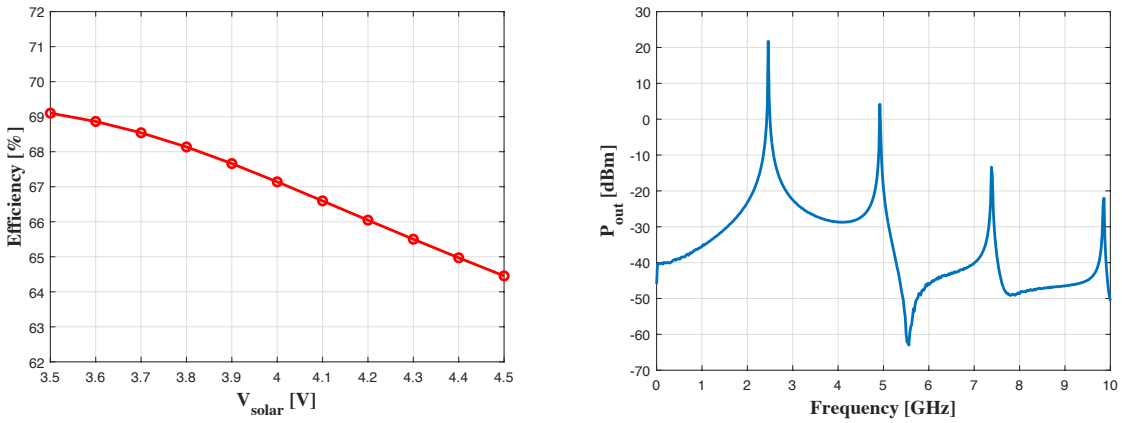

(a) (b)

Fig. 5.4. Plots showing (a) power conversion efficiency obtained from harmonic balance analysis, and (b) output power spectrum derived from transient analysis.

an output at the desired frequency. Additionally, the inverter efficiency was determined by measuring the output power at the load and the input power from the bias line. For this purpose, the solar voltage was swept from 3.5 V to 4.5 V to observe efficiency variations within this range, as shown in Fig. 5.4a. As illustrated in the figure, the efficiencies across this range are favorable, achieving 67% at a 4 V bias, which is considered optimal for this application. It is acknowledged that this value may degrade with real implementation; however, it appears promising for achieving an efficient overall WPT system. Furthermore, Fig. 5.4b illustrates the output power spectrum obtained from transient analysis and transformed into the frequency domain. The power level at the target frequency is acceptable and significantly higher than that of other harmonics, highlighting effective spectral purity—a critical measure of signal quality, indicating how "clean" and precise the signal is in frequency content. Spectral purity was calculated using the following formula:

$$SP\ [dB] = -10 \log_{10} \frac{\sum_{n=2}^{8} P_{out,n}}{P_{out,1}} \tag{5}$$

where eight harmonics were included. The numerator represents the combined power levels at harmonics other than the fundamental, while the denominator corresponds to the fundamental harmonic power level. The result is 16.8 dB, indicating that the power at the fundamental frequency is substantially higher than at other harmonics. It is noteworthy that harmonic balance simulations were initially conducted with eight harmonics, and additional simulations including higher harmonics (up to 16) yielded no significant difference in results.

Another observation involves comparing the drain power with the output power, as

a substantial portion of the drain power is expected to be converted into output power. From the harmonic balance analysis, the drain power is measured at 0.23 W, while the output power is 0.19 W under a 4 V bias. This indicates that over 80% of the drain power is transferred to the output, which is favorable. The remaining power loss can be attributed to additional losses in the feedback loop and matching network. Also, the input power from the biasing branch is measured at 0.28 W, indicating the required power for the oscillator's operation within this concept. Referring to Chapter 2, where solar readings of the low-cost solar panel were evaluated, the available power can be estimated by examining the panel's maximum power output. This approximation confirms that the input power required for the oscillator is reasonable and feasible for the prototype. It is important to note that a DC-DC converter may be placed between the solar panel and the inverter to allow for adjustable voltage, enhancing flexibility in power management.

5.4 Conclusion of the Chapter

The development and optimization of the Class-E inverter represent a significant advancement in the realm of RF applications, particularly in the context of WPT systems. By efficiently converting DC from solar energy into high-frequency AC signals, the inverter serves as a vital component that bridges renewable energy sources with transparent antenna technologies. A thorough analysis and simulation of the inverter circuit demonstrate its capability to sustain high efficiency, achieving a conversion efficiency of 67% under a 4 V bias. This efficiency is crucial for ensuring that the energy harvested from PV cells is utilized effectively, thereby enhancing the overall performance of the integrated WPT system.

Moreover, the findings underscore the importance of addressing the challenges associated with the inherent variability of solar energy as a power source. The implementation of a Class-E topology, combined with high-frequency oscillation principles, not only mitigates switching losses but also facilitates optimal impedance matching, thus maximizing power transfer and minimizing reflections. Ultimately, this research paves the way for further enhancements in energy-efficient applications, particularly in the realm of space-based systems, where reliable and efficient power conversion is essential for mission success. The successful integration of the inverter with transparent antennas stands to revolutionize energy harvesting techniques, contributing to the advancement of sustainable technologies in RF and WPT applications.

With the completion of this chapter, the focus on in-space WPT is concluded. The work presented thus far aims to demonstrate and analyze a proof of concept for in-space WPT on a small scale, utilizing low-cost, readily available components. Notably, this concept holds potential scalability for larger, more practical applications.

In such implementations, CubeSats could effectively transfer excess DC power to other CubeSats in need, enhancing resource sharing and overall mission efficiency. The subsequent chapters will shift to terrestrial WPT applications and advancements in antenna technologies. As highlighted in the introduction, the organization of the chapters does not follow a chronological sequence but is instead arranged by significance. This structure allows for a more coherent understanding of foundational concepts that have significantly influenced the trajectory of the main research presented in this thesis. The insights gained from the forthcoming chapters enriched the overall discourse on WPT and its applications, reinforcing the relevance and applicability of the research conducted.

6 Modular UHF Systems for Integrated Energy and Data Transfer

This chapter is based on the following article:

[57] A. B. Gok, F. Benassi, G. Paolini, D. Masotti, and A. Costanzo, "A wireless/wired uhf modular system combining energy and data transfer," in *2022 Wireless Power Week (WPW)*, 2022, pp. 231–234.

6.1 Introduction to the Chapter

The drive toward more intelligent systems and advanced services in industry has led to the development of concepts like the Industrial Internet of Things (IIoT), where sensors and instruments are connected to industrial applications via the internet. The growing prevalence of wireless access is enhancing cellular connectivity's role in the IIoT, expected to account for over 10% of the global IoT market, and while existing LTE systems focus on mobile broadband, challenges remain in supporting IIoT device interconnectivity, prompting increased interest in low-power wireless access solutions that offer efficient signaling, extended battery life, low costs, and broad coverage [58]. One of the key applications of IIoT is asset tracking [59], which enables manufacturers to monitor the location, status, and condition of products throughout the supply chain, both for short-range and long-range operations. Low-power wide-area networks (LPWANs) are particularly promising for wireless communication due to their extensive coverage, cost-effectiveness, and low energy consumption. One study [60] illustrates that localization in harbor environments can be effectively achieved using long range (LoRa), a radio frequency modulation technology associated with LPWANs, by optimizing parameters such as the spreading factor. Additionally, strategies such as adjusting the wake-up and sleep cycles of wireless sensor networks (WSNs) have been proposed to minimize power consumption. To overcome the limitations posed by battery-powered systems, attention has shifted towards WPT technologies.

This chapter elaborates on the development of an innovative modular system designed to enable the simultaneous transmission of energy and information between unplugged trolleys in industrial environments. By strategically integrating WPT between consecutive trolleys and guided power transfer along the edges of individual trolleys, the system effectively distributes power while supporting low-power communication sensor nodes throughout the trolley chain, drawing energy solely from the locomotive. Communication among the trolleys and the locomotive is facilitated through battery-less LoRa nodes, enhancing long-range communication capabilities. The modularity of the system is further underscored by the concurrent design of its

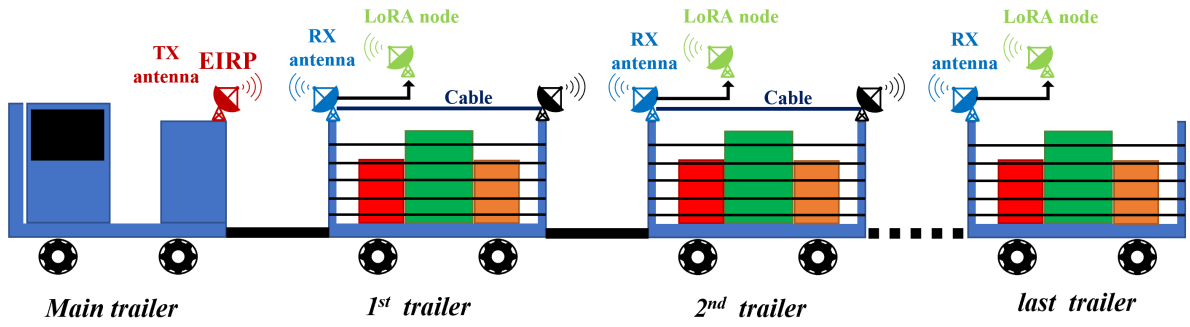

Fig. 6.1. Pictorial representation of a train of unplugged trailers embedding WPT and LoRa communication [57].

components, which include a radiating system, a power splitter, and a rectifier specifically engineered to deliver a substantial portion of available power even at low input power levels, ensuring efficient energization of the LoRa nodes. Notably, the system maintains reliable communication regardless of the position or arrangement of each trolley within the chain. Operating at a frequency of 2.45 GHz for both power and data transmission, the system's efficacy has been theoretically predicted and experimentally validated in a multi-trolley configuration spanning 10 meters, utilizing a transmitted power of 36 dBm that adheres to regulatory standards, thus representing a significant advancement in industrial applications.

Fig. 6.1 provides an overview of the system implementation. The first chart displays the active power transmitter, while the subsequent charts show pairs of wireless front-ends positioned on the left and right sides. These front-ends are linked by a low-loss coaxial cable running the length of each chart. The system begins with the main trailer, which acts as the primary energy source. Power is transmitted through an antenna located at the rear of the carriers and is received by an antenna at the front. At each receiver, a power divider distributes part of the energy to the LoRa node, with the

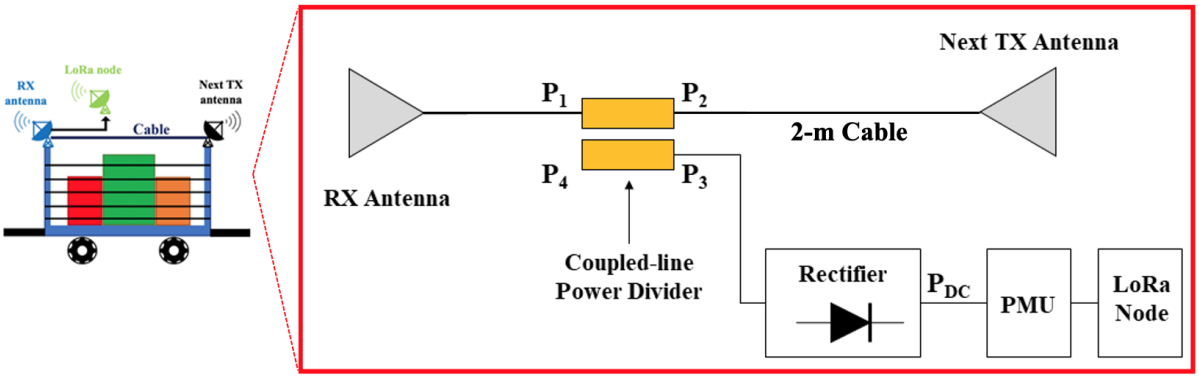

Fig. 6.2. Circuit block details embedded within each trailer: at the receiving front-end, a power splitter distributes the incoming power between the rectifier input and the cable, which directs the remaining RF power to the opposite end of the trailer, where the transmitting antenna is positioned [57].

remainder being sent to the next transmitting antenna via cables.

Fig. 6.2 presents a block diagram illustrating the system installation. On the left side of the diagram, a power receiving module is depicted, which distributes power between a rectifier, supplying a LoRa node, and a cable that transmits power to the right side of the diagram. There, a radiating element serves as a power transmission station for the next stage, establishing a cascading scenario. The practical implementation of this system imposes constraints in terms of dimensions and operational distances, which are critical parameters for the efficient design of the entire system. One of the primary design challenges is optimizing the system to recharge the maximum number of trailers, and therefore LoRa nodes, within the shortest possible time, ensuring continuous communication. Additionally, emphasis is placed on developing a modular system that maintains performance even if the trailer order changes.

6.2 Choice of Radiating Element: 32-Patch Antenna Array

Considering the operational context and environment of the system, patch antennas were selected as the optimal topology, primarily due to the presence of a ground plane that mitigates sensitivity to the underlying material, which is predominantly metal. These antennas, dedicated to WPT, are placed at the right edge of each stage, with an approximate reference distance of 50 cm between stages. Thus, a balance between size and performance is crucial to ensure efficient power transfer across multiple trailers.

The antenna array is fabricated on Rogers 4350B substrate ($\epsilon_r = 3.66$, $tan\delta = 0.0037$) with a thickness of 1.52 mm. To optimize antenna gain while maintaining compact dimensions, a 32-patch array was implemented, achieving an overall gain of 17 dBi at 2.45 GHz. Fig. 6.3 presents an image of the fabricated antenna, along with the integrated power splitter and rectifier. Fig. 6.4a and 6.4b depict the measured and simulated S_{11} and far-field radiation patterns, showcasing excellent correlation between both results. The antenna occupies a total volume of 487 x 287 x 1.52 mm^3, which was

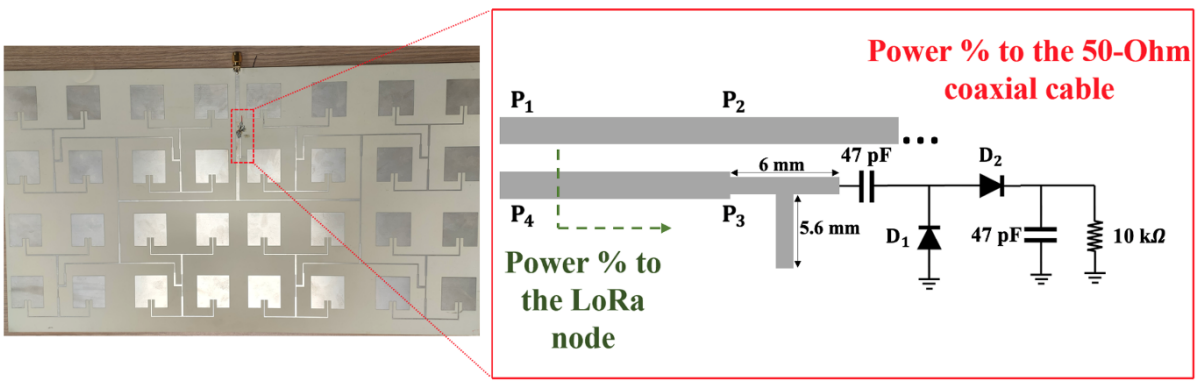

Fig. 6.3. The fabricated antenna array featuring an integrated power splitter and rectifier [57].

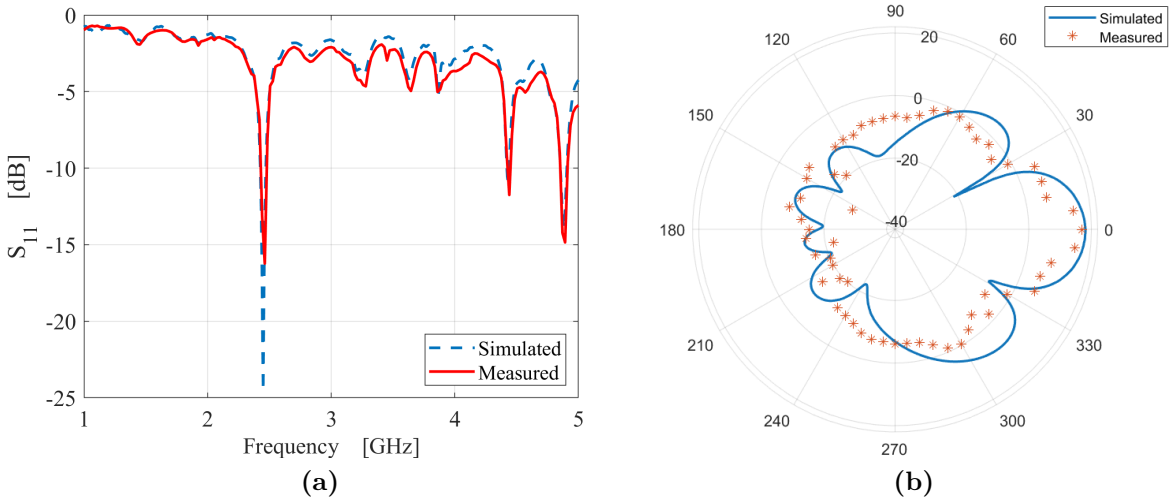

Fig. 6.4. Measured and full-wave simulated performance of the array: (a) antenna reflection coefficient; (b) logarithmic radiation patterns in the E-plane [57].

determined to be the optimal balance between performance and size, considering the antennas need to be mounted on the metal walls of industrial trolleys. While doubling the antenna's dimensions could theoretically increase the gain by 3 dB, it would also result in a more cumbersome structure and a larger, more complex meandered array feed network, potentially introducing additional losses.

The high gain of the antenna array, necessary for reliable wireless power transmission between trailers, aligns well with the anticipated line-of-sight positioning of antennas on adjacent stages. Each trailer is equipped with two antennas, connected by a high-performance 2-meter, 50 Ω coaxial cable, which exhibits an attenuation of 0.66 dB at 2.45 GHz.

6.3 Power Budget Assessment and Rectifier Design

Preliminary calculations have been conducted for a system consisting of four trailers, each measuring 2 meters in length, to estimate the received power at each wireless link and account for the cable attenuation when connecting the two antennas within the same trailer. Since the primary objective is to charge the LoRa node on each trailer, a power splitter is integrated into each receiving array to allocate the minimum required power to the LoRa node, while transferring the majority of the power to the far end of the trailer via the coaxial cable. A power management unit (PMU) ensures that the storage capacitors are charged to a sufficient voltage level for the LoRa nodes.

A key design objective is determining the optimal power splitting ratio to ensure adequate power for recharging the final LoRa node while maximizing the number of trailers that can be supported. Although an initial approach could involve setting a fixed power splitting ratio, given that the first trailer receives more power than the

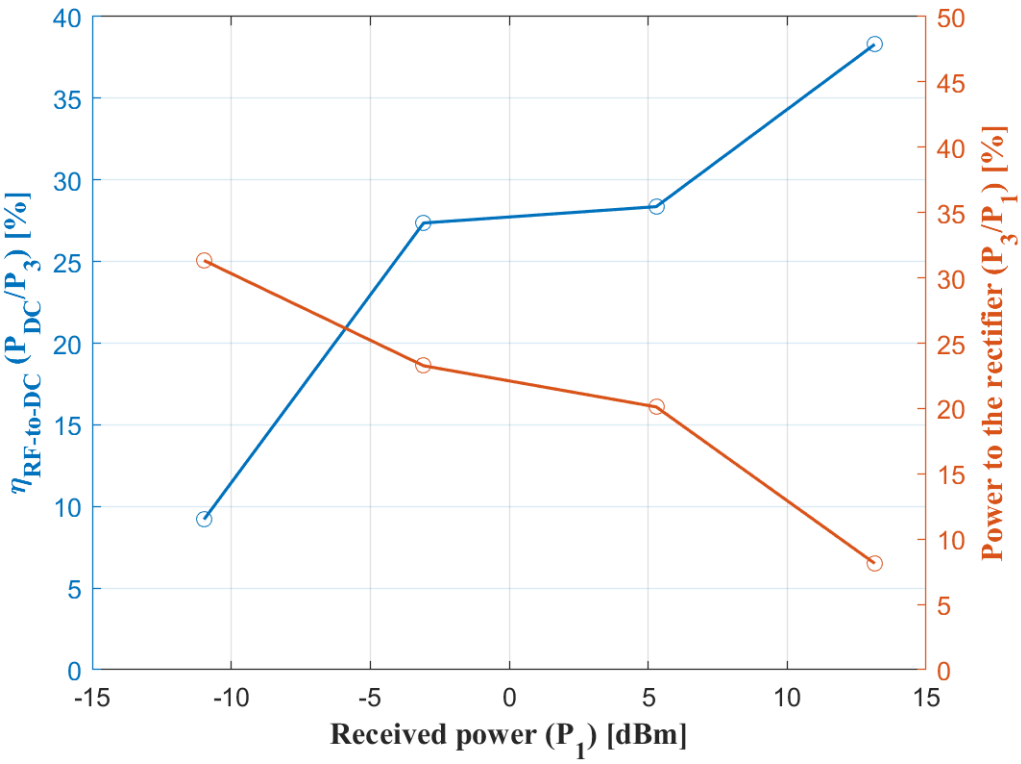

Fig. 6.5. Measurement results of power conversion efficiency and the power splitting percentage directed to the LoRa node branch as a function of the received power at the antenna array [57].

subsequent ones, a variable power distribution strategy has been adopted. Specifically, trailers farther from the source, which receive less power, are allocated a higher percentage of the available power compared to the first trailers, which receive a greater initial power input.

A coupled microstrip line power splitter has been developed on the same substrate as the antenna to provide varying RF power percentages to the rectifier and the coaxial cable. The entire subsystem, which includes a voltage-doubler rectifier (comprising diodes D_1 and D_2, represented as Skyworks SMS7630-079LF, and 47 pF capacitors), has been designed using a full-wave model of the antenna array within a nonlinear simulator to optimize the geometry of the structure. This optimization aims to achieve the highest RF-to-DC efficiency at lower power levels, thereby ensuring reliable powering of the most distant LoRa node. For this purpose, a suitable load of 10 kΩ has been selected based on the aforementioned optimization criteria.

Referring to Fig. 6.3, the efficiency is expressed as follows:

$$\eta_{RF-to-DC} = \frac{P_{DC}}{P_3} \tag{6}$$

$$P_3 = |S_{31}|^2 P_1 \tag{7}$$

The measured RF-to-DC efficiency is illustrated in Fig. 6.5. The constraint on the power distribution has resulted in the rectifier efficiency not reaching its potential maximum, as would be observed in a standard rectenna configuration. Additionally, the measured percentage of power entering the rectifier input is presented in Fig. 6.5, varying from approximately 8% to 31% relative to the power received by the antenna.

Moreover, Table 6.1 presents a summary of the measured performance for each of the four passive trailers considered in this study. It has been observed that the system effectively adjusts the power splitter ratio to the rectifier in response to decreasing total received power. The RF input power and RF-to-DC efficiency are detailed in the third and fourth rows, respectively. As previously mentioned, these values are not optimized for maximum performance but are tailored to ensure overall system effectiveness for enabling LoRa communication across the maximum number of trailers.

The penultimate row indicates the measured time for the PMU ePeas AEM30940 during a cold start, referencing the performance of 1 mJ power consumption reported in the literature. In this implementation of LoRa node communication, the proposed WPT chain successfully activates the fourth LoRa node in under four minutes. The final row of Table 6.1 specifies the power delivered to the subsequent transmitting antenna within the same trailer, which corresponds to the previously defined remaining power after accounting for coaxial cable attenuation.

6.4 Conclusion of the Chapter

This study presents the design, implementation, and measurement of an innovative microwave system capable of facilitating wireless power transfer and communication for tracking applications, utilizing LoRa technology. The proposed system is applicable in various industrial environments to monitor the operational integrity of a fleet of trailers.

Table 6.1. Overview of the system's measured performance [57].

Trailer #	*1*	*2*	*3*	*4*
Received power at the front edge (P_1) [dBm]	13.15	5.29	-3.08	-10.98
Power splitter ratio to the rectifier [%]	8.14	20.12	23.27	31.33
Rectifier input power (P_3) [dBm]	2.26	-1.69	-9.43	-16.02
RF-to-DC efficiency [%]	38.30	28.36	27.36	9.20
Charging time of LoRa node [s]	4.1	14.2	22.1	226.6
Transmitted power at the back edge [dBm]	12.12	3.65	-4.91	-13.27

Each trailer, though disconnected from power sources, can communicate its status using battery-less LoRa nodes that are recharged through a cascading arrangement of antenna arrays. The performance results demonstrate the system's ability to wirelessly power up to four passive trailers, thereby enabling straightforward LoRa data transmission that is beneficial for tracking purposes.

Furthermore, this work underscores the critical role of antenna arrays in WPT within the context of combined energy and data transfer in industrial applications. It also illuminates pathways for advancing space-based WPT technologies and their potential applications in transparent antenna scenarios.

7 Minimized Ground Plane Design for Bidirectional WLAN Monopole Antennas

This chapter is based on the following article:

[61] A. B. Gok, F. Benassi, D. Masotti, and A. Costanzo, "Bidirectional monopole antenna array with minimized ground plane for wlan applications," in *2023 17th European Conference on Antennas and Propagation (EuCAP)*, 2023, pp. 1–4.

7.1 Introduction to the Chapter

Printed monopole antennas have garnered significant interest, particularly for WLAN applications [62], due to their advantages, including low profile, compact size, wide bandwidth, quasi-omnidirectional radiation characteristics, and ease of integration with microstrip circuits. While the omnidirectional capabilities of monopole antennas have been widely utilized, bidirectional antennas are increasingly favored for applications in elongated and narrow environments, such as indoor corridors and tunnels [63]. A single-element monopole antenna performs well in confined spaces or towards specific directions but exhibits limited range due to its low power gain. To enhance the operating range, employing an array of multiple single-element antennas presents an effective solution, simplifying complexity while maintaining a compact design. Despite the benefits of monopole antenna arrays, research in this area has been limited, largely due to their strong dependence on the ground plane [64]. The size of the ground plane can significantly affect the overall radiation performance of the array, particularly by altering both the impedance bandwidth and the radiation pattern. Various methods have been explored to mitigate the negative impacts of the ground plane, and different approaches have been employed to improve the gain of monopole antenna arrays.

This chapter presents a printed monopole antenna array designed to operate at 2.45 GHz, featuring an innovative minimized ground plane configuration. It emphasizes the methodologies employed to investigate and mitigate the impact of ground plane size on the performance of the microstrip feeding network. The optimized ground plane design leads to a substantial reduction in side lobe levels while simultaneously enhancing both gain and bandwidth. Nevertheless, although a compact ground plane is critical for improving array performance, there exists a threshold beyond which further minimization is impractical. This necessitates a careful equilibrium in the pursuit of optimal dimensions. The intricacies of this delicate trade-off are discussed in the following sections.

7.2 Configuration of the Antenna and Feeding Network

The antenna is fabricated on an economical and robust FR4 substrate with a relative permittivity of $\epsilon_r = 3.68$, a loss tangent of $tan\delta = 0.0035$, and a thickness of 1.5 mm, specifically tuned to operate at 2.45 GHz for WLAN communication systems. The array consists of four printed monopole antennas functioning as a broadside antenna. The radiating elements and the feeding network of the proposed four monopole antenna design are illustrated in Fig. 7.1a, and these components are integrated into the top layer. The length of each monopole has been determined in accordance with standard guidelines, ensuring that the element length is approximately $\lambda/4$, where λ represents the resonance wavelength.

Considering an input impedance of 50 Ω for the array feeding network, the individual elements of the array are supplied by a 100 Ω microstrip line, with a quarter-wave transformer employed to facilitate a seamless transition to the 50 Ω input impedance. Additionally, since the upper and lower pairs of elements are energized

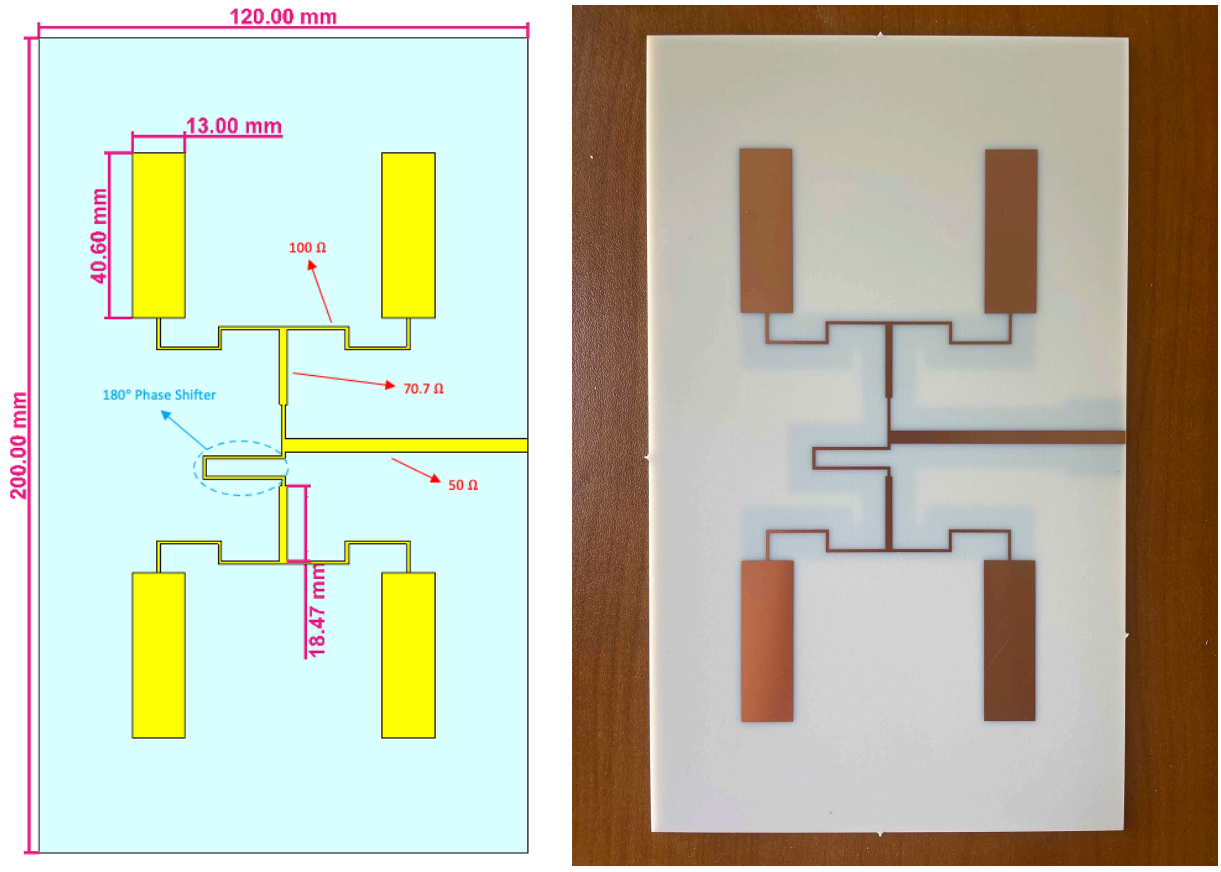

(a) (b)

Fig. 7.1. Top view of (a) the design of a 2-by-2 monopole array, where the feeding network is implemented using microstrip technology with a bottom ground plane, and (b) the top view of the manufactured prototype [61].

from opposite directions, a 180° phase shift between these pairs is essential.

Although the horizontal spacing between the elements is set at $\lambda/2$ to minimize sidelobe level (SLL) and mitigate coupling effects between the element pairs, the incorporation of a quarter-wave transformer and a meandered line for phase shifting necessitates a deviation from maintaining a uniform vertical spacing. To optimize the configuration further, the 100 Ω lines feeding the monopoles have been designed with a meandered structure, effectively reducing the vertical separation between the antenna elements, as illustrated in the schematic representation in Fig. 7.1a.

7.3 Reference Monopole Antenna and Optimized Ground Structure

For the initial phase of this study, a reference four-element monopole antenna was designed with a conventional full ground plane, as depicted in Fig. 7.2a. This configuration serves as a baseline for further optimization, which will be elaborated upon in subsequent sections. The ground plane dimensions were carefully selected to fully encompass the horizontal extent of the array, while the vertical dimension was truncated just beneath the monopoles, following standard design protocols for this type of antenna. Preliminary full-wave simulations of this configuration were performed, yielding a SLL of -5.9 dB. The SLL, defined as the ratio of the main lobe's peak

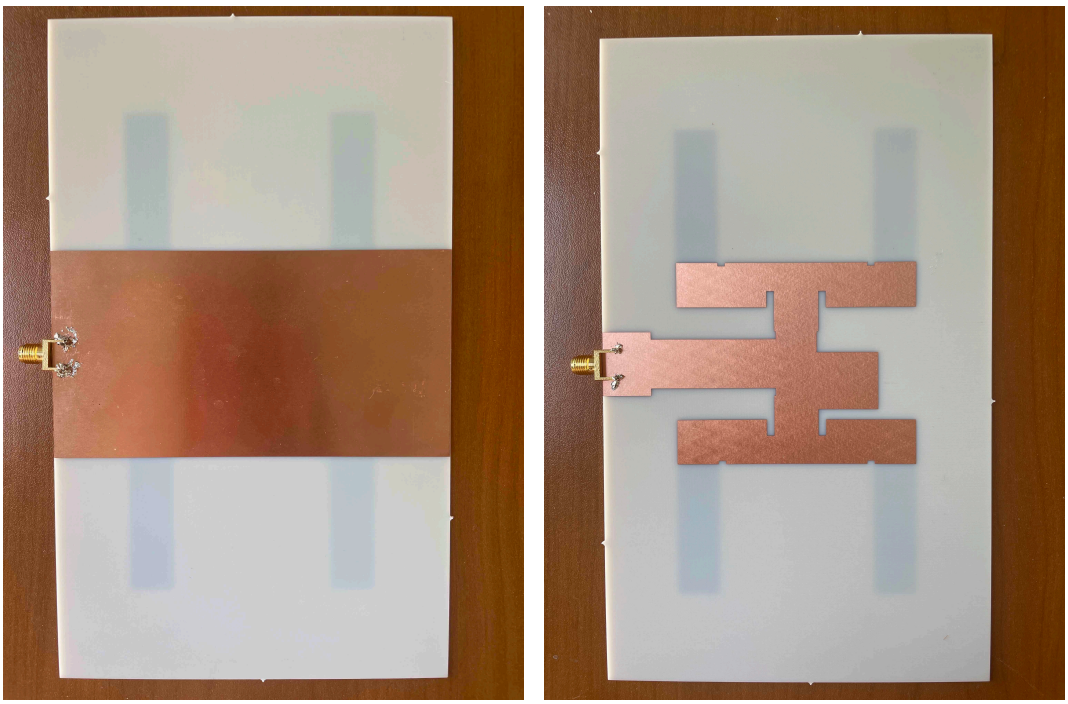

(a) **(b)**

Fig. 7.2. Ground configurations: (a) standard (reference); (b) optimized design [61].

amplitude to the side lobe's peak amplitude, was adversely affected by parasitic radiation from the large ground plane, highlighting a critical area for improvement.

To enhance the performance of the monopole antenna array, careful modifications to the ground plane are required to avoid any adverse impact on the feeding network. A variety of ground plane shapes and sizes were analyzed to assess their influence on the antenna's radiation characteristics. The optimized ground plane configuration is depicted in Fig. 7.2b. This design was initially developed by replicating and systematically enlarging the layout of the feeding network situated on the top layer, as illustrated in Fig. 7.1b. Following this, the structure was further expanded along its perimeter by introducing a margin, denoted as M, shown on the left side of Fig. 7.3. The parameter M was meticulously optimized to evaluate its impact on the radiation properties of the array, ultimately achieving the optimal balance between ground plane size and its influence on the antenna's radiation characteristics and feeding network performance.

The enlargement process follows the same approach as previously outlined, with the exception of adjustments made at the termination of the 50 Ω feeding line, where the waveguide port for numerical simulations is placed. This region must maintain dimensions at least equal to the waveguide port to ensure accurate simulation outcomes. Additionally, the portion of the ground plane in proximity to the monopole radiating element is excluded from this tuning process, as altering it would significantly influence

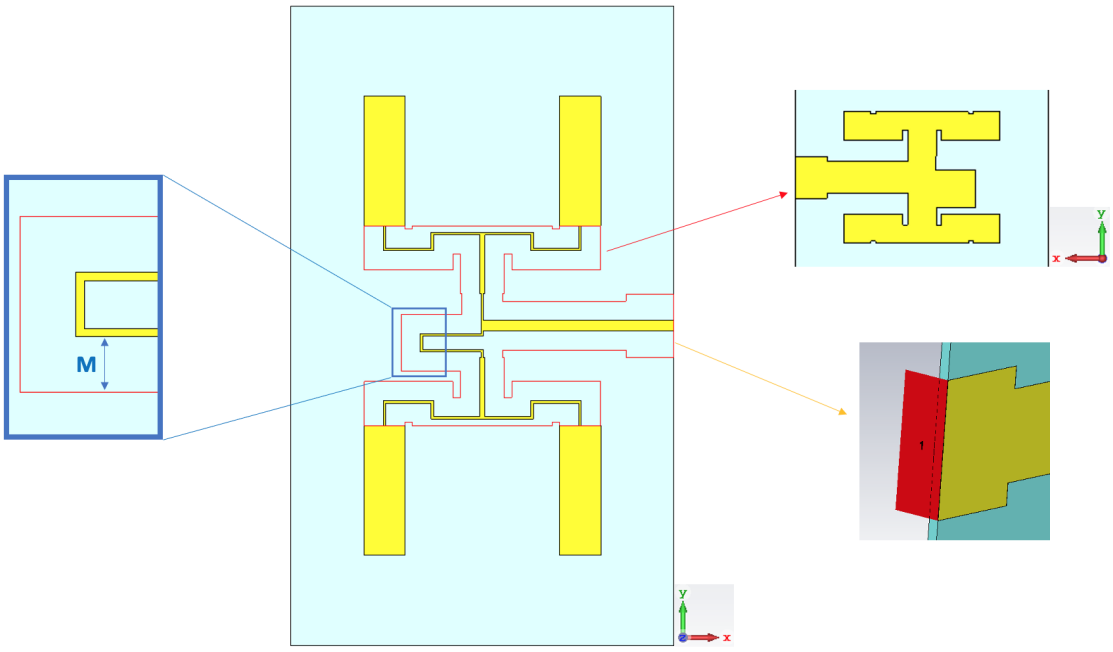

Fig. 7.3. Visualization of the ground plane relative to the top layer. The feeding network is extended using the variable M to achieve the distinct shape of the ground structure. The ground plane dimensions near the simulation port are adjusted to match the port size, ensuring consistent and reliable results [61].

the tuning of the monopole. This area is integral to the antenna structure and has a substantial impact on the overall array performance, including the operating frequency.

7.4 Results and Comparative Analysis

To evaluate the impact of ground plane size on antenna performance, full-wave simulations were conducted on the complete structure with incrementally increasing ground plane dimensions. These results were compared with those of the standard structure depicted in Fig. 7.2a. The findings are summarized in Table 7.1. In addition to the reference structure, the smallest and largest meandered ground planes were achieved for $M = 3$ mm and $M = 7$ mm, respectively.

Table 7.1 clearly illustrates that a minimized and meandered ground plane enhances the antenna's radiation performance compared to the reference case. However, adjusting the parameter M, which results in an increase in ground plane size, further improves both the antenna gain and the SLL. The design with $M = 6$ mm is identified as the optimal case, as additional increases in size do not significantly affect the results.

Fig. 7.4a presents the normalized radiation patterns of the antenna, comparing the standard and minimized ground plane configurations using both simulated and measured data. The polar plots distinctly demonstrate improvements in antenna gain and SLL, with measurement results confirming these enhancements. Additionally, the bidirectional radiation pattern of the optimized design, exhibiting a directivity of approximately 9.6 dBi, is evident in the same figures. Moreover, Fig. 7.4b illustrates the reflection coefficient (S_{11}) at the input port of the array over the frequency range of 2-3 GHz. The measured results for the optimized structure reveal an impedance bandwidth ($|S_{11}| < -10$ dB) of 510 MHz (2.32-2.83 GHz), which exceeds that of the reference design. At the end, the $|S_{11}|$ reaches as low as -23 dB at the operating frequency of 2.45 GHz.

Table 7.1. Radiation characteristics of the antenna for various ground plane sizes and shapes [61].

Ground Structure	**Gain [dBi]**	**SLL [dB]**	**Directivity [dBi]**
Standard (Reference)	7.30	-5.9	7.89
M = 3 mm	8.92	-9.9	9.63
M = 4 mm	9.02	-10.4	9.64
M = 5 mm	9.04	-10.6	9.59
M = 6 mm	9.05	-11.2	9.64
M = 7 mm	9.07	-11.2	9.66

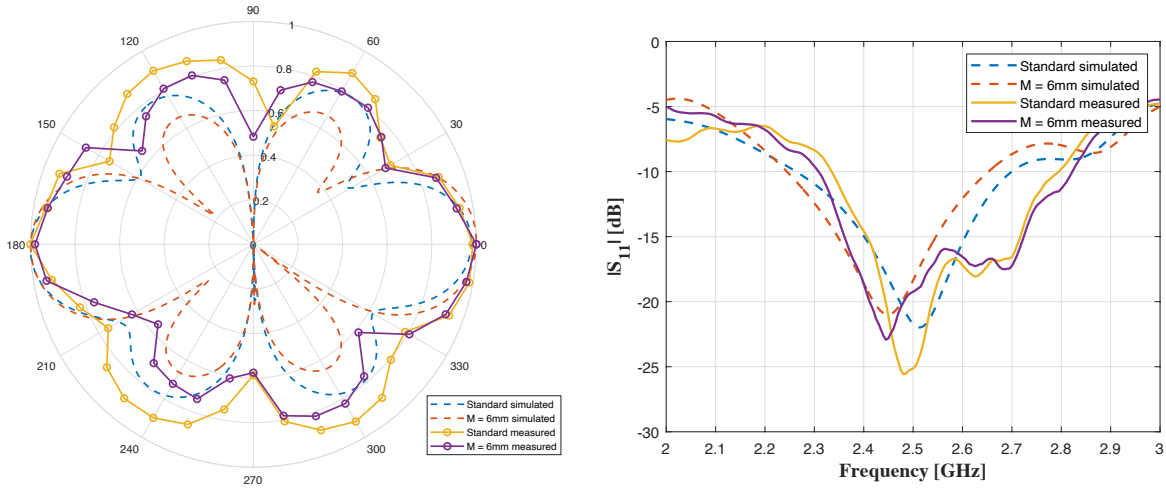

(a) (b)

Fig. 7.4. Simulated and measured (a) normalized radiation patterns of the monopole array and (b) reflection coefficient graphs at the input port of both the standard antenna and the proposed antenna featuring a minimized ground plane ($M = 6$ mm) [61].

7.5 Conclusion of the Chapter

In summary, a new bidirectional monopole antenna array, optimized for WLAN applications, has been developed and rigorously analyzed through simulation and measurement. The design comprises four monopole elements operating at 2.45 GHz. Several ground plane configurations were explored, with a detailed comparison conducted across different designs. The configuration offering the best balance between antenna performance and size achieved a peak gain of 9 dBi in both broadside and opposite directions. This design also demonstrated superior side lobe suppression. The findings reveal that the relationship between array performance and ground plane size is complex, as smaller ground planes do not necessarily yield better results, emphasizing the need for careful optimization. The design process for the 2-by-2 array has been validated through measurements and can be easily extended to larger monopole arrays.

This chapter, like Chapter 6, delves into antenna array technology, but with a stronger focus on communication systems. The exploration of monopole antenna arrays in this context broadens our understanding of their potential across various applications. The innovative ground plane design and advanced feeding network techniques presented in this work provide fresh insights and perspectives. These findings have also sparked the development of novel approaches, opening new avenues for research into transparent antennas, particularly regarding their potential applications in space and satellite technologies.

8 Class-E Amplifier-Driven Telepowering Units for Enhanced Balise Transmission Efficiency

This chapter is based on the following article:

[65] A. B. Gok, M. Shanawani, A. Moriconi, T. Salmon Cinotti, D. Masotti and A. Costanzo, "Efficient Telepowering Unit for Balise Transmission Modules Using Class-E Amplifier," *IEEE Transactions on Transportation Electrification* [Submitted].

8.1 Introduction to the Chapter

In this chapter, my involvement in the project addressing the efficient powering of train balises is presented. The focus of the work centers around telepowering systems, which have traditionally played a vital role in modern railway infrastructure. Train balises, standardized across global railway systems, serve as essential position sensors that communicate critical information to onboard train systems. When a train approaches a balise, it triggers the telepowering process, allowing for the transmission of position data and other necessary details to the onboard antenna. It transmits essential control information, such as track layout, stops, direction, and speed limits, through uplink signals in the form of balise telegrams. Any errors in the wireless transmission of this information can directly impact the train control system, potentially causing accidents.

As depicted in Fig. 8.1, the balise system comprises the ground-based balise and the Balise Transmission Module (BTM), which integrates both the BTM antenna and host unit. During the information exchange between the train and the balise, the process is initiated by telepowering, wherein the BTM antenna activates the balise through excitation signals [66]. Subsequently, the uplink phase follows, during which the balise transmits vital data, including speed limits and temporary speed restrictions, to the BTM antenna. This information enables the train to dynamically adjust and regulate its speed in real time, ensuring safe and efficient operation.

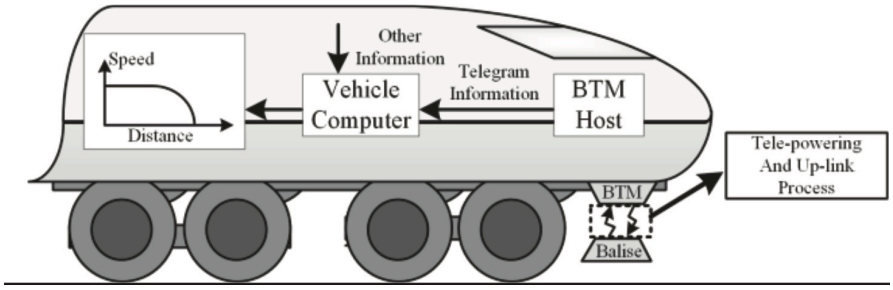

Fig. 8.1. Operational mechanism and visualization of the balise system [66].

A key challenge in this area lies in the suboptimal power efficiency of current systems. Issues such as impedance mismatches between the antenna and transmission lines, as well as the distance between telepowering sources and onboard antennas, result in energy losses. Traditional designs typically consume up to 65 W of power [67], far more than what is actually required to activate balises. This project has sought to address these inefficiencies by introducing an innovative approach that significantly reduces the power consumption while maintaining compliance with European railway standards [68, 69].

The inverter design for the WPT system presented in this thesis is fundamentally rooted in the outcomes of this project, particularly the design of the Class-E amplifier discussed earlier. The insights and experimental data gathered from this work have been instrumental in shaping the advancements detailed in this thesis, serving as a critical foundation for further development and optimization.

8.2 System Architecture and Functional Overview

The typical design architecture of the system is illustrated in Fig. 8.2. The Balise Transfer Module (BTM-TX) on board the train is connected to the antenna via a transmission line (TXL), which is approximately 20 meters in length. The BTM-TX continuously transmits the telepowering signal through the on-board antenna. When the train passes over a functional balise, the antenna captures the generated telegram and relays it through the TXL to the BTM-TX. Following this, the BTM-TX filters out unwanted signals before passing the processed signal to the Balise Receive Module (BTM-RX), which is typically mounted adjacent to the BTM-TX via another transmission line.

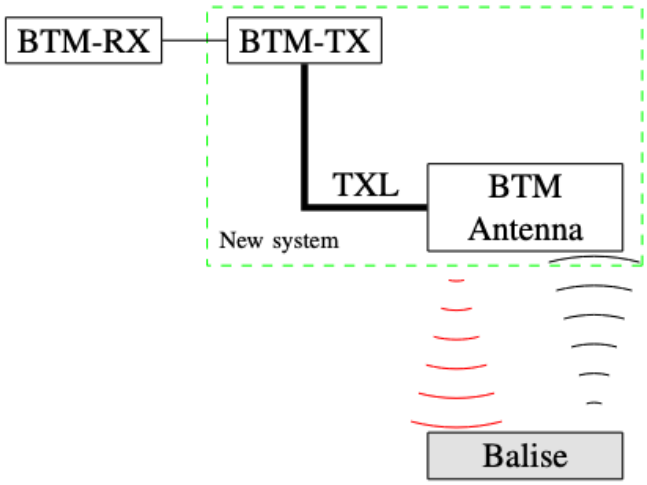

Fig. 8.2. Topology of balise-train communication. The on-board antenna transmits the telepowering wireless signal (red) and receives the telegram wireless signal (black).

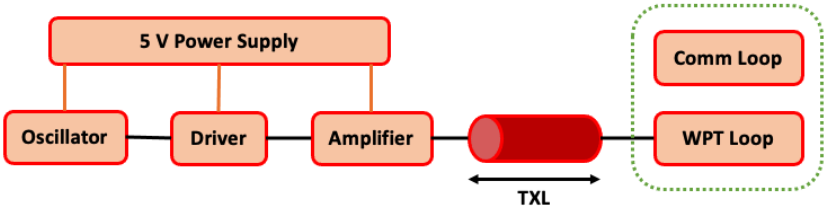

Fig. 8.3. Schematic diagram of the proposed BTM-TX system.

The newly developed system is comprised of multiple functional blocks, as shown in Fig. 8.3, designed to enable continuous telepowering transmission at 27.095 MHz. In this configuration, the entire BTM-TX is replaced by a single PCB housed within the antenna enclosure. The PCB is powered by a 5 V supply unit, derived from the train's primary 24 V DC source, to operate the oscillator, driver, and Gallium nitride (GaN) transistor. The minimal phase noise jitter is expected to have negligible effects on the stability of the Class-E amplifier employed in the system. Additionally, a communication loop antenna, incorporating a filter, has been designed to receive telegram signals at 4.234 MHz from the balise via a balanced connection to the BTM-RX circuitry.

In the next stage, the LMG1020 gate driver is utilized to drive the GaN transistor, improving the speed of both the rising and falling edges of the driver response. The series resistances between the driver and the GaN device are critical, as they directly impact the switching performance. The amplifier consists of the nonlinear GaN transistor and a network of reactive components that form a Class-E amplifier, optimized for impedance matching to the load. Class-E amplifiers operating at this power and frequency typically require a low load impedance of around 2 Ω, while the connecting cable possesses a characteristic impedance of either 50 Ω or 75 Ω, as is the case in this system. Matching the amplifier to the load, given the large impedance difference, necessitates a carefully designed matching network, which must account for both power requirements and insertion loss. The antenna input impedance, examined using emulation measurements from existing technology, is identified as being approximately 50 Ω. Given that most available antennas are inductive loops, it is unlikely that the real part of the antenna impedance aligns closely with this frequency due to the antenna's dimensions. In this proposed system, the TXL is integrated as part of the matching network, allowing the circuit to be tuned effectively to the telepowering antenna, which consists entirely of reactive components. This design approach serves to minimize power consumption within the antenna.

8.3 Antenna and Circuit Design for Train Balise Activation

In this section, the methodology for calculating the EM power required for the activation of the balise is presented, commencing with the determination of magnetic field intensity at a specified height and a comparison of theoretical calculations with empirical data derived from simulations conducted in CST. The influence of enclosure dimensions on the impedance characteristics of the loop antenna is examined, and the interoperability of the system with concurrent systems is evaluated. Certain detailed calculations are deliberately omitted, and the reader is referred to the aforementioned paper for further verification.

Accurate assessment of the power required for balise activation is essential for establishing minimum thresholds for electrical parameters, including current and magnetic flux of the BTM-TX. For the sake of simplicity, it is assumed that the coupling between the BTM-TX antenna and the balise is minimal, thus not significantly affecting the magnetic flux or the loop resistance. With a total loop resistance estimated at 1 Ω—a value that accounts for connections and soldering, albeit overestimated—the real power consumed by the loop is calculated to be 1 W. In opposition to the aforementioned consumption of 65 W, this notable disparity emphasizes the potential for a substantial reduction in the power required for balise activation through meticulous system engineering.

The antenna model was simulated in CST software within a rectangular metal enclosure as shown in Fig. 8.4a, with a wall thickness of 30 mm chosen to meet mechanical requirements. A parametric sweep analyzed the impact of the spacing between the outer loop and the metal box, revealing that the real part of the loop's

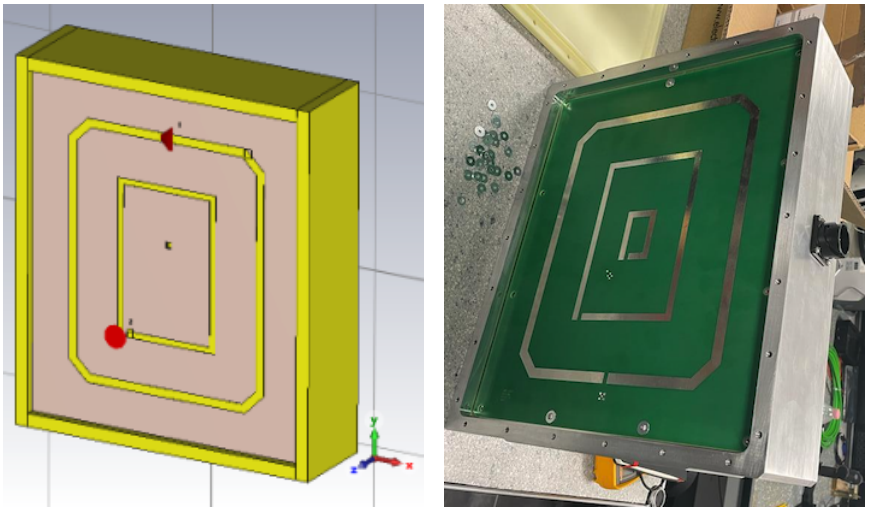

(a) **(b)**

Fig. 8.4. (a) 3D simulation model of the realized unit from CST and (b) the image of the constructed unit.

input impedance remained constant at 0.2 Ω across all spacing values, while the imaginary part increased from 95.49 Ω at a spacing of 25 mm to over 105 Ω at 45 mm. To ensure adequate power for the balise while preventing unintended activation of nearby balises, minimum and maximum magnetic flux values were established. A simulation scenario at a specified height identified three distinct regions of the magnetic field distribution: the main lobe zone, side lobe zone, and cross-talk zone. The maximum acceptable limit for cross-talk was set at -60 dB, which was met according to the distribution pattern. The magnetic flux in the balise equivalent loop was calculated using dimensions defined the relevant standard [68], yielding a standard balise size of 358×488 mm^2. The magnetic flux equation was applied iteratively along the x-axis, with a loop current of 1 A used to establish the magnetic flux curve. Adjusting the current to 3 A raised the minimum required magnetic flux threshold to 2.6 nVs. Analysis indicated that for high-speed trains traveling at speeds exceeding 300 km/h, the balise remains activated for less than 7 ms while the antenna unit moves.

In compliance with regulations, the WPT and communication systems must remain operational during train movement. The communication loop detects balise telegrams at a carrier frequency of 4.234 MHz, utilizing a filter to match the loop's predominantly reactive impedance to the TXL and to allow the useful bandwidth defined by Frequency-shift keying (FSK) modulation. A filter was implemented to reduce power insertion loss within the passband and improve signal matching between the communication loop and the receiver, enabling effective detection of both the FSK signal and a portion of the telepowering signal at 27.095 MHz. If the telepowering signal is not detected, control alarms trigger protective measures.

8.3.1 Description of the Telepowering Circuit Design

After discussing the overall system and the antenna component of the balise powering system, attention can now be directed to the primary focus of this thesis: amplifier design. The circuit is based on a Class-E topology, chosen for its load-independent operation, which enables the WPT system to sustain efficiency despite variations in loading [70]. Given the predominantly inductive nature of the loop impedance, compensating for the inductive reactance necessitates the inclusion of series capacitors capable of withstanding high currents. To manage the voltage drop across each capacitor, it becomes essential to divide the required capacitance into multiple smaller capacitors connected in series. This modification notably impacts the resonance quality factor, allowing harmonics beyond the fundamental frequency to propagate to the antenna, ultimately reducing the amplifier's efficiency.

The primary challenge associated with the loop antenna operating at this frequency is the significantly higher reactive component compared to the real component. As a

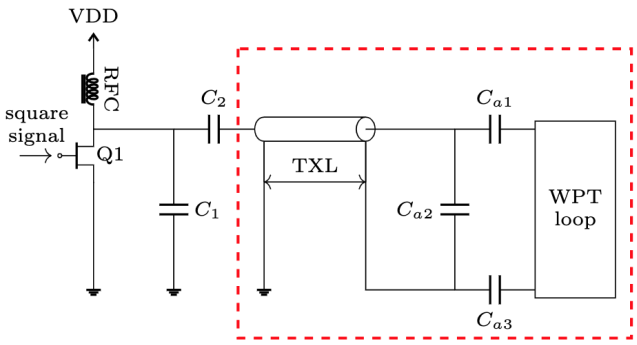

Fig. 8.5. Circuit diagram of a Class-E amplifier for telepowering devices.

result, any additional or parasitic elements introduced at the antenna's input will substantially alter the overall impedance magnitude. To address this issue, a capacitor network, as depicted in Fig. 8.5, is incorporated at the antenna's input, with each capacitor having a value of 100 pF. This network effectively reduces the ratio of the imaginary to the real component of the impedance, thereby providing the optimal load for the amplifier. Using the design equations [71] for the Class-E amplifier, a simplified circuit is constructed, as shown in Fig. 8.5. A key factor in optimizing performance is isolating the load from potential harmonics generated during the Class-E amplifier's switching process. Typically, a series RLC circuit with a quality factor greater than 10 is sufficient for this purpose. However, in this design, the RLC tanking is inherently synthesized by the matching network and the TXL circuitry located between the amplifier and the antenna, effectively reducing the number of components and associated losses. Rather than utilizing a very small inductance value, this approach incorporates a comprehensive model of the TXL cable and optimizes its length to improve overall efficiency. This strategy replaces both the capacitor and the RLC circuit with the TXL, thereby minimizing losses. It is important to emphasize that the TXL cable used in this setup is an RG-179 and it is not employed for conventional matching schemes, where cable length is a critical factor. Such a practice would likely result in suboptimal performance, with the cable contributing approximately 50% of the losses. However, these losses remain significantly lower compared to alternative solutions, such as transformers or higher-order filters. Additionally, the high quality factor, due to the small real impedance, necessitates precise tuning to account for component tolerance variations. As standards allow only fixed components, the TXL cable is used as a tuning element by adjusting its length. Accurate modeling of the cable in ADS enables fine-tuning, with various lengths tested alongside lumped components to achieve resonance while complying with regulations.

Fig. 8.6. Image of the prototype including measurement setup.

8.3.2 Simulation and Measurement Results

Modeling involved simulations to assess the impact of shifting the balise loop along the x-axis, selecting components based on performance, cost, and availability. CST provided S-parameters, Z-parameters, and magnetic field data for post-processing and co-simulation with a nonlinear GaN device. Circuit simulations using ADS's transient-assisted harmonic balance method analyzed 32 harmonics. Measurements were taken on a prototype with FR4 boards, housed in an aluminum enclosure (Fig. 8.6).

The load segment, including the WPT loop, capacitor network, and coaxial cable was simulated and measured, with impedance results. While cable length adjusts the imaginary component, controlling the real component proved difficult, with a simulated value of $3\,\Omega$ and a measured value of $1.8\,\Omega$. This discrepancy is likely due to common and differential mode currents affecting measurements, which simulation alone cannot fully address. Neglecting this could impact the amplifier's load-sensitive efficiency. The circuit was initially built without the driver and simulated in ADS. One-port S-parameters for the WPT loop, including antenna capacitors and a 40 cm TXL cable, were measured with a vector network analyzer over 2-50 MHz and imported into ADS for tuning. Fig. 8.7a shows the simulated and measured GaN drain voltage waveforms, which closely align. Discrepancies stem from parasitic inductance in the connections between the GaN output and the circuit, resulting in overshoots of about 3 V in the positive cycle and up to 8 V in the negative cycle, likely due to inaccuracies in the SPICE model's time-to-frequency domain conversion.

The SPICE model for the driver was integrated into the circuit schematic, revealing slight discrepancies between the simulated and measured drain and gate voltages. However, improvements in the drain voltage overshoots can be observed by comparing the plots in Fig. 8.7. The variations are likely attributed to external parasitic elements from the interconnections involving the driver, resistors, and GaN device. Although the

observed gate signal, as shown in Fig. 8.8a, exhibits overshoots that are acceptable as long as the operating point remains stable, careful selection of gate resistors can effectively manage this behavior. The resistors must balance the gate capacitor's charging time—crucial for proper switching—against the need to limit excessive overshoot or ringing. Adequately sized resistors can reduce ringing effects caused by parasitic inductance while ensuring the necessary charging time constant for effective operation. Additionally, waveform distortions around the gate threshold during switching stem from factors such as Miller capacitance, the non-linear behavior of the GaN gate capacitor, and the gate plateau effect [72]. As shown in Fig. 8.8b, the output voltage waveforms from simulation and measurement closely align.

The loop current was measured indirectly using the method described in [73], where the loop antenna, connected to a spectrum analyzer, allows for the calculation of magnetic field intensity. A wooden slider was utilized to move the prototype along the x-axis, maintaining a constant height of 22 cm above the balise. Measurements were taken at various displacements, with the most critical reading at the center where the loop aligns with the geometric center of the balise. At the carrier frequency of 27.095 MHz, the received power at the center was measured as -1.7 dBm. Using performance factor data from [73], the magnetic field intensity was calculated, assuming the loop is unaffected by transverse magnetic components. Based on these calculations, the loop current was determined to be 3.3 A. Since direct load current measurement is not feasible, the circuit efficiency was calculated indirectly using the simulated antenna impedance and loop current. With a total power consumption of 5.3 W for both the antenna and the 40 cm RG-179 cable, and a DC input power of 18 W, the system's indirect efficiency was found to be slightly more than 70%. The detailed calculations for these results are outlined in [65].

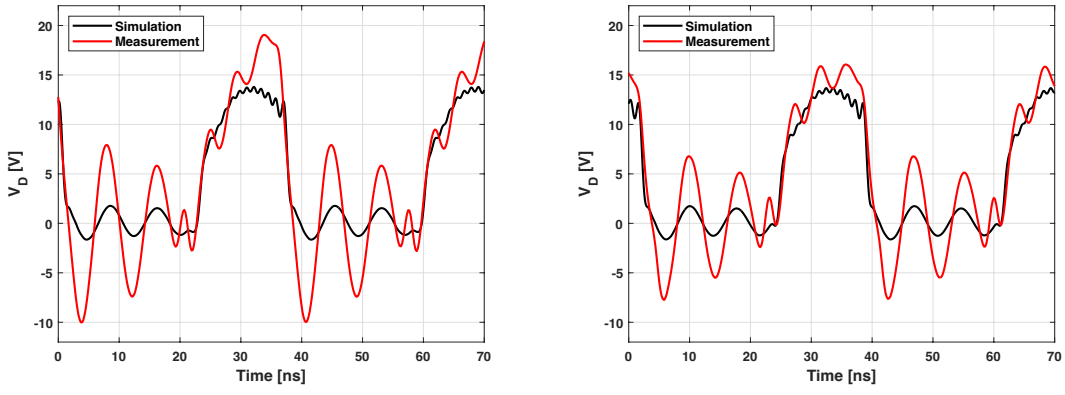

Fig. 8.7. Comparison of simulated and measured drain voltages of the GaN device (a) before and (b) after driver integration.

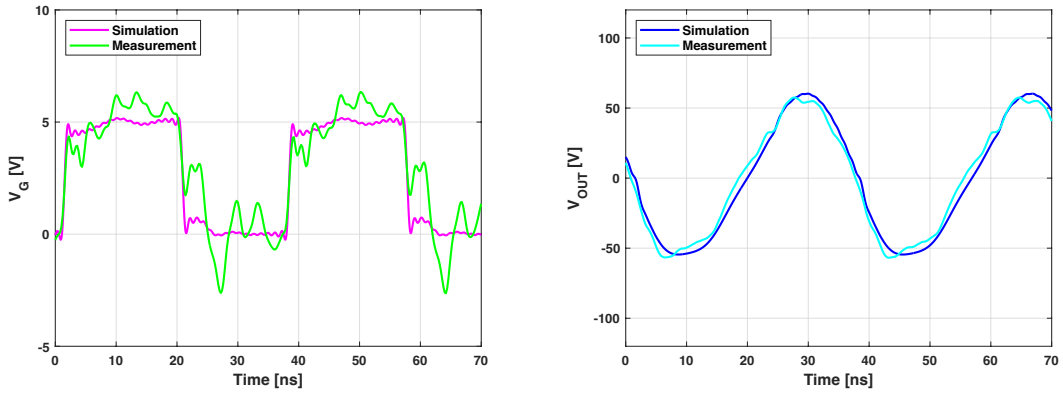

Fig. 8.8. Simulated and measured (a) gate and (b) load voltages of the GaN device with the driver.

8.4 Conclusion of the Chapter

This section presents a novel design for powering train balises, validated through a combination of simulations and measurements. The impact of the distance between the wireless loop and its metal enclosure was analyzed, revealing variations in input impedance and magnetic field strength. In addition to offering an alternative approach to the existing commercial standard, a key challenge was matching the Class-E amplifier to a predominantly inductive load with a minimal real component. This issue was resolved by balancing the real and reactive components through a capacitor network, while fine-tuning was achieved by optimizing the inductive properties of the TXL cable. The telepowering circuit was designed to operate with the lowest possible DC voltage, supported by a gate driver to provide the necessary high-current drive to the power device. The final circuit achieved a 70% indirect efficiency, significantly reducing the power required to activate the balise.

This section of the thesis functions as a preliminary exploration for the design of a Class-E based inverter, which is detailed in Chapter 5 and is intended for subsequent integration with a transparent antenna to facilitate a comprehensive in-space WPT transmitter. Consequently, this chapter offers a high-level overview of the research, rather than engaging in an exhaustive discussion of technical specifics. Furthermore, this chapter marks the culmination of the presentation of my research work, while the subsequent chapter will explore the future prospects and implications of in-space WPT.

9 Future Prospects and Impacts of In-Space Wireless Power Transfer

As the exploration and utilization of outer space continue to expand, the integration of WPT not only holds promise for enhancing operational capabilities but also poses important considerations for the sustainability and safety of space activities. One of the foremost challenges arising from the burgeoning satellite population and the growing volume of space debris is the imperative to manage orbital sustainability effectively.

9.1 Managing Space Debris and Orbital Sustainability

The rapid growth in the number of satellites and space debris in Earth's orbit presents significant challenges for space infrastructure. As the density of these objects increases, so does the risk of collisions between satellites and debris, which can lead to unexpected fragmentation events. These collisions not only threaten the functionality of active satellites but also create more debris, further escalating the risk of future collisions. The consequences of such events can be severe, including damage to space assets, disruption of crucial services like communication and navigation, and even the potential for a cascading effect, known as the Kessler syndrome [74], where debris generation becomes uncontrollable.

Moreover, the increasing volume of debris raises concerns about the long-term sustainability of Earth's orbits. If left unmanaged, the accumulation of space junk could render key orbital pathways unusable, restricting access to space for future missions and making it difficult to maintain and deploy new space-based technologies. The degradation of these orbits could severely impact the services that satellites provide, from weather monitoring to global communications, underscoring the urgent need for effective space debris management strategies and policies to preserve the safety and functionality of space infrastructure.

The rapid commercialization of space and the growing prevalence of satellite constellations, such as SpaceX's Starlink and OneWeb, have drastically increased the number of satellites operating in LEO. This surge in orbital traffic has heightened concerns about space debris and the potential triggering of the Kessler Effect, where collisions between objects in space could create a cascade of debris. Despite efforts to implement debris mitigation strategies, the steady launch of satellites continues to contribute to the accumulation of both tracked and untracked space debris. While some companies, like SpaceX, design their satellites to deorbit and burn up at the end of their operational lives, the overall volume of objects in orbit is becoming a growing challenge [75]. This situation underscores the urgent need for more effective debris removal technologies and stricter enforcement of space debris mitigation policies to

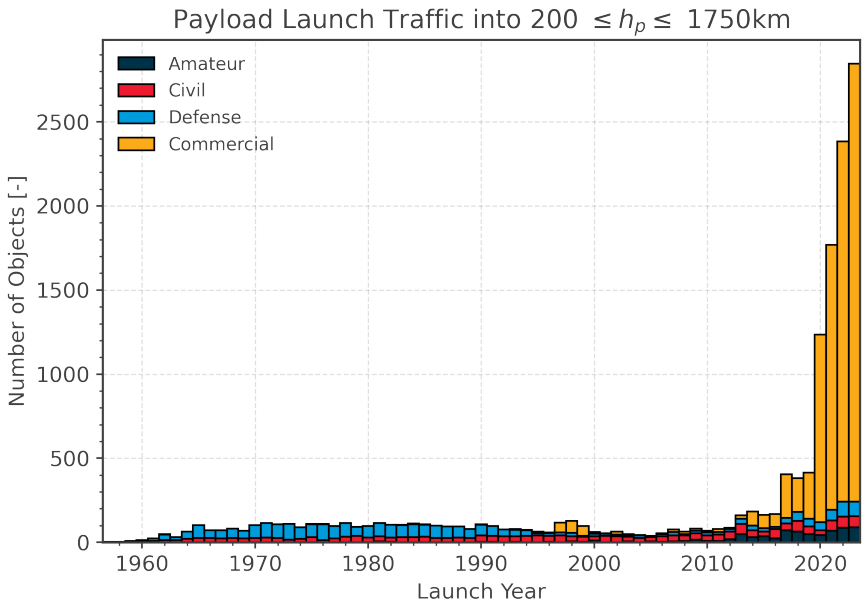

Fig. 9.1. Payload launch traffic of missions to LEO and GEO provided by the Space Debris Environment Report [76].

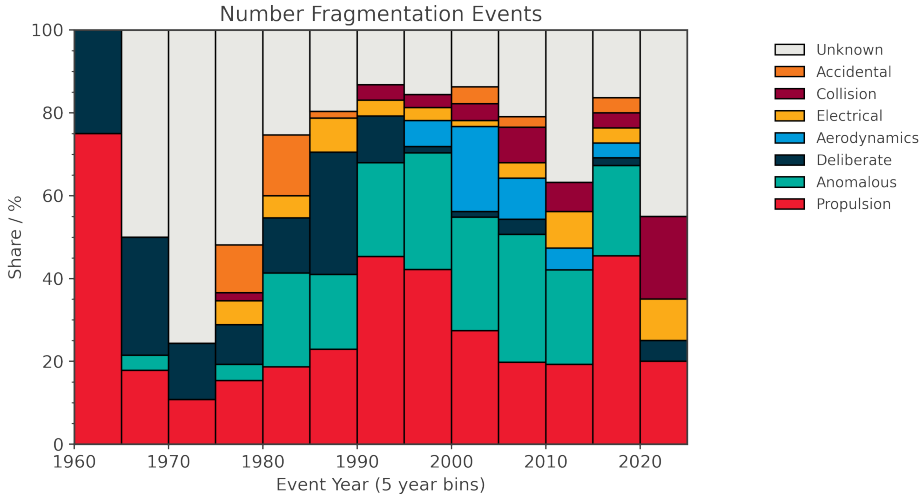

Fig. 9.2. Percentage of orbital fragmentation caused by various events, as reported in the Space Debris Environment Report [76].

maintain the long-term sustainability of space activities.

Fig. 9.1 and 9.2 provide compelling visual evidence of the rising complexity of space debris management. In Fig. 9.1, the dramatic increase in payload launches since the 2010s is primarily attributed to the commercial sector, which dwarfs civil, defense, and amateur payloads. The sharp spike observed from 2020 onward aligns with the mass deployment of satellite constellations, particularly in LEO. This exponential growth signifies the escalating challenge of managing an overcrowded orbital environment. It is clear that as the number of commercial satellites continues to surge, the potential for accidental

collisions and debris generation will also rise. In Fig. 9.2, the breakdown of fragmentation events by cause over time offers valuable insight into the dynamics of debris creation. It is evident that propulsion failures and anomalous events have consistently contributed to a significant portion of these events, with collisions becoming a growing concern in the last few decades. The share of unknown causes also remains non-negligible, underscoring the challenge of tracking and attributing space debris events. The variation in the types of fragmentation events over time suggests that different mitigation strategies may be necessary depending on the dominant debris-generating factors during specific periods. Together, these figures highlight not only the accelerating pace of space activity but also the diverse sources of debris, both of which complicate efforts to maintain safe and sustainable space operations.

To address the escalating challenges posed by space debris, several innovative mitigation and remediation strategies must be implemented. One promising approach involves developing debris removal technologies that use minimal propellant, such as electrodynamic tethers [77] or ion-beam shepherding [78], enabling efficient deorbiting of space debris without significantly adding to the operational cost of active satellites. In-space recycling and re-use of orbital assets is another key strategy, where obsolete spacecraft can be repurposed, reducing the need for new launches and preventing additional debris accumulation. Moreover, enhancing collision avoidance systems through advanced autonomous algorithms will be vital as orbital congestion grows, allowing for real-time decision-making and trajectory adjustments based on predictive models. The improvement of sensor networks for detecting smaller, untracked debris, combined with refined simulation tools for re-entry, will further bolster debris mitigation efforts by ensuring that deorbited objects pose minimal risk. These integrated approaches are crucial to maintaining the long-term sustainability of space activities in increasingly crowded orbits.

In addition to these strategies, air-breathing thrusters [81] are emerging as a promising solution for deorbiting satellites and space debris by leveraging atmospheric particles to generate propulsion, with some examples of this concept shown in Fig. 9.3. These thrusters can draw in scarce atmospheric molecules, such as oxygen and nitrogen, allowing for thrust generation without the need to carry large amounts of propellant. This capability makes them particularly suitable for small satellites or debris still situated in LEO, where the thin atmosphere can still be utilized effectively. As the thruster collects and compresses these atmospheric particles, it converts them into thrust through combustion or other propulsion techniques, enabling a gradual reduction in altitude until re-entry occurs. However, it is important to note that air-breathing thrusters require additional energy to effectively ionize and accelerate the collected particles, adding complexity to their design. This energy demand can pose challenges for smaller spacecraft with limited power resources, underscoring the

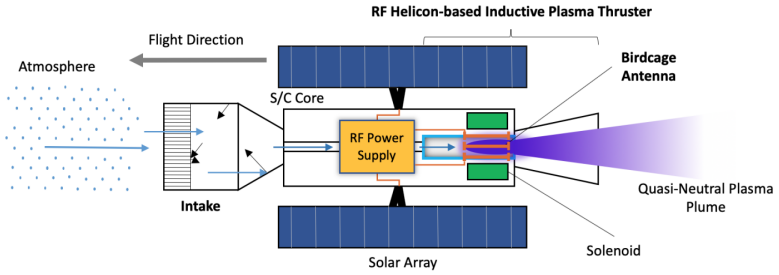

(a)

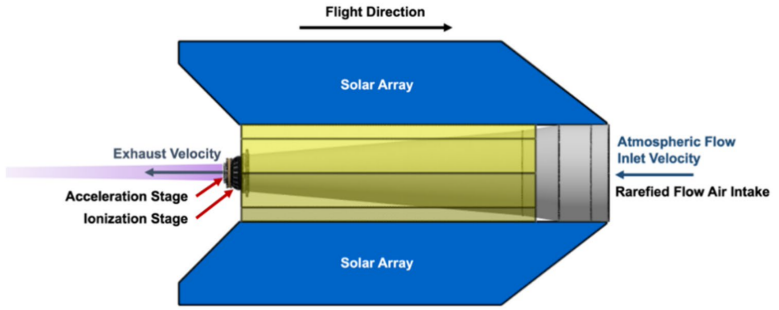

(b)

Fig. 9.3. Examples of air-breathing electric propulsion system concepts: (a) Romano et al. concept [79], (b) AETHER project [80].

necessity for careful planning and integration of power systems in the deployment of this promising technology for debris mitigation.

One potential solution to address the energy demands associated with various propulsion systems, including air-breathing thrusters, is the implementation of in-space WPT systems. This technology can be particularly beneficial in scenarios where satellites or debris equipped with different propulsion methods require additional energy for their operations, especially when solar power is insufficient or unavailable due to orbital conditions or shading from other objects. Moreover, integrating WPT with transparent antennas and solar cells can optimize space and reduce costs, allowing for efficient energy transfer while simultaneously generating power for other onboard systems. This integration not only enables continuous operation of the propulsion system without physical connections but also enhances overall system efficiency by maximizing available resources. As a result, WPT could support a range of propulsion technologies, enabling sustained operation without the burden of carrying extra fuel. As the development of in-space WPT technology progresses, it holds the potential to significantly enhance the effectiveness and viability of various propulsion systems, ultimately contributing to more efficient and effective space debris mitigation strategies across diverse applications.

10 Conclusion

The thesis explores various integrated antenna technologies and their application in WPT for space and communication systems. Central to this investigation is the development of transparent antennas that can be integrated with solar panels, offering a dual function of energy harvesting and wireless power transmission. By leveraging the abundant solar energy in space and combining it with efficient WPT systems, the research presents a novel approach to satellite energy autonomy, extending the operational capabilities of space-based systems.

A key contribution of this thesis is the design and optimization of transparent antennas. Fabricated with conductive mesh patterns, these antennas effectively transmit and receive electromagnetic waves while maintaining high levels of transparency, allowing them to be placed directly over solar panels. This research highlights the critical role of transparency in antenna design, not only to ensure efficient electromagnetic wave transmission but also to minimize any potential reduction in solar panel efficiency. By optimizing the line width and spacing of the meshed antennas, the study achieves remarkable transparency without compromising performance. A significant design enhancement includes the elimination of horizontal lines, which further enhances optical transparency while preserving robust electromagnetic functionality.

The integration of transparent antennas with PV panels is a major focus of the thesis. The author presents a detailed examination of the challenges involved in combining these two technologies, particularly the interaction between the antenna and the solar panel's metal contacts, which can affect both the antenna's radiation pattern and the solar panel's energy conversion efficiency. The research successfully develops a generalized model to optimize this interaction, ensuring that the antenna does not significantly degrade the performance of the solar panel. The thesis also presents an in-depth investigation into the interaction between the antenna and the solar panel's top metal contacts, which affect both the antenna's radiation pattern and the solar cell's energy conversion efficiency. Extensive simulations and experimental validation demonstrate the feasibility of this combined system, offering practical solutions for energy-constrained space missions.

In addition to the transparent antenna design, the thesis explores the development of WPT systems for space applications, particularly for CubeSats. The concept of in-space wireless power transfer between satellites is examined through various scenarios, including power transfer from larger satellites to CubeSats and cooperative power sharing within a swarm of CubeSats. The research demonstrates that, while long-range power transfer between larger satellites is achievable over several kilometers, cooperative power sharing between CubeSats is constrained to shorter distances due to their limited power

generation capacity. Nonetheless, the research highlights the viability of coordinated power transfer within a CubeSat swarm for short-range applications.

The research also extends to the design of a Class-E amplifier-based inverter, which plays a crucial role in the WPT system. The inverter is responsible for converting the DC power generated by the solar panel into high-frequency AC signals that can be transmitted wirelessly. By employing a Class-E amplifier, the research achieves high power conversion efficiency, which is essential for space-based systems where energy resources are limited. The design of the inverter is carefully optimized to ensure that it can drive the transparent antenna array effectively, providing the necessary power for wireless transmission without introducing significant losses.

Furthermore, the thesis examines the broader implications of the research for space sustainability. As the number of satellites in orbit continues to grow, managing space debris and ensuring the long-term sustainability of orbital pathways are becoming increasingly important. The research suggests that WPT could play a pivotal role in debris mitigation by enabling the use of energy-efficient propulsion systems.

Overall, the thesis makes a significant contribution to the field of space-based WPT and integrated antenna technologies. The development of transparent antennas that can be integrated with solar panels represents a major advancement in satellite energy systems, offering a solution that combines energy harvesting and wireless power transmission in a single structure. The research not only demonstrates the feasibility of this approach but also provides a clear pathway for further optimization and implementation in future space missions. Additionally, the exploration of Class-E amplifier-based inverters and their application in WPT systems offers valuable insights into the design of efficient power conversion systems for space applications. By addressing the challenges of space debris and orbital sustainability, the research also highlights the potential of WPT to contribute to the long-term sustainability of space activities.

In conclusion, the thesis presents a comprehensive study of integrated antenna technologies and wireless power transfer solutions for space and communication systems. Through the development of transparent antennas, efficient power amplifiers, and innovative WPT systems, the research provides a foundation for future advancements in satellite energy autonomy and space sustainability. The findings of this research have the potential to impact not only space missions but also terrestrial communication networks, where WPT could play a key role in powering low-energy devices and off-grid systems. As technology continues to evolve, the integration of WPT with other energy systems will likely become a critical component of next-generation communication and power infrastructure, both in space and on Earth.

Bibliography

[1] V. Palazzi, R. Correia, X. Gu, S. Hemour, K. Wu, A. Costanzo, D. Masotti, E. Fazzini, A. Georgiadis, H. Kazemi, R. Pereira, N. Shinohara, D. Schreurs, J.-C. Chiao, A. Takacs, D. Dragomirescu, and N. B. Carvalho, "Radiative wireless power transfer: Where we are and where we want to go," *IEEE Microwave Magazine*, vol. 24, no. 2, pp. 57–79, 2023.

[2] N. Tesla, "The transmission of electrical energy without wires," *Electrical World and Engineer*, vol. 1, pp. 21–24, 1904.

[3] N. Shinohara, "Trends in wireless power transfer: Wpt technology for energy harvesting, mllimeter-wave/thz rectennas, mimo-wpt, and advances in near-field wpt applications," *IEEE Microwave Magazine*, vol. 22, no. 1, pp. 46–59, 2021.

[4] A. Costanzo, D. Masotti, G. Paolini, and D. Schreurs, "Evolution of swipt for the iot world: Near- and far-field solutions for simultaneous wireless information and power transfer," *IEEE Microwave Magazine*, vol. 22, no. 12, pp. 48–59, 2021.

[5] N. Chahat, E. Decrossas, D. Gonzalez-Ovejero, O. Yurduseven, M. J. Radway, R. E. Hodges, P. Estabrook, J. D. Baker, D. J. Bell, T. A. Cwik, and G. Chattopadhyay, "Advanced cubesat antennas for deep space and earth science missions: A review," *IEEE Antennas and Propagation Magazine*, vol. 61, no. 5, pp. 37–46, 2019.

[6] R. Baktur, "Cubesat link budget: Elements, calculations, and examples," *IEEE Antennas and Propagation Magazine*, vol. 64, no. 6, pp. 16–28, 2022.

[7] Y. Rahmat-Samii, V. Manohar, and J. M. Kovitz, "For satellites, think small, dream big: A review of recent antenna developments for cubesats," *IEEE Antennas and Propagation Magazine*, vol. 59, no. 2, pp. 22–30, 2017.

[8] M. Sureda, M. Sobrino, O. Millan, A. Aguilella, A. Solanellas, M. Badia, J. F. Munoz-Martin, L. Fernandez, J. A. Ruiz-De-Azua, and A. Camps, "Design and testing of a helix antenna deployment system for a 1u cubesat," *IEEE Access*, vol. 9, pp. 66 103–66 114, 2021.

[9] N. Chahat, R. E. Hodges, J. Sauder, M. Thomson, E. Peral, and Y. Rahmat-Samii, "Cubesat deployable ka-band mesh reflector antenna development for earth science missions," *IEEE Transactions on Antennas and Propagation*, vol. 64, no. 6, pp. 2083–2093, 2016.

[10] N. Virushabadoss, N. Mahjabeen, H. S. Phull Bakshi, and R. Henderson, "Design of x-and ka-band reflectarray antennas for intercelestial communication using cubesat

relay," in *2021 IEEE Space Hardware and Radio Conference (SHaRC)*, 2021, pp. 31–34.

[11] P. Kokila, T. Gunasekar, T. Mohanasundaram, M. Senthilkumar, S. K. T, and S. P, "Radio astronomy based s-band horn antenna for cubesat application," in *2023 International Conference on Self Sustainable Artificial Intelligence Systems (ICSSAS)*, 2023, pp. 1745–1749.

[12] M. J. Veljovic and A. K. Skrivervik, "Patch antenna system for cubesats in l band," in *2019 13th European Conference on Antennas and Propagation (EuCAP)*, 2019, pp. 1–5.

[13] F. Davoli, C. Kourogiorgas, M. Marchese, A. Panagopoulos, and F. Patrone, "Small satellites and cubesats: Survey of structures, architectures, and protocols," *International Journal of Satellite Communications and Networking*, vol. 37, 09 2018.

[14] K. Matsuka, E. Lupu, Y. Nakka, R. Foust, S.-J. Chung, and F. Hadaegh, "Distributed multi-target relative pose estimation for cooperative spacecraft swarm," 07 2019.

[15] A. Costanzo, L. Roselli, A. Georgiadis, N. Carvalho, A. Takacs, P. Arpesi, and R. Martins, "Could the space probe philae© be energized remotely?" *Wireless Power Transfer*, vol. 6, pp. 1–7, 05 2019.

[16] A. B. Gok, D. Masotti, and A. Costanzo, "Co-location of pv panel with meshed antenna array for inter-satellite energy transmission," *IEEE Journal of Radio Frequency Identification*, vol. 8, pp. 516–525, 2024.

[17] ——, "Integration of solar power and microwave wpt exploiting transparent antennas," in *2023 IEEE Wireless Power Technology Conference and Expo (WPTCE)*, 2023, pp. 1–4.

[18] P. Mishra and G. Singh, "6g-iot framework for sustainable smart city: Vision and challenges," *IEEE Consumer Electronics Magazine*, vol. 13, no. 5, pp. 93–103, 2024.

[19] S.-H. Park, S.-M. Kim, S. Kim, H. Yoo, B. Kim, and C.-B. Chae, "Demo: A transparent antenna system for in-building networks," in *2022 IEEE International Conference on Communications Workshops (ICC Workshops)*, 2022, pp. 1–2.

[20] M. Inomata, T. Sayama, T. Motegi, O. Kagaya, H. Shoji, S. Takeuchi, and K. Nobuoka, "Transparent glass antenna for 28 ghz and its signal reception characteristics in urban environment," in *2020 14th European Conference on Antennas and Propagation (EuCAP)*, 2020, pp. 1–5.

[21] M. E. Eralp, O. A. Civi, and R. Baktur, "Highly transparent and efficient flexible antenna for vehicle-to-everything (v2x) applications," in *2024 18th European Conference on Antennas and Propagation (EuCAP)*, 2024, pp. 01–04.

[22] M. Stanley, Y. Huang, H. Wang, H. Zhou, A. Alieldin, and S. Joseph, "A transparent dual-polarized antenna array for 5g smartphone applications," in *2018 IEEE International Symposium on Antennas and Propagation & USNC/URSI National Radio Science Meeting*, 2018, pp. 635–636.

[23] R. B. Green, M. Guzman, N. Izyumskaya, B. Ullah, S. Hia, J. Pitchford, R. Timsina, V. Avrutin, U. Ozgur, H. Morkoc, N. Dhar, and E. Topsakal, "Optically transparent antennas and filters: A smart city concept to alleviate infrastructure and network capacity challenges," *IEEE Antennas and Propagation Magazine*, vol. 61, no. 3, pp. 37–47, 2019.

[24] M. D. Poliks, Y.-L. Sung, J. Lombardi, R. Malay, J. Dederick, C. R. Westgate, M.-H. Huang, S. Garner, S. Pollard, and C. Daly, "Transparent antennas for wireless systems based on patterned indium tin oxide and flexible glass," in *2017 IEEE 67th Electronic Components and Technology Conference (ECTC)*, 2017, pp. 1443–1448.

[25] K. K. So, B.-J. Chen, and C. H. Chan, "Microwave and millimeter-wave mimo antenna using conductive ito film," *IEEE Access*, vol. 8, pp. 207 024–207 033, 2020.

[26] A. K. Baghel, Y. Bikrat, J. Tavares, H. Chaves, V. U. Oliveira, P. Pinho, N. B. Carvalho, and H. Alves, "A novel portable anechoic chamber using ultra-thin 2d microwave absorber for industrial 5.0," *Scientific Reports*, vol. 14, no. 1, p. 5358, 2024.

[27] Y. Yao, Y. Shao, J. Zhang, and J. Zhang, "A transparent antenna using metal mesh for uwb mimo applications," *IEEE Transactions on Antennas and Propagation*, vol. 71, no. 5, pp. 3836–3844, 2023.

[28] T. Yasin and R. Baktur, "Bandwidth enhancement of meshed patch antennas through proximity coupling," *IEEE Antennas and Wireless Propagation Letters*, vol. 16, pp. 2501–2504, 2017.

[29] S. Sivapurapu, R. Chen, M. u. Rehman, K. Kanno, T. Kakutani, M. Letz, F. Liu, S. K. Sitaraman, and M. Swaminathan, "Flexible and ultra-thin glass substrates for rf applications," in *2021 IEEE 71st Electronic Components and Technology Conference (ECTC)*, 2021, pp. 1638–1644.

[30] M. Uzair, A. Kaewcharoen, S. Chalermwisutkul, and P. Tarbut, "Characterization of glass samples for on-glass wifi and uhf rfid antenna design," in *2021 Research,*

Invention, and Innovation Congress: Innovation Electricals and Electronics (RI2C), 2021, pp. 97–101.

[31] "BOROFLOAT Technical Details", SCHOTT. [Online], Available: https://www.schott.com/en-au/products/borofloat-p1000314/technical-details [Accessed: 26-Sep-2024].

[32] M. Wagih, A. S. Weddell, and S. Beeby, "Meshed microstrip printed antenna for matching network-free rf energy harvesting," in *2021 51st European Microwave Conference (EuMC)*, 2022, pp. 761–764.

[33] "V-One Tech Specs", Voltera. [Online], Available: https://www.voltera.io/tech-specs [Accessed: 27-Sep-2024].

[34] P.-C. Yu, C.-C. Hong, and T.-M. Liou, "Bendable transparent conductive meshes based on multi-layer inkjet-printed silver patterns," *Journal of Micromechanics and Microengineering*, vol. 26, no. 3, p. 035012, 2016.

[35] Z. J. Silva, C. R. Valenta, and G. D. Durgin, "Optically transparent antennas: A survey of transparent microwave conductor performance and applications," *IEEE Antennas and Propagation Magazine*, vol. 63, no. 1, pp. 27–39, 2021.

[36] A. B. Gok, D. Masotti, and A. Costanzo, "Preliminary study of an in-space wireless power transmission for cubesats," in *2023 IEEE International Conference on Wireless for Space and Extreme Environments (WiSEE)*, 2023, pp. 99–104.

[37] N. E. Chahat, "A mighty antenna from a tiny cubesat grows," *IEEE Spectrum*, vol. 55, no. 2, pp. 32–37, 2018.

[38] T. Yekan and R. Baktur, "Conformal integrated solar panel antennas: Two effective integration methods of antennas with solar cells," *IEEE Antennas and Propagation Magazine*, vol. 59, no. 2, pp. 69–78, 2017.

[39] M. Del Prete, A. Costanzo, A. Georgiadis, A. Collado, D. Masotti, and Z. Popović, "A 2.45-ghz energy-autonomous wireless power relay node," *IEEE Transactions on Microwave Theory and Techniques*, vol. 63, no. 12, pp. 4511–4520, 2015.

[40] C. Nieto-Peroy and M. R. Emami, "Cubesat mission: from design to operation," *Applied Sciences*, vol. 9, no. 15, p. 3110, 2019.

[41] M. Ismail, A. Bakry, H. Selim, and M. Shehata, "Eclipse intervals for satellites in circular orbit under the effects of earth's oblateness and solar radiation pressure," *NRIAG Journal of Astronomy and Geophysics*, vol. 4, no. 1, pp. 117–122, 2015.

[42] M. Qaraqe, M. Usman, A. Serbes, I. S. Ansari, and M.-S. Alouini, "Power hotspots in space: Powering cubesats via inter-satellite optical wireless power transfer," *IEEE Internet of Things Magazine*, vol. 5, no. 3, pp. 180–185, 2022.

[43] F. Y. Hadaegh, S.-J. Chung, and H. M. Manohara, "On development of 100-gram-class spacecraft for swarm applications," *IEEE Systems Journal*, vol. 10, no. 2, pp. 673–684, 2016.

[44] A. Collado and A. Georgiadis, "Conformal hybrid solar and electromagnetic (em) energy harvesting rectenna," *IEEE Transactions on Circuits and Systems I: Regular Papers*, vol. 60, no. 8, pp. 2225–2234, 2013.

[45] G. D'Accolti, G. Beltrame, E. Ferrando, L. Brambilla, R. Contini, L. Vallini, R. Mugnuolo, C. Signorini, H. Fiebrich, and A. Caon, "The solar array photovoltaic assembly for the rosetta orbiter and lander spacecraft's," in *Space Power*, vol. 502, 2002, p. 445.

[46] "Rosetta's solar panels", ESA. [Online], Available: https://sci.esa.int/web/rosetta/-/54421-rosetta-solar-panels [Accessed: 06-Oct-2024].

[47] C. Hardgrove, R. Starr, I. Lazbin, A. Babuscia, B. Roebuck, J. DuBois, N. Struebel, A. Colaprete, D. Drake, E. Johnson, J. Christian, L. Heffern, S. Stem, S. Parlapiano, M. Wiens, A. Genova, D. Dunham, D. Nelson, B. Williams, J. Bauman, P. Hailey, T. O'Brien, K. Marwah, L. Vlieger, J. Bell, T. Prettyman, T. Crain, E. Cisneros, N. Cluff, G. Stoddard, and M. Kaffine, "The lunar polar hydrogen mapper cubesat mission," *IEEE Aerospace and Electronic Systems Magazine*, vol. 35, no. 3, pp. 54–69, 2020.

[48] X. Ma, T. Li, J. Ma, Z. Wang, C. Shi, S. Zheng, Q. Cui, X. Li, F. Liu, H. Guo *et al.*, "Recent advances in space-deployable structures in china," *Engineering*, vol. 17, pp. 207–219, 2022.

[49] A. U. Rehman, E. P. Van Kerschaver, E. Aydin, W. Raja, T. G. Allen, and S. De Wolf, "Electrode metallization for scaled perovskite/silicon tandem solar cells: Challenges and opportunities," *Progress in Photovoltaics: Research and Applications*, vol. 31, no. 4, pp. 429–442, 2023.

[50] T. W. Turpin and R. Baktur, "Meshed patch antennas integrated on solar cells," *IEEE Antennas and Wireless Propagation Letters*, vol. 8, pp. 693–696, 2009.

[51] S. V. Shynu, M. J. Roo Ons, P. McEvoy, M. J. Ammann, S. J. McCormack, and B. Norton, "Integration of microstrip patch antenna with polycrystalline silicon

solar cell," *IEEE Transactions on Antennas and Propagation*, vol. 57, no. 12, pp. 3969–3972, 2009.

[52] S. Aldhaher, P. C.-K. Luk, A. Bati, and J. F. Whidborne, "Wireless power transfer using class e inverter with saturable dc-feed inductor," *IEEE Transactions on Industry Applications*, vol. 50, no. 4, pp. 2710–2718, 2014.

[53] W. J. Hwang, S. W. Shin, G. W. Choi, H. J. Kim, and J. J. Choi, "High-efficiency power oscillator using harmonic-tuned matching network," in *2009 IEEE MTT-S International Microwave Symposium Digest*, 2009, pp. 1505–1508.

[54] Z. Kaczmarczyk, "A high-efficiency class e inverter–computer model, laboratory measurements and spice simulation," *Bulletin of the Polish Academy of Sciences Technical Sciences*, pp. 411–417, 2007.

[55] A. Georgiadis and A. Collado, "Solar powered class-e active antenna oscillator for wireless power transmission," in *2013 IEEE Radio and Wireless Symposium*, 2013, pp. 40–42.

[56] "E-PHEMT Transistor SAV-541+", Mini-Circuits. [Online], Available: https://www.minicircuits.com/pdfs/SAV-541+.pdf [Accessed: 21-Oct-2024].

[57] A. B. Gok, F. Benassi, G. Paolini, D. Masotti, and A. Costanzo, "A wireless/wired uhf modular system combining energy and data transfer," in *2022 Wireless Power Week (WPW)*, 2022, pp. 231–234.

[58] S. Mumtaz, A. Alsohaily, Z. Pang, A. Rayes, K. F. Tsang, and J. Rodriguez, "Massive internet of things for industrial applications: Addressing wireless iiot connectivity challenges and ecosystem fragmentation," *IEEE Industrial Electronics Magazine*, vol. 11, no. 1, pp. 28–33, 2017.

[59] V. Selvakumar, S. Sivanandan, V. Saillaja, and A. Subbarayudu, "Smart asset management: Tracking and optimizing assets with iot sensors," in *2023 2nd International Conference on Edge Computing and Applications (ICECAA)*, 2023, pp. 1354–1358.

[60] I. F. Priyanta, F. Golatowski, T. Schulz, and D. Timmermann, "Evaluation of lora technology for vehicle and asset tracking in smart harbors," in *IECON 2019 - 45th Annual Conference of the IEEE Industrial Electronics Society*, vol. 1, 2019, pp. 4221–4228.

[61] A. B. Gok, F. Benassi, D. Masotti, and A. Costanzo, "Bidirectional monopole antenna array with minimized ground plane for wlan applications," in *2023 17th European Conference on Antennas and Propagation (EuCAP)*, 2023, pp. 1–4.

[62] A. M. Yadav, C. J. Panagamuwa, and R. D. Seager, "A miniature reconfigurable printed monopole antenna for wlan/wimax and lte communication bands," in *2012 Loughborough Antennas & Propagation Conference (LAPC)*, 2012, pp. 1–4.

[63] L. Liu, Z. Zhang, Z. Tian, and Z. Feng, "A bidirectional endfire array with compact antenna elements for coal mine/tunnel communication," *IEEE Antennas and Wireless Propagation Letters*, vol. 11, pp. 342–345, 2012.

[64] M. Ammann and M. John, "Optimum design of the printed strip monopole," *IEEE Antennas and Propagation Magazine*, vol. 47, no. 6, pp. 59–61, 2005.

[65] A. B. Gok, M. Shanawani, A. Moriconi, T. Salmon Cinotti, D. Masotti and A. Costanzo, "Efficient Telepowering Unit for Balise Transmission Modules Using Class-E Amplifier," *IEEE Transactions on Transportation Electrification* [Submitted].

[66] T. Wang and L.-h. Zhao, "Modeling and optimization for balise coupling process in high speed railway," in *2017 7th IEEE International Symposium on Microwave, Antenna, Propagation, and EMC Technologies (MAPE)*, 2017, pp. 176–179.

[67] *RDG Guidance Note ETCS On-Board Equipment*, Rail Delivery Group Std. [Online]. Available: https://www.raildeliverygroup.com/media-centre-docman/acop/281-rdg-gn-nti-005etcson-boardequipmentv2/file.html

[68] UNISIG, "SUBSET-036: FFFIS for EuroBalise 3.0. 0," 2015. [Online]. Available: https://www.era.europa.eu/system/files/2022-12/index009_-_subset-036_v310.pdf

[69] ——, "SUBSET-085: Test specification for EuroBalise FFFIS V3. 0.0," 2012. [Online]. Available: https://www.era.europa.eu/system/files/2022-12/index043_-_subset-085_v300.pdf

[70] S. Aldhaher, D. C. Yates, and P. D. Mitcheson, "Load-independent class e/ef inverters and rectifiers for mhz-switching applications," *IEEE Transactions on Power Electronics*, vol. 33, no. 10, pp. 8270–8287, 2018.

[71] S. C. Cripps *et al.*, *RF power amplifiers for wireless communications*. Artech house Norwood, MA, 2006, vol. 250.

[72] M. Begue, "External gate resistor design guide for gate drivers," *no. May*, 2018.

[73] *Near-Field Probe Set*, Jan. 52013. [Online]. Available: https://www.ets-lindgren.com/sites/etsauthor/ProductsManuals/Probes_Monitors/7405.pdf

[74] D. J. Kessler, N. L. Johnson, J. Liou, and M. Matney, "The kessler syndrome: implications to future space operations," *Advances in the Astronautical Sciences*, vol. 137, no. 8, p. 2010, 2010.

[75] B. Mrusek and L. Weiland, "Space commercialization and the rise of constellations: The resulting impact on the kessler effect," in *2023 IEEE Aerospace Conference*, 2023, pp. 01–07.

[76] "Space Environment Statistics", ESA. [Online], Available: https://sdup.esoc.esa.int/discosweb/statistics/ [Accessed: 30-Sep-2024].

[77] S. Kawamoto, Y. Ohkawa, S. Kitamura, and S.-I. Nishida, "Strategy for active debris removal using electrodynamic tether," *Transactions of the Japan Society for Aeronautical and Space Sciences, Space Technology Japan*, vol. 7, no. ists26, pp. Pr_2_7–Pr_2_12, 2009.

[78] M. Merino, E. Ahedo, C. Bombardelli, H. Urrutxua, and J. Peláez, "Ion beam shepherd satellite for space debris removal," *Progress in Propulsion Physics*, vol. 4, pp. 789–802, 2013.

[79] F. Romano, Y.-A. Chan, G. Herdrich, C. Traub, S. Fasoulas, P. Roberts, K. Smith, S. Edmondson, S. Haigh, N. Crisp *et al.*, "Rf helicon-based inductive plasma thruster (ipt) design for an atmosphere-breathing electric propulsion system (abep)," *Acta Astronautica*, vol. 176, pp. 476–483, 2020.

[80] T. Andreussi, E. Ferrato, C. Paissoni, A. Kitaeva, V. Giannetti, A. Piragino, S. Schäff, K. Katsonis, C. Berenguer, Z. Kovacova *et al.*, "The aether project: development of air-breathing electric propulsion for vleo missions," *CEAS Space Journal*, vol. 14, no. 4, pp. 717–740, 2022.

[81] S. W. Jackson and R. Marshall, "Conceptual design of an air-breathing electric thruster for cubesat applications," *Journal of Spacecraft and Rockets*, vol. 55, no. 3, pp. 632–639, 2018.